(A New Proposal to Jefferson Lab PAC-49)

Measurement of the Asymmetry $A_d^{e^+e^-}$ between $e^+ - {}^2$H and $e^- - {}^2$H Deep Inelastic Scattering Using SoLID and PEPPo at JLab

May 24, 2021

(pending approval from JLab Hall A and SoLID Collaborations)

A. Afanasev, A. Schmidt
George Washington University, Washington, DC 20052, USA

D. Armstrong, T. Averett, W. Li
William and Mary, Williamsburg, Virginia 23187, USA

H. Atac, A. Atencio, R. Li, M. Nycz, N. Sparveris
Temple University, Philadelphia, PA 19122, USA

V. Bellini
INFN, Sezione di Catania, I-95129 Catania, Italy

R. Beminiwattha
Louisiana Tech. University, Ruston, LA 71272, USA

J. Benesch, A. Camsonne, J.-P. Chen, S. Covrig Dusa, A. Deur, D. Flay, D. Gaskell, J. Grames,
D. W. Higinbotham, D. Mack, M. D. McCaughan, R. Michaels, D. Nguyen, Y. R. Roblin,
M. Stefani, H. Szumila-Vance, A. S. Tadepalli
Thomas Jefferson National Accelerator Facility, Newport News, Virginia 23606, USA

J. C. Bernauer◆, E. Cline, R. Corliss, K. Dehmelt, A. Deshpande, C. Gal, T. K. Hemmick,
M. M. Mondal, S. Park, B. Schmookler
Center for Frontiers in Nuclear Science (CFNS) at
Stony Brook University, Stony Brook, NY 11794, USA
◆ *and RIKEN BNL Research Center, Upton, NY 11973, USA*

V. Bertone
IRFU, CEA, Université Paris-Saclay, F-91191 Gif-sur-Yvette, France

D. Byer, H. Gao, B. Karki, V. Khachatryan, G. Matousek, E. van Nieuwenhuizen, A. Smith,
B. Yu, Z. Zhao, J. Zhou Duke University and Triangle Universities Nuclear Laboratory,

D. Day, I. P. Fernando, K. Paschke, J. Zhang, X. Zheng[1]
University of Virginia, Charlottesville, Virginia 22904, USA

---

[1] Contact email: xiaochao@jlab.org

W. Deconinck, J. Mammei
University of Manitoba, Winnipeg, Manitoba R3T 2N2, Canada

J. Erler[♠], H. Spiesberger[♣]
PRISMA^{+} Cluster of Excellence, [♣]Institute for Nuclear Physics and [♠]Institute of Physics,
Johannes Gutenberg-University, 55099 Mainz, Germany

C. Ghosh, H. Liu
University of Massachusetts Amherst, Amherst, MA 01003, USA

P. Gueye
Michigan State University, East Lansing, MI 48824, USA

S. Habet, A. Hobart, E. Voutier
CNRS/IN2P3, IJCLab, *Université Paris-Saclay, 91405 Orsay, France*

O. Hen, T. Kutz
Massachusetts Institute of Technology, Cambridge, MA 02139, USA

T. Holmstrom
Longwood University, Farmville, VA 23909, USA

H. F. Ibrahim
Cairo University, Cairo, Giza 12613, Egypt

W. Korsch
University of Kentucky, Lexington, KY 40506, USA

S. Li
Lawrence Berkeley National Laboratory, Berkeley, CA 94720, USA

T. Liu
Shandong University, Shandong, China

S. Mantry
University of North Georgia, Dahlonega, GA 30597, USA

P. Markowitz
Florida International University, Miami, Florida 33199, USA

M. Mihovilovič, S. Širca
University of Ljubljana, 1000 Ljubljana, Slovenia

H. Mkrtchyan
A.I. Alikhanyan National Science Laboratory (Yerevan Physics Institute), Yerevan 0036,
Armenia

C. Morean

University of Tennessee, Knoxville, TN 37996, USA

G. Niculescu
James Madison Univeristy, Harrisonburg, VA 22801, USA

G. D. N. Perera, K. A. H. Sirilal
University of Colombo, Colombo 3, SRI LANKA

P. E. Reimer
Argonne National Laboratory, Argonne, Illinois 60439, USA

E. Santopinto
INFN, Sezione di Genova, I-16146 Genova, Italy

M. H. Shabestari
University of West Florida, Pensacola, FL 32514, USA

A. W. Thomas
University of Adelaide, Adelaide SA 5005, Australia

Y. Tian
Syracuse University, Syracuse, NY 13244, USA

M. H. Wood
Canisius College, Buffalo, NY 14208, USA

Z. Ye
Tsinghua University, Beijing 100084, China

Executive Summary

We propose a measurement of the asymmetry, $A_d^{e^+e^-}$, between unpolarized positron and electron beams scattering off a liquid deuterium target in the deep inelastic scattering (DIS) region. We will use the secondary positron and electron beams produced using the PEPPo process, incident on a 40-cm long liquid deuterium target. Beam polarization is not required, though knowledge of the beam polarization is desired to form additional asymmetry observables. The scattered positrons or electrons will be detected by the SoLID spectrometer in Hall A in its PVDIS configuration. The SoLID magnet polarity will be flipped to match the charge of the beam.

We request 104 PAC days of beam time that includes 96 days of production with 3 μA beams at 11 GeV and 6.6 GeV, each split between e^+ and e^- runs; 2 days for pass changes; and 6 days for Compton tune, general commissioning, and reversing the SoLID magnet polarity. Time needed to setup and commission the secondary positron or electron beam is not included in this request. The asymmetry $A_d^{e^+e^-}$ will be measured over a wide (x, Q^2) range and provide precision data on the nucleon structure function $F_3^{\gamma Z}$. From the asymmetries we will also attempt to extract the electron-quark neutral-current effective couplings, $2C_{3u} - C_{3d}$, to a precision of approximately ± 0.060. Here, $C_{3q} \equiv -2c_A^e c_A^q$, with $c_A^{e(q)}$ the axial weak charge of the electron (quark). To extract C_{3q}, higher-order QED contributions to $A_d^{e^+e^-}$ must be calculated precisely as their contribution is larger than the electroweak contribution. Similarly, differences in the beam energy and luminosity between e^+ and e^- runs will cause a sizable asymmetry and must be understood from data because it is so far unlikely that these differences can be controlled to a sufficiently precise level. We present a method of using a multi-parameter fit to separate C_{3q} from these experimental effects and further determination of $F_3^{\gamma Z}$.

The proposed measurement will help to advance our studies of electroweak physics and the nucleon structure into a terrain that was scarcely explored previously. There has only been one direct measurement on the muonic counterpart of C_{3q}, carried out at CERN in 1980, which yielded $2C_{3u}^{\mu q} - C_{3d}^{\mu q} = 1.57 \pm 0.38$. Even with the assumption of lepton universality, the knowledge gained from the CERN measurement is limited by its statistical precision. Therefore, the proposed measurement will provide the first direct access to C_{3q} for the electron-quark interaction and possibly the most precise measurement among all charged leptons. Results on the scarcely measured structure function $F_3^{\gamma Z}$ for the nucleon will add knowledge to our understanding of the nucleon structure.

Contents

1 Introduction

Our knowledge on the Standard Model (SM) of Particle Physics reached a concluding milestone in 2012, brought by experimental observations of the Higgs boson at the LHC [1][2]. Since then, the research of both medium- and high-energy physics along this direction has focused primarily on high-precision tests of the Standard Model and searching for Beyond-the-Standard-Model (BSM) physics. The fundamental questions include: Are leptons and quarks made of even smaller particles, or are they truly point-like elementary entities that exist down to the Planck scale? Are there new interactions at higher energy scales than what we have reached? At what energy scale and with what symmetry can we unify strong and electroweak interactions? How do we explain neutrino masses, and can we reduce the number of parameters of the Standard Model? Most recently, experimental results on the b quark decay [3] and the muon $g-2$ measurement [4] added exciting fresh information to the field. Of course, one might argue that some of the biggest questions are outside the scope of the SM: dark matter and dark energy still pose the greatest challenge to our understanding of gravity and the universe as a whole. These questions and challenges, along with the desire to fully understand the nucleon and the strong interaction, form in part the frontier of medium-energy nuclear physics research in the US and worldwide.

The Continuous Electron Beam Accelerator Facility (CEBAF), hosted at Jefferson Lab (JLab), has provided an essential tool in our pursuit of understanding the strong interaction and the nucleon and nuclear structure since the late 1990's. In the last decade, studies of electroweak (EW) physics have emerged as a new and pioneering direction for JLab's research program. Among these, the Qweak experiment provided the latest data on the proton weak charge and improved our knowledge on the EW neutral-current (NC) axial-vector (AV) C_{1q} couplings [5]. The 6 GeV PVDIS (Parity Violating Deep Inelastic Scattering) experiment similarly improved our knowledge on the vector-axial (VA) C_{2q} couplings [6, 7]. At this point, one begins to ask the question: can we measure other observables that can help test the Standard Model, even though such measurements have become increasingly challenging in the most recent decade?

In this document, we propose a measurement of the cross section asymmetry between positron and electron deep inelastic scattering (DIS) off a deuterium target. We plan to use secondary positron and electron beams produced by the PEPPo (Polarized Electrons for Polarized Positrons) method [8]. The scattered DIS events will be detected by the SoLID spectrometer in its PVDIS configuration [9], with its magnet polarity reversed to match the charge of the beam. In order to access the EW contribution to the asymmetry, we need to calculate electromagnetic higher-order effects and subtract them from data. To do so, we have learned some of the methods and tools used by the high-energy physics community. From the measured asymmetries, we will extract the scarcely measured nucleon $F_3^{\gamma Z}$ structure function, and possibly provide the first direct determination of the axial-axial (AA) electroweak NC coupling combination, $2C_{3u} - C_{3d}$, for electron-quark interactions.

2 The Physics Case of Electroweak Neutral Current Couplings

2.1 Four-Fermion Interactions and Effective Couplings

At medium energy scales much below the W and Z bosons masses, the weak NC interaction of electron DIS off a nucleon or nuclear target can be written using the effective Lagrangian [10]:

$$L_{NC}^{e^-q} = \frac{G_F}{\sqrt{2}} \sum_q \left[C_{1q}\bar{e}\gamma^\mu\gamma_5 e\bar{q}\gamma_\mu q + C_{2q}\bar{e}\gamma^\mu e\bar{q}\gamma_\mu\gamma_5 q + C_{3q}\bar{e}\gamma^\mu\gamma_5 e\bar{q}\gamma_\mu\gamma_5 q\right], \quad (1)$$

where $G_F = 1.166\times10^{-5}$ (GeV)$^{-2}$ is the Fermi constant. The terms $\bar{e}\gamma^\mu\gamma_5 e\bar{q}\gamma_\mu q$, $\bar{e}\gamma^\mu e\bar{q}\gamma_\mu\gamma_5 q$ and $\bar{e}\gamma^\mu\gamma_5 e\bar{q}\gamma_\mu\gamma_5 q$ are often referred to as the AV, VA, and AA four-fermion contact interactions, respectively, which are low-energy approximations of the NC weak interaction of the Standard Model. Each of the terms is multiplied by the corresponding effective electron-quark (eq) coupling. At the one-boson-exchange level (tree level): $C_{1q} = 2c_A^e c_V^q$, $C_{2q} = 2c_V^e c_A^q$ and $C_{3q} = -2c_A^e c_A^q$, with $c_{V,A}^{e(q)}$ the lepton (quark) neutral-current vector (V) and axial (A) couplings to the Z^0. The SM predictions for u and d quarks relate their effective NC couplings to the weak mixing angle θ_W. At the tree level:

$$C_{1u} = -\frac{1}{2} + \frac{4}{3}\sin^2\theta_W\ ,\ C_{2u} = -\frac{1}{2} + 2\sin^2\theta_W\ , C_{3u} = \frac{1}{2}\ , \quad (2)$$

$$C_{1d} = \frac{1}{2} - \frac{2}{3}\sin^2\theta_W\ ,\ \ C_{2d} = \frac{1}{2} - 2\sin^2\theta_W\ ,\ \ C_{3d} = -\frac{1}{2}\ . \quad (3)$$

One main focus of low or medium-energy experiments is to determine these effective couplings to a high precision, as any deviation from their SM predictions could indicate a modification of the Lagrangian, i.e., a hint of the existence of BSM physics. The current knowledge of C_{1q} and C_{2q} is shown in Fig. 1 [11], along with expected results from the planned P2 experiment at Mainz [12] on C_{1q} and the planned SoLID project [9] at JLab on C_{2q}.

In recent years, a different notation – g_{AV}^{eq}, g_{VA}^{eq} and g_{AA}^{eq} – was introduced [17] and has been adopted by PDG (Particle Data Group) since 2017. The difference from the $C_{1q,2q,3q}$ is that the new notation (the g's) absorbs some higher-order corrections. The new notation is also no longer defined as the product of $c_{V,A}^e$ and $c_{V,A}^q$ and thus can absorb effects from BSM physics. More importantly, the extracted values of $g_{AV,VA,AA}^{eq}$ should be independent of the processes in which they are measured. This allows a direct comparison of the weak NC couplings between experiments. We will continue using the $C_{1q,2q,3q}$ notation in this document, and will use the new $g_{AV,VA,AA}^{eq}$ notation once data are collected and the process of extracting the couplings begins.

2.2 Knowledge of Muonic C_{3q} at CERN

While the $C_{1q,2q}$ couplings are parity-violating, the AA interaction or the C_{3q} coupling can only be accessed by comparing lepton with anti-lepton scattering. In fact, direct measurements on the electron-quark C_{3q} do not yet exist. The only related measurement is a CERN experiment [18] that extracted the muonic counterpart of C_{3q} by comparing (polarized) μ^- vs. μ^+ DIS cross sections off a carbon target. The asymmetry measured was

$$B_+ \equiv \frac{\sigma^+(-|\lambda|) - \sigma^-(+|\lambda|)}{\sigma^+(-|\lambda|) + \sigma^-(+|\lambda|)} = -\frac{3G_F Q^2}{10\sqrt{2}\pi\alpha} Y(y)[(2C_{3u} - C_{3d}) + |\lambda|(2C_{2u} - C_{2d})], \quad (4)$$

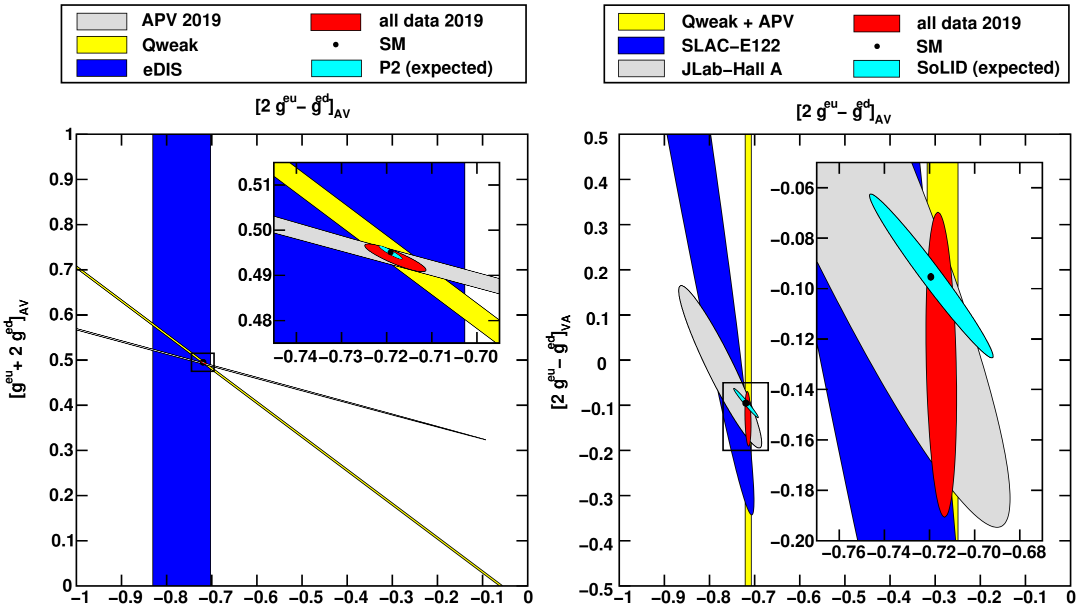

Figure 1: From Ref. [11]: Current and expected knowledge of the couplings C_{1q} or g_{AV}^{eq} (left) and C_{2q} or g_{VA}^{eq} (right). In the left panel, the Atomic Parity Violation ("APV 2019") results shown utilized the latest theory calculations of [13] and the "eDIS" band is a combination of the SLAC E122 [14, 15] and the JLab PVDIS [6, 7] experiments. Expected results from the future P2 @ Mainz [12] and SoLID @ JLab [9, 16] are also shown, centered at the SM values.

where the superscript in $\sigma^{\pm}$ indicates the charge of the muon beam, $|\lambda|$ is the magnitude of the beam polarization, the sign in $\pm|\lambda|$ represents the helicity of the incident beam, α is the fine structure constant, G_F is the Fermi constant, $Q^2 \equiv -q^2$ with q the 4-momentum transfer, $y \equiv \nu/E$ with ν the energy transfer and E the incident beam energy, and

$$Y(y) \equiv \frac{1-(1-y)^2}{1+(1-y)^2}\,. \tag{5}$$

The CERN results using two beam energies $E = 200$ GeV ($|\lambda| = 0.81$) and 120 GeV ($|\lambda| = 0.66$) were

$$2C_{3u} - C_{3d} + 0.81(2C_{2u} - C_{2d}) = 1.45 \pm 0.41, \tag{6}$$

$$2C_{3u} - C_{3d} + 0.66(2C_{2u} - C_{2d}) = 1.70 \pm 0.79, \tag{7}$$

where the values $\alpha = 1/129$ and $1/130$ were used for the two energies, respectively, evaluated at the averaged Q^2 value of the corresponding beam energy. These results can be compared to the SM tree level predictions of 1.42 and 1.44, respectively. Note that these results were previously summarized in [19] but the calculations were updated in [20]. Using the SM values for $2C_{2u} - C_{2d}$, we find the constraint

$$[2C_{3u} - C_{3d}]^{\mu q} = 1.57 \pm 0.38, \tag{8}$$

where we assumed that the (smaller) systematic error of the 200 GeV data was common to both beam energies. This is in good agreement with the SM value ($+1.5$). Assuming lepton universality, one may compare the precision of the CERN results on C_{3q} with those shown in Fig. 1. However, we note that there is so far no direct data on C_{3q} for electron-quark interactions. The proposed measurement will change this situation.

2.3 Asymmetries in e^+ vs. e^- Deep Inelastic Scattering

For the difference between e^+ and e^- scattering, we can define the following asymmetries:

$$A_{RL}^{e^+e^-} \equiv \frac{\sigma_R^{e^+} - \sigma_L^{e^-}}{\sigma_R^{e^+} + \sigma_L^{e^-}},\ A_{LR}^{e^+e^-} \equiv \frac{\sigma_L^{e^+} - \sigma_R^{e^-}}{\sigma_L^{e^+} + \sigma_R^{e^-}}\ ;\ A_{LL}^{e^+e^-} \equiv \frac{\sigma_L^{e^+} - \sigma_L^{e^-}}{\sigma_L^{e^+} + \sigma_L^{e^-}},\ A_{RR}^{e^+e^-} \equiv \frac{\sigma_R^{e^+} - \sigma_R^{e^-}}{\sigma_R^{e^+} + \sigma_R^{e^-}},$$

where the subscripts R, L represent the helicity of the incident beam $h = +1, -1$. Additionally, the helicity-independent (unpolarized) lepton-charge asymmetry is defined as

$$A^{e^+e^-} \equiv \frac{\sigma_{h=0}^{e^+} - \sigma_{h=0}^{e^-}}{\sigma_{h=0}^{e^+} + \sigma_{h=0}^{e^-}}. \tag{9}$$

Detailed expressions of these asymmetries for DIS off a hydrogen (proton) or a deuterium target are summarized in Appendix A and parton-model derivations given in Appendix D. Here we focus on $A_d^{e^+e^-}$, the asymmetry between unpolarized positron and electron beams scattering off the deuteron since it provides a direct access to the combination $2C_{3u} - C_{3d}$. The parton-model expression for the asymmetry is:

$$A_d^{e^+e^-} = -\frac{3G_F Q^2}{2\sqrt{2}\pi\alpha} Y(y) R_V \frac{(2C_{3u} - C_{3d})}{5 + 4R_C + R_S}\ , \tag{10}$$

where

$$R_V(x) \equiv \frac{u_V + d_V}{u^+ + d^+}\ ,\ R_C(x) \equiv \frac{2c^+}{u^+ + d^+}\ ,\ R_S(x) \equiv \frac{2s^+}{u^+ + d^+}\ , \tag{11}$$

are defined by the parton distribution functions (PDF) $q^+ \equiv q + \bar{q}$ and $q_V \equiv q - \bar{q}$. The assumption $s = \bar{s}$ and $c = \bar{c}$ were used. Quantitatively, one can write

$$A_d^{e^+e^-} = -(108\,\mathrm{ppm/GeV^2}) Q^2 Y(y) \frac{R_V}{1 + \frac{4}{5}R_C + \frac{1}{5}R_S}(2C_{3u} - C_{3d})\ . \tag{12}$$

The full expressions using structure functions are also given in Appendix A. For the unpolarized asymmetry and ignoring γZ contribution to the denominator, we have:

$$A_{d,\mathrm{full}}^{e^+e^-} = \frac{G_F Q^2}{2\sqrt{2}\pi\alpha} \frac{g_A^e}{2} Y_3 \frac{F_3^{\gamma Z}}{F_1^{\gamma}}\ , \tag{13}$$

where

$$Y_3 = \left[\frac{r^2}{1 + R^\gamma}\right] \frac{1 - (1-y)^2}{1 + (1-y)^2 - y^2\left[1 - \frac{r^2}{1+R^\gamma}\right] - \frac{2M^2x^2y}{Q^2}}\ . \tag{14}$$

with $R^\gamma \equiv \sigma_L^\gamma/\sigma_T^\gamma$ and $r^2 = 1 + \frac{Q^2}{\nu^2}$. The structure functions, $F_{1,3}^{\gamma,\gamma Z}$, can be written in terms of PDFs at the parton model level:

$$F_1^\gamma(x,Q^2) = \frac{1}{2}\sum Q_q^2\left[q(x,Q^2)+\bar{q}(x,Q^2)\right], \tag{15}$$

$$F_1^{\gamma Z}(x,Q^2) = \sum Q_q g_V^q\left[q(x,Q^2)+\bar{q}(x,Q^2)\right], \tag{16}$$

$$F_3^{\gamma Z}(x,Q^2) = 2\sum Q_q g_A^q\left[q(x,Q^2)-\bar{q}(x,Q^2)\right], \tag{17}$$

where Q_q denotes the quark's electric charge and the summation is over the quark flavors $u, d, s\cdots$. Hence measurement of $A_d^{e^+e^-}$ provides a direct measurement of the structure function $F_3^{\gamma Z}$ if world data on F_1^γ are used as inputs.

2.4 The *AA* Effective Coupling and BSM Physics Search

While precision data on the $C_{1q,2q}$ provided constraints on the energy (or "mass") limit below which BSM physics is unlikely to occur, it is important to measure all axial and vector combinations of the EW NC couplings. The strong coupling mass limit on BSM physics that can be imposed by a C_{3q} measurement with uncertainty $\Delta(2C_{3u}-C_{3d})$ in the optimal case [2], is:

$$\Lambda = v\sqrt{\frac{8\sqrt{5}\pi}{\Delta(2C_{3u}-C_{3d})}}, \tag{18}$$

where $v = \sqrt{1/(\sqrt{2}G_F)} = 246.22$ GeV is the Higgs vacuum expectation value, and the $\sqrt{5}$ is a normalization factor taking into account the coefficients of the $C_{3u,3d}$ in the denominator for the optimal scenario.

Any model predicting a significant effect in the C_{3q} (AA), while leaving the $C_{1q,2q}$ (AV and VA) unaltered, is presumably contrived or tuned, though one could argue that our universe is very fine-tuned to start with. We emphasize here that the C_{3q} are couplings independent of the $C_{1q,2q}$ and pose complementary constraints on BSM physics. Conversely, if new physics is seen in the C_{1q} or C_{2q}, it would be of paramount importance to measure the C_{3q}, as well.

2.5 The CERN Experiment NA004

In this paragraph we give a brief description of the CERN experiment NA004 carried out by the BCDMS Collaboration. The experiment utilized the polarized $\mu^\pm$ beams on a 40-meter [3] long ^{12}C target. Two beam energies were used: 200 and 120 GeV. The beam energy was measured to $\pm 0.5\%$ and the energy calibration for the difference of μ^+ vs. μ^- was kept at 6×10^{-4} and 13×10^{-4} level for 200 and 120 GeV, respectively. Beam charge was reversed twice per data taking period of 12 days with intensity at about 2×10^7 muons per spill. The $\mu^\pm$ events were taken at the same intensity such that systematic effects (intensity, deadtime, etc) largely

---

[2] If certain BSM physics modifies both C_{3u} and C_{3d} but in the same direction with $\delta C_{3u} = \frac{1}{2}\delta C_{3d}$, then it cannot be accessed by the proposed measurement. We present here the optimal scenario where the sensitivity to BSM physics is maximized. See [11] for details.

[3] This is not a typo, in case the reader wonders...

cancel. The polarity of the spectrometer was reversed between each μ^+ and μ^- data taking. The spectrometer was running at the saturated state and the absolute field was kept at 2×10^{-4} precision after each polarity change. A total of five, two, and one 12-day data taking periods were spent at 200 GeV with $Q^2 > 30$ (GeV)^2, 120 GeV with $Q^2 > 20$ (GeV)^2, and 120 GeV with $Q^2 > 12$ (GeV)^2, respectively. In extracting the EW contributions to the asymmetry, the dependence of the measured asymmetries on various kinematics variables – x, y, Q^2 and θ – were studied and compared with the expectation from experimental systematic effects such as different μ^+ and μ^- beam energies, and no visible sign of such effects was found. Higher order QED and EW radiative corrections were calculated and were found to be comparable in size to the EW contribution to the asymmetry. These corrections were applied, and the final extracted asymmetries were fitted vs. $Y(y)Q^2$ and the fitted slope provided the final results on $2C_{3u} - C_{3d}$.

We note that many of the experimental strategies of the CERN NA004 experiment can be applied to the proposed measurement, although there will be larger radiative corrections (relative to the EW contribution) at JLab beam energies. On the other hand, while larger Q^2 values mean smaller radiative corrections, the higher Q^2 implies that purely weak effects (the Z terms) may no longer be neglected, and observables are sensitive to a combination of couplings that can be separated only by fitting the data globally. In addition, the Y-weighting of C_{3q} in $A^{e^+e^-}$ (similar to C_{2q} in PVDIS) implies it is best accessed in a fixed-target (high y) setting. These show part of the complementarity between medium energy (direct access to a specific combination of the couplings) and high energy (access to a combination of many couplings) experiments is highly desired. For the specific cases of C_{2q} and C_{3q}, JLab is the best place to directly measure these couplings precisely.

3 The Proposed Experiment

In this section we will first summarize the present initiative towards developing positron beams at CEBAF. Then we will discuss beamline requirements for the positron beam in Hall A, the liquid deuterium target and the SoLID spectrometer. We will provide simulated rates for the proposed measurement, the expected electroweak contribution to the asymmetries, and the projected statistical uncertainty. Then we will discuss specific aspects of the measurement such as tracking efficiency, particle identification and background corrections. We leave discussions of all systematic effects to the next section.

3.1 The Positron Source

The production of positron beams from unpolarized electron beams is a commonly known technique used at numerous accelerator facilities. For the physics program at CEBAF, a polarized beam is desired to study a wide range of topics and the technique to produce polarized positron beams is much more involved. As of today, HERA has been the only facility to run polarized positron beams, using the self-polarization of multi-GeV positrons via the Sokolov-Ternov effect [21], but such energy is outside the range of the CEBAF injector and accommodating such high energy e^+ source would be costly. For the proposed measurement we consider a process in which an initially polarized electron beam of low energy is incident on a high-Z target, which produces polarized positrons through Bremsstrahlung radiation followed by pair production. The new PEPPo experiment [8] using a 8.2-MeV/c electron beam with an 85.2%

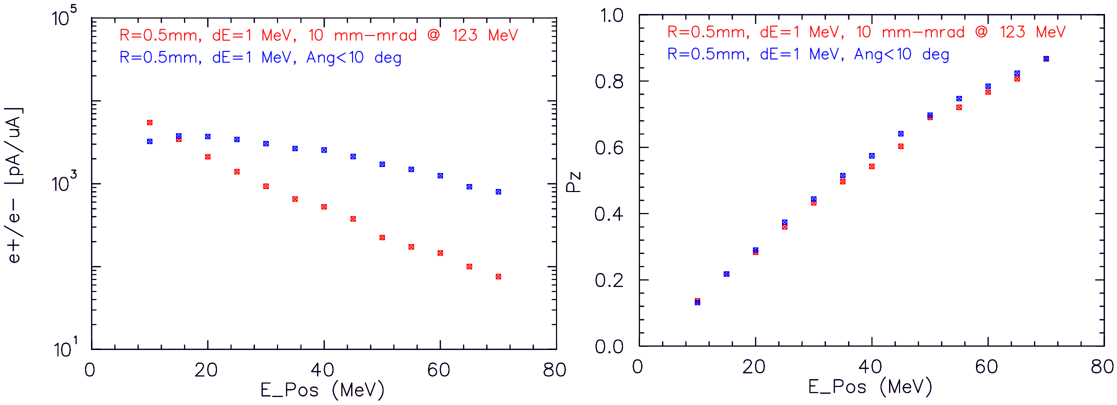

Figure 2: Energy dependence of the positron efficiency production (left) and polarization (right) simulated with a 123 MeV and 100% polarized electron beam [8]. Points correspond to the selection of produced positrons within an energy spread of 1 MeV and a constant angular acceptance of 10° (blue) or a 10 mm·mrad emittance (red).

polarization demonstrated the polarization transfer from primary electrons to secondary particles (electrons and positrons) can reach 100%. The PEPPo technique is ideally suited for the production of both polarized and unpolarized positron beams at CEBAF.

The polarization of such positron beam depends on the required beam intensity. The trade-off between polarization and intensity capabilities is illustrated in Fig. 2 showing the simulated performance of a positron source using a 123 MeV and 100% polarized primary electron beam. A software collimator combining a 1 MeV energy acceptance and alternatively a 10° angular acceptance or a 10 mm·mrad emittance mimics the positron collection efficiency, with the latter configuration corresponding to the measured emittance acceptance of CEBAF [22]. Considering a 1 mA initial electron beam, the simulated positron beam intensity decreases from 5 μA down to 100 nA in the 10-60 MeV positron energy range, while the polarization increases from 10% up to 75%.

Several designs for injecting the positron beam at CEBAF were discussed in [8]. For each design, the same technique can be used to produce a secondary electron beam with similar characteristics as the positron beam. In one of the approaches, it was estimated that a 3 μA positron beam can be produced comfortably [22] when polarization is not required, which is the value we choose to use in this proposal.

3.2 Acceleration of Positrons in CEBAF

The operation of CEBAF with positron beams was extensively discussed in the LOI12-18-004 [23] and we summarize the main requirements and features of the positron beam here. Accelerator R&D is on-going to develop the source concept with realistic parameters and more results are expected in Fall of 2022.

In order for positrons to transit CEBAF in the usual electron path, all magnet polarities need be inverted. The dipole powering network uses common power supplies feeding strings of magnets in series. The magnets were designed to be slightly too high in field strength, and electronic loads (shunts) are installed to shunt a controlled amount of the current. All machine protection provisions for the dipole magnets remain functional with the main power supply leads inverted. The shunt hardware is unipolar, and inverting the shunt leads in coordination with the power supply leads leaves the dipole powering network fully functional and protected. These many power supplies and shunt connections require reversing switches (see Appendix B) to be installed with carefully designed features to ensure that all polarity changes are appropriately coordinated.

The injection chicane properties (aperture and dispersion) control the CEBAF beam acceptance and are normally configured for low emittance and low momentum spread beams. But the principal limiting aperture of the chicane is very localized and can be readily modified to increase its acceptance for the anticipated positron beam. Once the beam passes the injector chicane and enters CEBAF, we focus on beam optical parameters in each pass of acceleration and up to the experimental halls, see Fig. 3. The beam properties are affected by two factors that cause differences between e^+ and e^- beams: the acceleration damping within the CEBAF accelerating sections, and the synchrotron radiation in the recirculating arcs. The dynamics of the momentum spread of electron beams is dominated by radiation effects, while despite a much larger initial momentum spread, positron beams essentially benefit from acceleration damping which results in the same momentum spread as electron beams. The large positron beam emittance at the injector entrance is strongly reduced by acceleration effects, which results in a final emittance 4-5 times larger than the one of electron beams. This difference in the secondary e^+ vs. e^- beams characteristics should be taken into account when designing high-precision experiments.

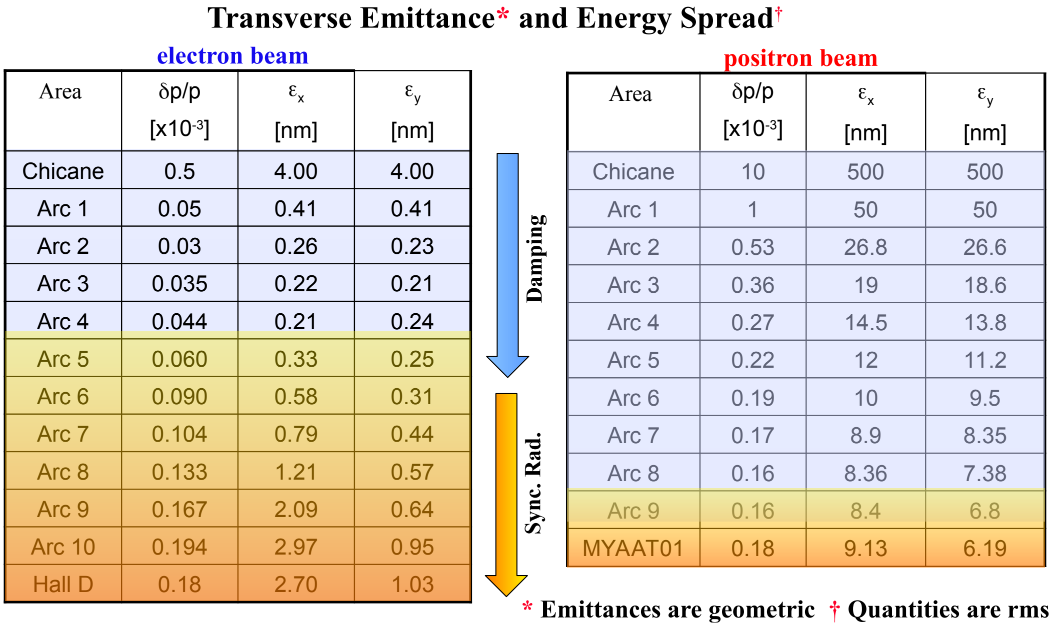

Transverse Emittance* and Energy Spread†

electron beam

Area	$\delta p/p$ [$\times10^{-3}$]	ε_x [nm]	ε_y [nm]
Chicane	0.5	4.00	4.00
Arc 1	0.05	0.41	0.41
Arc 2	0.03	0.26	0.23
Arc 3	0.035	0.22	0.21
Arc 4	0.044	0.21	0.24
Arc 5	0.060	0.33	0.25
Arc 6	0.090	0.58	0.31
Arc 7	0.104	0.79	0.44
Arc 8	0.133	1.21	0.57
Arc 9	0.167	2.09	0.64
Arc 10	0.194	2.97	0.95
Hall D	0.18	2.70	1.03

positron beam

Area	$\delta p/p$ [$\times10^{-3}$]	ε_x [nm]	ε_y [nm]
Chicane	10	500	500
Arc 1	1	50	50
Arc 2	0.53	26.8	26.6
Arc 3	0.36	19	18.6
Arc 4	0.27	14.5	13.8
Arc 5	0.22	12	11.2
Arc 6	0.19	10	9.5
Arc 7	0.17	8.9	8.35
Arc 8	0.16	8.36	7.38
Arc 9	0.16	8.4	6.8
MYAAT01	0.18	9.13	6.19

* Emittances are geometric † Quantities are rms

Figure 3: Comparison of simulated electron (left) and positron (right) beam properties [24]. The blue arrow indicates the prominence of acceleration damping effects, and the orange one corresponds to the dominance of the effects of synchrotron radiation.

3.3 Beam Polarimetry

While beam polarization is not required for the proposed measurement, it is desirable to know the beam polarization $|\lambda|$ to about 10% relative precision to cross-check the polarization-dependent asymmetry, $A^{e^+e^-}_{LR,RL,LL,RR}$, that can be extracted from data. The contribution from beam polarization to the RR and LL (LR and RL) asymmetries is proportional to $|\lambda| C_{1q}$ ($|\lambda| C_{2q}$), and is smaller than the contribution from C_{3q}.

Two of the three existing polarimetry techniques can be used for positrons with minimal modification: the first is the Mott polarimetry at the source which, in principle, will work for positrons up to 6 MeV of energy. The other is the Compton polarimetry in Hall A which, in principle, should also work without modification for positrons. We estimate that with the slightly larger intrinsic size of the positron beam, and assuming a beam current of 3 μA and a Compton laser power of 2 kW, an absolute $\pm 2\%$ measurement on the beam polarization can be achieved within an hour. Furthermore, Compton measurements can be performed non-invasively and provide continuous monitoring of the beam polarization.

3.4 Positron Beam in Hall A and Beam Monitoring System

All beamline magnets (prior to the beam entering Hall A) can in principle work for the positron beam if the magnet polarities are reversed. Hardware upgrades will be needed such that polarity reversal can be done quickly and consistently. Following the magnets, the beamline in Hall A consists of a Compton polarimeter, two Beam Current Monitors (BCM) between which an Unser monitor is located for absolute beam current measurement, a fast raster, a Moller beam polarimeter, and a number of Beam Position Monitors (BPM). All beamline monitoring components should in principle work for both positron and electron beams with minimal modifications. For example, stripline BPMs work for both positron and electron beams, though with each charge reversal the stripline likely needs to be physically reversed since the power flow is directional. The stripline BPM resolution at 1 μA current is 3 μm.

Beam energy in Hall A is measured by the "ARC" method, that is, the energy is determined using the beam bending angle and the $\int \vec{B} \cdot d\vec{l}$ value of the last dipole(s) in the Hall A beamline, just before the beam enters the hall. The beam energy can be determined to a relative 5×10^{-4} level using this method and is independent of the beam charge (provided the dipole magnet polarity is reversed). It is expected that a similar precision can be achieved for positron beams. In addition, one can use the BPM and magnet information in the ARC recorded in the EPICS data stream to correct for slight deviations of the beam from the central trajectory. This technique [25] was first used for the hypernuclei program in Hall C and can monitor the beam energy at the 10^{-5} level.

Beam current or intensity in the hall is measured by BCMs. The BCM is routinely calibrated with the Unser. However, at low beam currents (μA level) the Unser is noisy and Faraday cup measurements – invasive to Halls B, C, and D – are required to fully calibrate the BCM. We plan to carry out e^+ and e^- runs at about the same beam current to limit experimental systematic effects, such as DAQ deadtime and target density fluctuation. The BCM will be used to measure the beam intensity, though it is clear that one cannot control the difference in the beam intensity between e^+ and e^- runs to a high enough precision that is much smaller than the expected statistical uncertainty of the measured asymmetry.

Beam intensity and energy drifts with magnitudes smaller than what can be measured will contribute to systematic effects that cannot be directly corrected, see sections 4.2 and 4.3.

3.5 The Target and the Raster System

We plan to use a 40-cm long cryogenic liquid deuterium target, i.e. the same as for the SoLID PVDIS measurement [16]. Cryotargets are routinely used at JLab, with each cell typically of a cylindrical shape 1.3 inch in radius. The electron beam passes through an entrance "endcap" along the symmetrical axis of the cylinder, and scattered particle pass through the side walls or the exit "endcap". The entrance and exit "endcaps" as well as the side wall of the cryo-cells are made of 5-mil thick aluminum, which should be taken into account when calculating energy loss of particles. Then aluminum endcaps also contribute to background events, to be discussed in section 3.9. In addition to cryo targets, the target ladder includes optics carbon targets and a "dummy" target made of two pieces of aluminum identical to the endcaps of the cryo target, so that event contribution from the endcaps can be measured.

The slightly larger intrinsic size of the positron beam should not cause any problem on the target because the beam will be rastered to a minimum size of 2×2 mm and is still much smaller than the transverse size of the target cell. Based on experience, the density fluctuation of the liquid deuterium target due to beam heating (often referred to as "target boiling effect" though the liquid does not undergo a phase transition in reality) can have two effects on experiments: first is a reduction in density that can affect the precision of typical cross section measurements; second is an increase in the width of helicity pair-wise asymmetry above that expected from the counting statistics, which affects typical parity-violation measurements. We note that the second effect is irrelevant to the proposed measurement. The density reduction is found to be at the 10^{-3} level for a 1 to 5-μA beam [26] and a 2×2 mm^2 square raster, and depends on the raster size. We will control the raster size and other target conditions (fan speed, etc) to ensure any density effect cancels between e^+ and e^- runs to the first order. Any possible effect due to target density change can be treated as part of the luminosity difference, see section 4.2.

3.6 The SoLID Spectrometer and its Field

The Solenoid Large Intensity Device, or SoLID, is a large-acceptance device planned for Hall A. It has two basic configurations: the semi-inclusive DIS (SIDIS) and the PVDIS configuration. We plan to use the PVDIS configuration for the proposed measurement, see Fig. 4. This configuration will be used for the PVDIS measurement at a luminosity up to 10^{39} cm^{-2}s^{-1} (50 μA e^- beam on a 40-cm long liquid deuterium target). For PVDIS running at the 10^{39} cm^{-2}s^{-1} luminosity, a set of baffles (slitted shielding) will be used to reduce the background by 1-2 orders of magnitude, but reduce the acceptance of DIS electrons by approximately a factor three. Due to concerns of high background and related systematic effects (of both DIS and background events), we will be using the baffles for the proposed measurement.

To use the PVDIS setup for the e^+ beam run, the polarity of the solenoid magnet will be reversed such that the acceptance of the scattered positrons can be kept as close to that of the electrons as possible. The solenoid field for the positive polarity (for e^+ detection) has been calculated and it was found that the difference from the negative polarity (for e^- detection) is at no more than the 10^{-5} level and only for about 10 out of ten million points calculated. This is

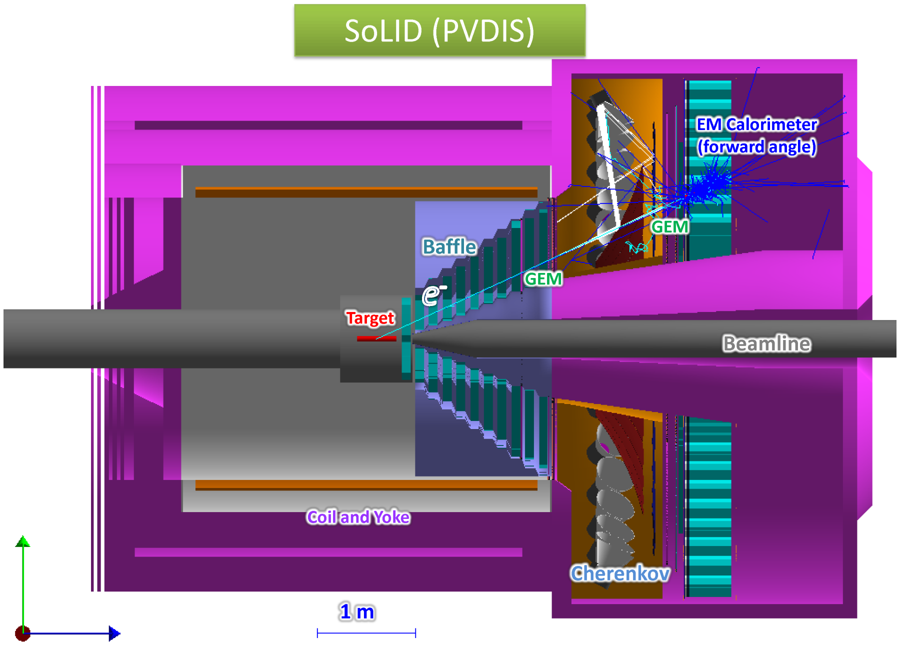

Figure 4: The planned Solenoid Large Intensity Device (SoLID) in its PVDIS configuration. The electron (or positron) beam enters from the left and incident on a 40-cm long liquid target. Scattered particles are detected by gas electron multiplication chambers, a gas cherenkov detector, and an electromagnetic calorimeter. A set of "baffles" (slitted shielding) will be used to reduce backgrounds.

in fact consistent with zero within the precision OPERA [27] can provide. When estimating systematic uncertainties, we will use 10^{-5} as the upper limit of the scattered particle's momentum difference between e^+ and e^- runs. Additionally, we present in Appendix C a high-precision field-mapping and feedback design, which is based on approaches used for the Fermilab Muon $g-2$ Experiment, that can potentially reach a $\Delta B/B = 10^{-6}$ field reproducibility and stability, making the effect of the SoLID magnetic field a negligible uncertainty for the proposed measurement.

3.7 Expected Rates and Electroweak Asymmetries

The expected DIS rates using SoLID PVDIS configuration with the baffles, a 40-cm long liquid deuterium target, and a 3 μA 11 GeV beam are shown in Fig. 5. The size of the electroweak component of the asymmetry $A_d^{e^+e^-}$ is calculated using Eq. (12) and both MMHT2014 [28] (NLO120 grid) and CT18 [29] (CT18NLO grid) PDFs. The average of $A_d^{e^+e^-}$ values using the two PDFs was taken as the central value, see Fig. 6. The expected statistical uncertainty of measured asymmetry with 80 PAC days of 11 GeV 3 μA beam data taking (split between e^+ and e^- beams) is shown in Fig. 7. Studies of the asymmetry value using the exact expression (Appendix A) and structure functions is underway but it does not alter significantly the size of the asymmetry (and more importantly the rates and statistical uncertainty).

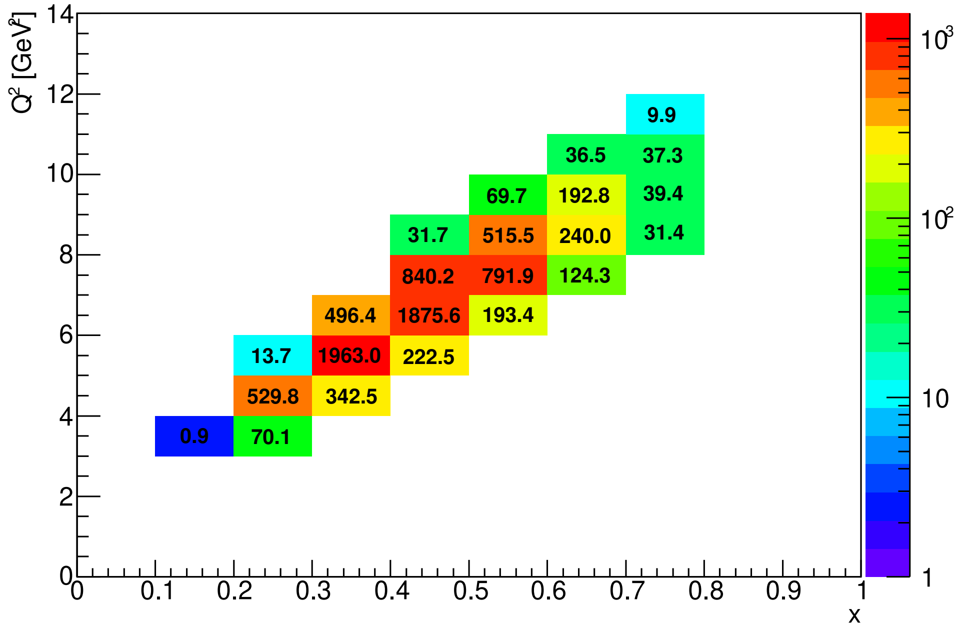

Figure 5: Simulated DIS rates in Hz for a 3 μA 11 GeV beam, a 40-cm liquid deuterium target, and SoLID in the PVDIS configuration. The baffles are in place. DIS cuts of $W > 2$ GeV and $Q^2 > 1$ GeV^2 have been applied.

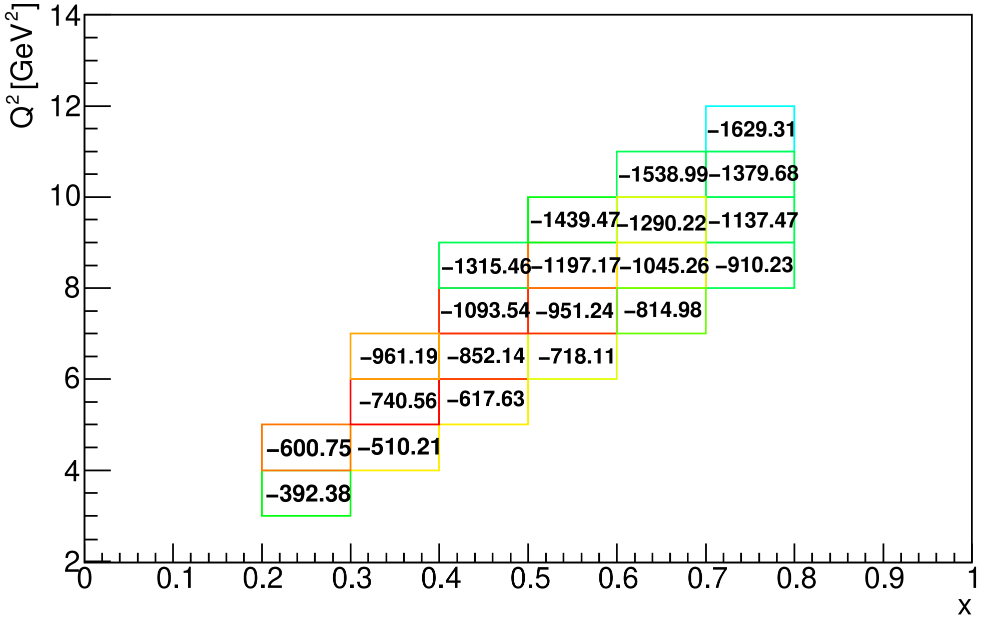

Figure 6: The electroweak contribution to the asymmetry $A_d^{e^+e^-}$ in ppm, averaged over MMHT2014 and CT18 PDFs.

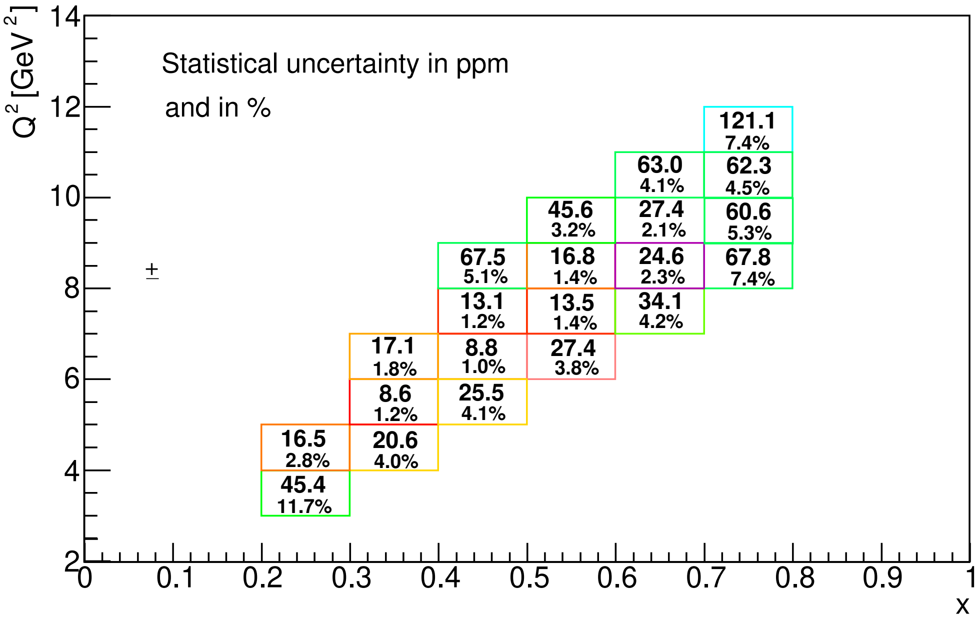

Figure 7: Statistical uncertainty in $A_d^{e^+e^-}$ in ppm (absolute) and in percent (%, relative). The beam time is 80 PAC days at 3 μA and the baffles are in place.

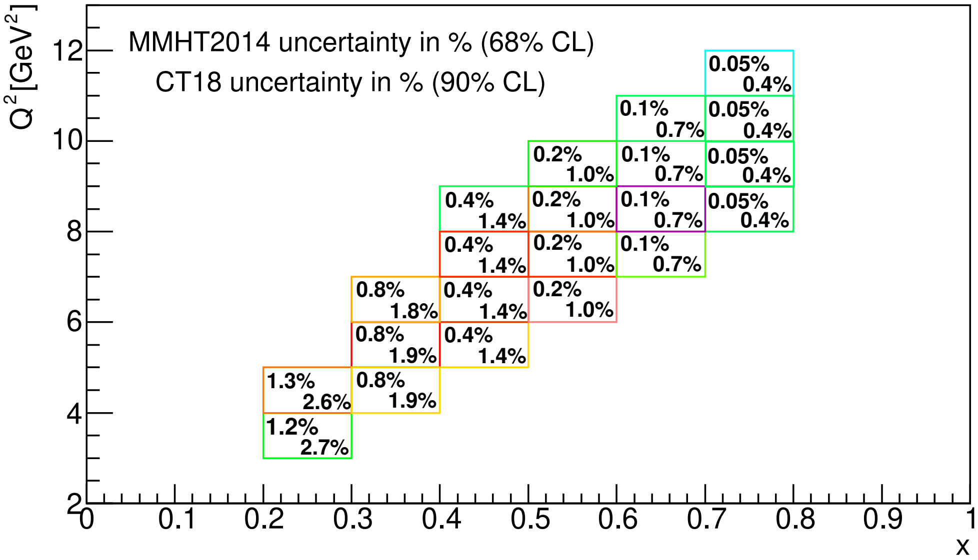

Figure 8: Relative uncertainty in $A_d^{e^+e^-}$ due to PDF in percent (%). In each kinematic bin (colored box), the two values are the uncertainties calculated from MMHT2014 eigenvectors (68% C.L., upper left) and CT18 eigenvectors (90% C.L., lower right). The difference between the two PDF sets are consistent with the uncertainties and are not shown.

Additionally, the uncertainty in the asymmetry calculation due to PDF sets were evaluated using the MMHT2014 (68% C.L.) eigenvectors and the CT18 (90% C.L.) eigenvectors. The relative sizes of these uncertainties are completely dominated by R_V and thus has a strong x

dependence, see Fig. 8. The differences between the asymmetry values calculated using the two PDF sets are consistent with these uncertainties and are not shown. In kinematic bins where the statistical precision is small, the PDF uncertainty becomes comparable to the statistical uncertainty.

3.8 Tracking and Data Acquisition

Particle detection in SoLID is accomplished by a Gas Electron Multiplication (GEM) detector for tracking, and a Light Gas Cherenkov (LGC) and an Electromagnetic Calorimeter (ECal) for particle identification (PID). For PVDIS configuration, the detectors are divided into thirty sectors, each equipped with their own data acquisition (DAQ) system utilizing fast readout with flash ADCs (FADCs). We will discuss tracking efficiency, accuracy and DAQ deadtime here, and will present PID in the next section.

3.8.1 Tracking Reconstruction

The tracking efficiency and accuracy of the GEM chambers are studied by running a full GEANT-4-based simulation for both DIS and background events. The GEANT-4 outputs are digitized using the SoLID-GEM digitization package, which simulates realistic GEM detector responses and convert the information into ADC signals on the readout strips. A tracking reconstruction package is used to analyze the ADC output. It first performs a GEM clustering in order to reconstruct the hit positions on the GEMs, and then performs a concurrent track finding and fitting using the Kalman Filter algorithm. Figure 9 shows the simulated GEM tracking efficiency and accuracy as functions of the beam current. The accuracy is defined as the fraction of GEM events for which the reconstructed tracks are the same as the incident DIS tracks.

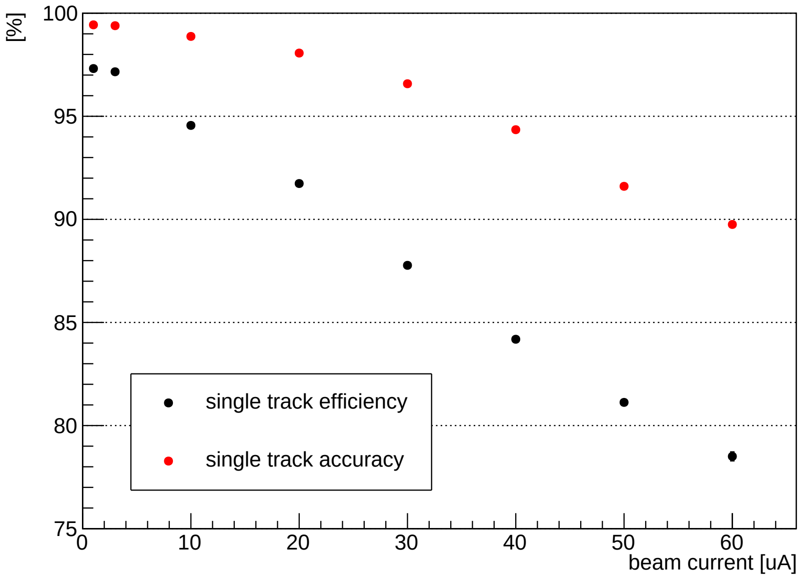

Figure 9: Simulated single-track efficiency and accuracy for GEM tracking vs. beam current.

For the 3 μA beam current planned for the proposed measurement, both single-track efficiency and single-track accuracy are very high and there is only a slight dependence on the current (event rate). The efficiency in principle will cancel out when forming yield asymmetries between e^+ and e^- runs, and any rate-dependence can be corrected. Furthermore, an overall difference in the efficiency between e^+ and e^- runs will cause a constant shift in the measured asymmetry, which can be absorbed into the "luminosity" term, see section 5.1. The only systematic effect that the tracking efficiency could cause on the extraction of C_{3q} is a possible difference in the (x, Q^2) dependence between e^+ and e^- runs. We have studied this effect by changing the pion background rate in the simulation to mimic the higher π^+/DIS ratio for e^+ runs than the π^-/DIS ratio for e^- runs, and found some dependence on (x, Q^2) in the tracking efficiency when the pion rates are increased by a factor of 10, although simulations with higher statistics are required to study the effect to higher precision or for smaller changes in the pion rate. We plan to measure the GEM efficiency for the full coverage during early running of SoLID experiments to confirm the simulation results, as well as with the e^+ beam, such that the efficiency difference between e^+ and e^- runs can be determined to a high degree of precision and corrected.

For accuracy of track reconstructions, the mis-identification of tracks causes the events to be sorted in incorrect kinematic bins and consequently a shift in the measured asymmetry. The effect on the measured asymmetry was studied by calculating the asymmetry based on reconstructed kinematics and compared with the simulated value without the background. It was found that the shift in the asymmetry is at no more than 0.2% relative, which can be further corrected by carefully studying the pileup of GEM signals. We will use an estimated value of 0.2% as the relative uncertainty in the measured asymmetry due to event reconstruction.

3.8.2 DAQ deadtime

Figure 10 shows the expected FADC deadtime as a function of per-sector rates, measured using pulser signals. The expected rate of the proposed measurement is about 1 kHz per sector, determined by the sum of the DIS rate and the online pion trigger with particle identification, and the DAQ deadtime is at the level of 2×10^{-4}. In real running of the experiment, the DAQ deadtime will be measured by sending a pulser of known frequency into the DAQ, and the ratio of accepted and initial pulser events provides a confirmation of the DAQ deadtime calculation. This deadtime correction will be applied to the measured yields. Because we will take data with e^+ and e^- at about the same current, we expect the deadtime correction to cancel to a large extent between the two data sets when forming the asymmetry. Additionally, the FADC deadtime is the same regardless of the kinematics of the events. Therefore, an overall deadtime difference between e^+ and e^- runs will cause a constant shift of the asymmetry that can be absorbed into the "luminosity" term when extracting C_{3q}, see section 5.1. In short, we expect the systematic uncertainty in the asymmetry measurement and C_{3q} extraction due to DAQ deadtime to be either negligible or will be taken into account in our analysis process.

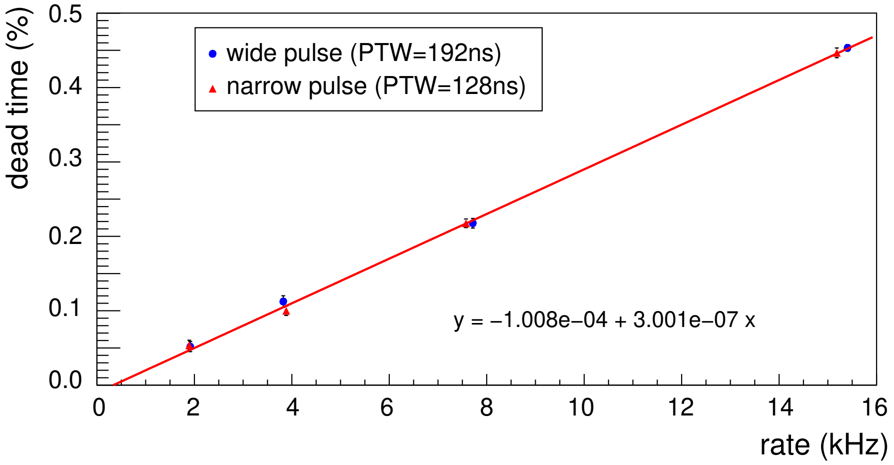

Figure 10: Measured FADC deadtime using a pulser system. The deadtime is shown in % as function of the pulser event rate in kHz, for two different signal widths. The system used to perform this measurement is part of the SoLID pre-R&D project currently ongoing at JLab.

3.9 Background Particles and Particle Identification

For any background in DIS, let f be the (average between e^+ and e^- runs) fraction of background to DIS event yields in production runs, $f \equiv Y_{bg}/Y_{\text{DIS}}$, and let A_{bg} be the asymmetry of the background. The DIS asymmetry can be obtained from the measured (total of DIS and background) asymmetry A_{total} as

$$A_{\text{DIS}} = (1+f)A_{\text{total}} - fA_{bg}\ . \tag{19}$$

This will cause not only a correction to the asymmetry but also an increase (widening) of the statistical uncertainty:

$$(\delta A_{\text{DIS}})^2 = (1+f)^2(\delta A_{\text{total}})^2 + f^2(\delta A_{bg})^2 + (\delta f)^2(A_{\text{total}} - A_{bg})^2, \tag{20}$$

where δf and δA_{bg} are the uncertainties of the background. In PVDIS, the background does not have a large asymmetry and the widening of the statistical uncertainty is very small. This is different for $A^{e^+e^-}$ because the asymmetries of charged pion and proton background are large. We discuss charged particle and pair production background separately below. We will also discuss about events scattering off the cryo target endcaps.

3.9.1 Charged Particle Background and Particle Identification

The typical background in DIS are photo-produced charged pions. For SoLID, electrons are identified using a light gas Cherenkov detector and the electromagnetic calorimeter (ECal). The ECal's particle identification (PID) performance optimized for SoLID PVDIS setting is shown in Fig. 11. Combined with the estimated charged pion rate, the fraction of pion contamination with ECal PID is shown in Fig. 12 for the ratio π^+/e^+ in e^+ runs. As one can see that the π/e contamination with ECal alone is expected to be below 2% for most of the DIS region, though it

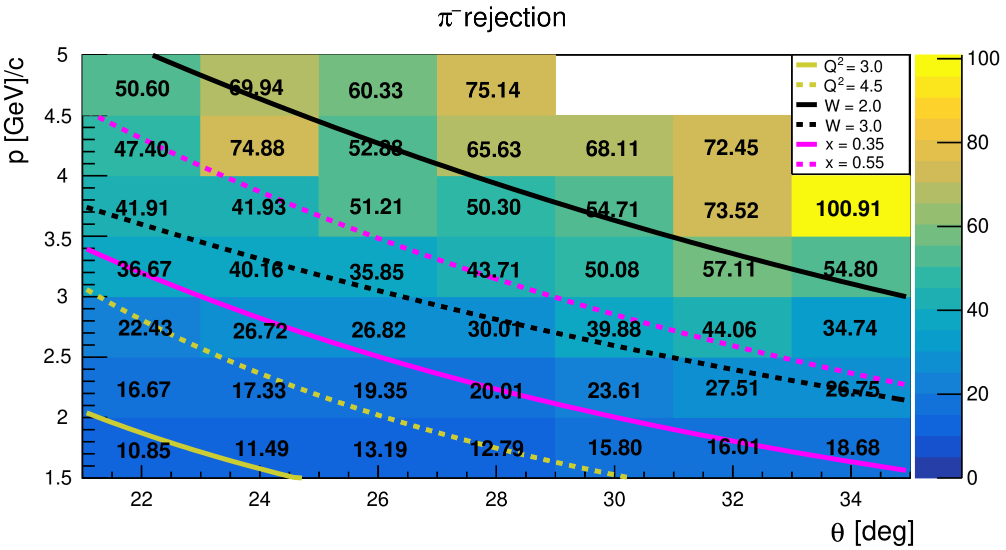

Figure 11: SoLID electromagnetic calorimeter (ECal) pion rejection factor with full background simulation for an average electron detection efficiency of 93%. The rejection can be improved with more stringent PID cuts though it will lower the electron efficiency slightly. For DIS region ($W > 2$ GeV and $x > 0.35$), the rejection factor varies between 20 and 50. With the addition of the gas cherenkov, pions will be suppressed by an additional factor of 100 or more.

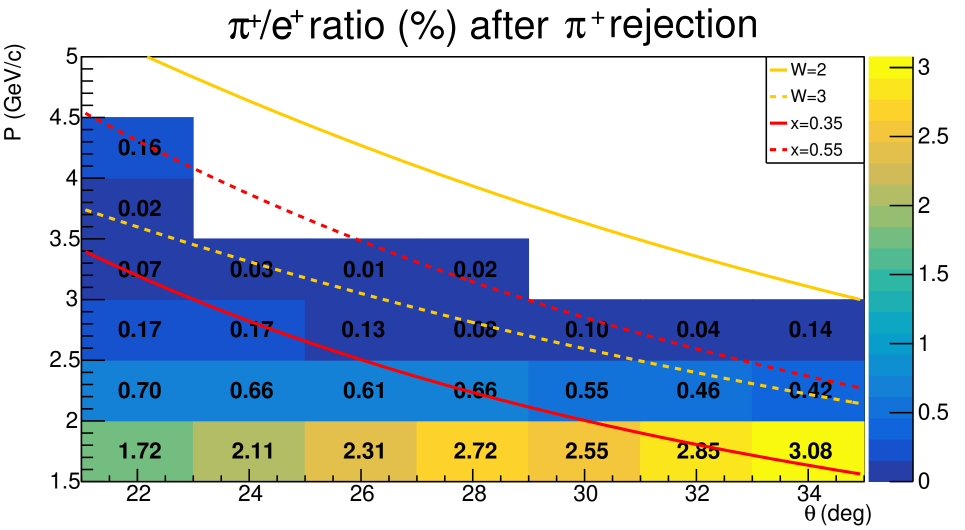

Figure 12: Simulated pion contamination in DIS event sample with ECal PID cuts, plotted on a grid of the scattering angle θ (horizontal axis) and the scattered particle's momentum (vertical axis). For offline analysis, Cherenkov cut will be applied to bring the contamination down by at least another factor 100.

can be up to 5% at low x. Once Cherenkov PID cuts are applied, the contamination fraction will be further suppressed by factor of 100 or more, bringing it down to 10^{-4} to 10^{-3} level.

The asymmetry of charged pions can be determined from the same experimental setup as DIS events, by accepting events that satisfy the pion signal type (i.e. a pion trigger, a common practice utilized by DIS experiments). Let the raw pion to electron ratio be $r_{\pi/e}$, the pion contamination fraction in DIS events would be $f_{\pi/e} = r_{\pi/e}/\eta_\pi$ where $\eta_\pi > 10^4$ is the pion rejection factor provided by ECal and Cherenkov combined. We assume that every one out of PS (an integer known as the "pre-scale" factor of the pion triggers) raw pion events will be collected and the asymmetry measured, the uncertainty of the charged pion background asymmetry is $\Delta A_\pi = \frac{1}{f_{\pi/e}\eta_\pi N_e/PS}$ and Eq. (20) becomes

$$(\Delta A_{\rm DIS})^2_{\pi\ bg} \quad = \quad \frac{1}{N_{\rm DIS}} + \frac{f_{\pi/e}}{\eta_\pi N_{\rm DIS}/PS} + (A_{\rm total} - A_\pi)^2(\Delta f_{\pi/e})^2\,, \tag{21}$$

where $N_{\rm DIS}$ is the total number of DIS events collected and we have used $\delta A_{\rm total} = 1/N_{\rm total} = 1/N_{\rm DIS}/(1+f_{\pi/e})$. Since $f_{\pi/e} < 10^{-3}$, $\eta_\pi > 10^4$, the second term on the RHS of the above equation can be omitted and we only need to consider the third term. Additionally, from previous data [30], charged pion background has a $\approx 30\%$ asymmetry between e^+ (π^+ background) and e^- (π^- background) settings. Since $A_{\rm total}$ is at $10^{-2\ \rm to\ -3}$ level, we can ignore the $A_{\rm total}$ in the parentheses and

$$(\Delta A^{\rm DIS})^2_\pi \quad \approx \quad \frac{1}{N_e} + (A_\pi)^2(\Delta f_{\pi/e})^2. \tag{22}$$

The value of $f_{\pi/e}$ can usually be determined to percent level, bringing $\Delta f_{\pi/e}$ to 10^{-5} (absolute). Relative to the goal of the measurement $\Delta A^{\rm DIS}$ which is about 10 ppm or larger, the widening of the uncertainty is not significant in most of the kinematic bins. The above method can also be applied to the proton background, which has similar PID efficiency, though is only present for e^+ runs and thus has a 100% asymmetry. The proton background rate was estimated using Wiser's fit [31]. We will use Eq. (22) to calculate the effect on the asymmetry uncertainty from both charged pion and proton backgrounds.

3.9.2 Pair Production Background

Pair production contamination for the proposed kinematics has been estimated, see Fig. 13. The π^0 cross section was calculated by taking the average of π^+ and π^- productions off a proton target from Wiser's fit [31], scaled by $A^{0.8}$ with $A = 2$ for the deuteron, and followed by the decays of $\pi^0 \to 2\gamma$ and $\gamma \to e^+e^-$. The method was found to be in good agreement with the pair production cross section measured in the Hall A d_2^n experiment at 6 GeV [30] and the more recent Hall C F_2 experiment at 11 GeV [32]. For the systematic effects of pair production we can follow a similar method as for charged pions. The main difference is that the pair production is caused by π^0 decay, and π^0 production is expected to be the same for e^+ vs. e^- beams, i.e. $A_{\rm pair} \approx 0$. We can assume $A_{\rm pair} \lesssim 1\%$ just to be conservative but the second term on the RHS of Eq. (20) will be the dominant one.

We will spend some time taking data with the SoLID in reversed polarity – e^+ detection for e^- beam and e^- detector for e^+ beam, traditionally called "positron runs" but we avoid using

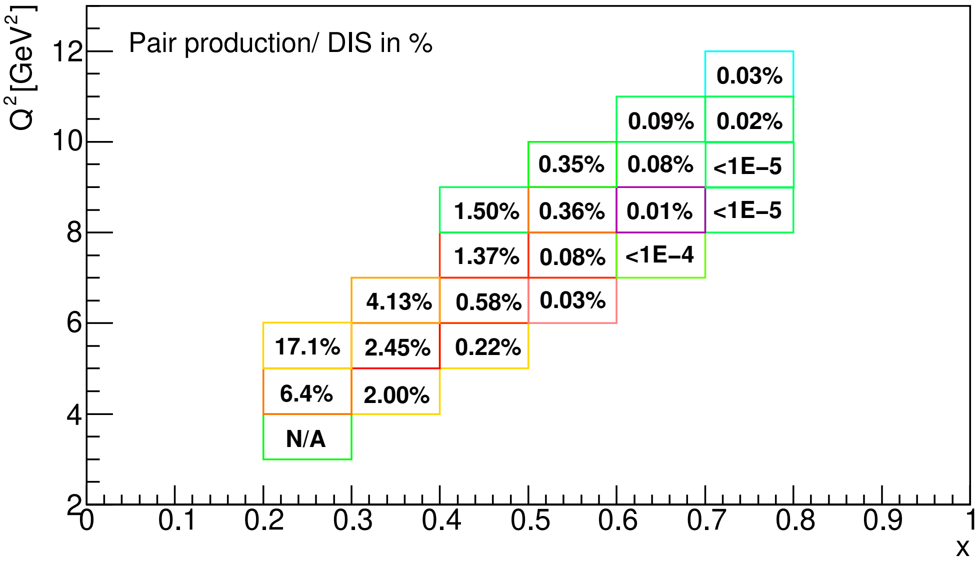

Figure 13: Estimated ratio of pair production background to DIS rate in %.

this term in this document – and denote the ratio of reversed polarity over production runs as α. Starting from Eq. (20) and letting $\Delta A_{\text{pair}} = 1/\sqrt{N_{\text{pair}}} = 1/\sqrt{\alpha f_{\text{pair}} N_{\text{DIS}}}$ where N_{pair} is the expected pair production event count from reverse-polarity runs, we obtain:

$$(\Delta A^{\text{DIS}})^2_{\text{pair}} \;=\; \frac{1}{N_{\text{DIS}}} + \frac{f_{\text{pair}}}{\alpha N_{\text{DIS}}} + (A_{\text{pair}})^2 (\Delta f_{\text{pair}})^2 \,. \tag{23}$$

Now one can see the second term will contribute if f_{pair} is at the percent level. To keep the widening of the uncertainty under control, we will set $\alpha = 0.1$, i.e. we will spend 10% of beam time on reverse-polarity runs. Additionally, we assume f_{pair} can be determined to 3% relative precision and take into account the third term assuming $A_{\text{pair}} \lesssim 0.01$. Both effects on the widening of the asymmetry uncertainty will be taken into account in our analysis.

3.9.3 Scattering from Target Endcaps

As described in section 3.5, the cryotarget "cell" typically has entrance and exit "endcaps" made of 0.5 mil (less than 0.15-mm) of aluminum. One can measure event count contribution from the aluminum endcaps using a "dummy" target – a target made of two bare pieces of aluminum placed at the same location as the cryo target endcaps. However, dummy target measurements do not collect enough statistics to measure aluminum asymmetry precisely and one must rely on calculations to estimate its effect. We note that because aluminum (^{27}Al) is almost isoscalar, the e^+e^- asymmetry should be similar to that of the deuteron. Using parton model for the proton and the deuteron asymmetries (see Appendix A), we found $A^{e^+e^-}_{\text{Al}}$ to differ relatively from $A^{e^+e^-}_d$ by 0.2% at low x to 0.8% at high x. We did not consider EMC effects which can change these ratios slightly. Considering the material thickness ratio of 5 mil of aluminum to 40-cm long liquid deuterium (0.169 g/cm^3 in density), the endcaps contribute to about 1% of DIS event counts and the effect on the measured asymmetry is therefore less than 0.01% relative and is negligible.

4 Data Analysis Procedure and Systematic Uncertainties

In this section we first outline the analysis procedure towards extractions of $A_d^{e^+e^-}$ from data. From the asymmetries we will also form the structure function $F_3^{\gamma Z}$ using world data on F_1^γ as inputs. Then we focus on systematic uncertainties that enter the analysis procedure and interpretation of the measured asymmetries. Systematic effects caused by specific components of the experimental setup were already described in the previous section and are only summarized here when relevant. Effects such as differences in the luminosity, beam energy, and (if applicable) momentum of the scattered DIS events between e^+ and e^- runs, are discussed. These effects will be dealt with using a multi-parameter fit, see section 5.1. We will dedicate section 4.5 to radiative effects (bin migrations), section 4.6 to Coulomb correction, section 4.7 to QED higher order contributions, and section 4.8 to higher twist effects.

4.1 Analysis Procedure

1. From data collected with each beam, we first form the yields

$$Y^\pm = \frac{N^\pm}{Q^\pm \eta_{\text{eff}}^\pm LT} , \tag{24}$$

   where the superscript represents the sign of the beam particle. N is the event count of interest, Q the accumulated beam charge measured by the BCM (section 3.4), and η_{eff} is the SoLID tracking and detection efficiency (section 3.8). The DAQ livetime is assumed to be nearly 100% as expected for the FADC readout (section 3.8). Yields can be formed for DIS, charged background (pions and protons), and for pair production background using reverse polarity runs.

2. Then we form the measured asymmetry

$$A_{\text{meas}} = \frac{Y^+ - Y^-}{Y^+ + Y^-} , \tag{25}$$

   again on both DIS and charged particle background events (charged pion and protons) using the hadron triggers. Similarly, the asymmetry of the pair production background is formed from data collected with reversed polarity runs.

3. To form the DIS asymmetry A_{DIS}, we subtract the background asymmetries from A_{meas} using Eq. (19), where the background contamination fraction $f = Y_{\text{bg}}/Y_{\text{DIS}}$ with yields Y calculated in step 1.

4. Now we can apply corrections for bin migration and subtract QED higher-order contributions from the asymmetry. This will provide the asymmetry data that enter the multi-parameter fit, Eq. (27) of section 5.1.

5. Once we obtain the fitted results for the beam energy and luminosity differences, one can correct the asymmetry with these two effects and obtain the electroweak asymmetry $A_d^{e^+e^-}$.

6. Lastly, we form $F_3^{\gamma Z}$ using the asymmetry $A_d^{e^+e^-}$ and Eq. (13), with the world F_1^γ data as inputs.

4.2 Difference in Luminosity

As described in section 3.4, the beam current in Hall A is measured by the BCM and calibrated by the Unser or Faraday cup. While the beam charge in principle is corrected for in the yield calculation in Eq. (24), the BCM and the Unser system can have slow drifts over time, causing an asymmetry between the measured e^+ and e^- yields that can't be accounted for through charge normalization. Since we plan to measure the asymmetry $A_d^{e^+e^-}$ to 10^1 to 10^2 ppm level, it is unlikely that this slow drift in BCM between e^+ and e^- runs can be controlled at a precision that is negligible compared to the statistical uncertainty. In addition, the different beam sizes can cause different target density change (boiling effect) between e^+ and e^- runs. We will refer to the combined effect of the BCM drift and target density fluctuation as a "luminosity" difference between e^+ and e^- runs, which cannot be directly measured and must be obtained by fitting the asymmetry data. As described in section 3.8, this "luminosity" term can also absorb any kinematic-independent differences in the tracking efficiency and DAQ deadtime between e^+ and e^- runs. In the following we will assume this luminosity difference can be up to 1% between e^+ and e^- runs.

4.3 Difference in the Beam Energy and Scattered Lepton Momentum

Similar to the luminosity, the energy difference between e^+ and e^- beams cannot be controlled to below a relative $10^{-5 \text{ to } -6}$ level using existing beam energy measurements, though one can argue that for the typical energy resolution of 5×10^{-4}, there must be cancellation in the systematics of energy measurements between e^+ and e^- beams and thus the energy difference can be much smaller. However, we found that unless the difference is known to 2×10^{-5} or better, one must account for the possible energy shift when analyzing the asymmetries.

A shift in E_{beam} is amplified in the observed rates because of the Q^2 dependence of the cross section. Similarly, if the momentum of the DIS particles differs slightly between positive and negative polarity runs of SoLID, it will cause a difference in the observed rate, though studies of the SoLID field map show that the difference in the SoLID fields is well below the 10^{-5} level (section 3.6) and we have designed a field mapping device to control the field repeatability and stability to below 10^{-5} (Appendix C). In the following, we will assume the difference in the beam energy is at most 5×10^{-4} (relative), and that in the DIS particles' momentum at most 1×10^{-5} (relative). Fortunately, kinematic dependence of these effects helps to separate them from electroweak contributions to the asymmetry.

4.4 Background Contamination

While the response of the SoLID magnet and detectors does not depend on the particle charge, e^+ and e^- runs will have different backgrounds. We have simulated the π^-/e^-, π^+/e^+ and p/e (proton over DIS events) ratios and found they are comparable. Because we expect high performance from the PID detectors, and the SoLID DAQ can provide hadron triggers for measuring the asymmetries of these background events, we expect the effect from both charged pion and proton backgrounds to be very small. This was indeed the case for the 6 GeV PVDIS experiment [7]. Nevertheless we will use Eq. (22) to calculate the widening of asymmetry uncertainties. Compared to charged pions and protons, pair production background cannot be distinguished from DIS leptons. As described in section 3.9.2 and assuming 80 days of production beam time, we will spend 8 days to run SoLID at reverse polarity (negative polarity for e^+ beam and vice versa) to measure the pair production background. We will use Eq. (23) to calculate the widening of the asymmetry uncertainties and fold this into the multi-parameter fit.

4.5 Radiative Corrections (Bin Migration)

In typical JLab experiments, radiation effects due to energy loss of incoming and scattered electrons passing through material shift the kinematics at the reaction point (vertex) towards lower Q^2 and higher x. This effect is often studied by running a simulation tool with the radiation effect turned on, and kinematic shift of the reaction vertex (bin migration) is corrected. To assist such "radiative corrections", data will be taken with a 6.6 GeV beam to ensure the accuracy of the calculation at the vertex. This is particularly important for the proposed measurement because of the large asymmetry caused by higher-order QED contributions (see next section). Figure 14 shows the distribution of reaction vertices for 11 GeV production with radiation effect turned on, and the x and Q^2 coverages of the 6.6 GeV runs. One can see that the 6.6 GeV runs will cover most of the low Q^2 region that migrates into the production data due to radiation effects.

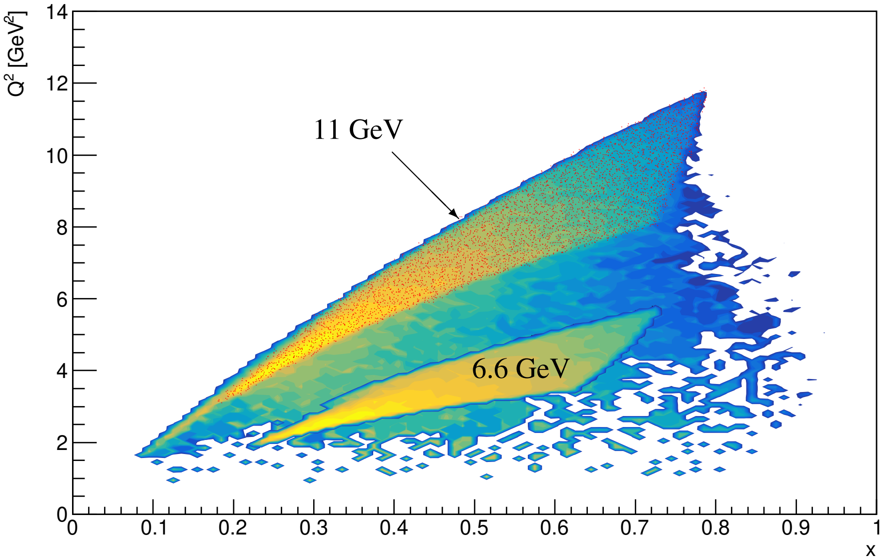

Figure 14: Bin migration for 11 GeV productions runs (the colored contours show the vertex kinematics) and the kinematic coverage of 6.6 GeV runs (lower yellow contour, vertex only).

Detailed rates and statistical uncertainty estimate for the 6.6 GeV run are shown in Figs. 15 and 16. The asymmetry shown is from the electroweak contribution only. The PDF uncertainties are at less than 2% level and are omitted here. QED higher-order corrections can be carried out similarly to the 11 GeV run. The ratio of pair production over DIS is found to vary between 10^{-3} and 2%, and thus it is not necessary to run reverse-polarity runs for 6.6 GeV.

Following the prescription of [7] where the uncertainty due to bin migration was found to be at 0.4% level for the $Q^2 = 1.9$ (GeV)^2 point, we estimate 10 days of running at 6.6 GeV will be

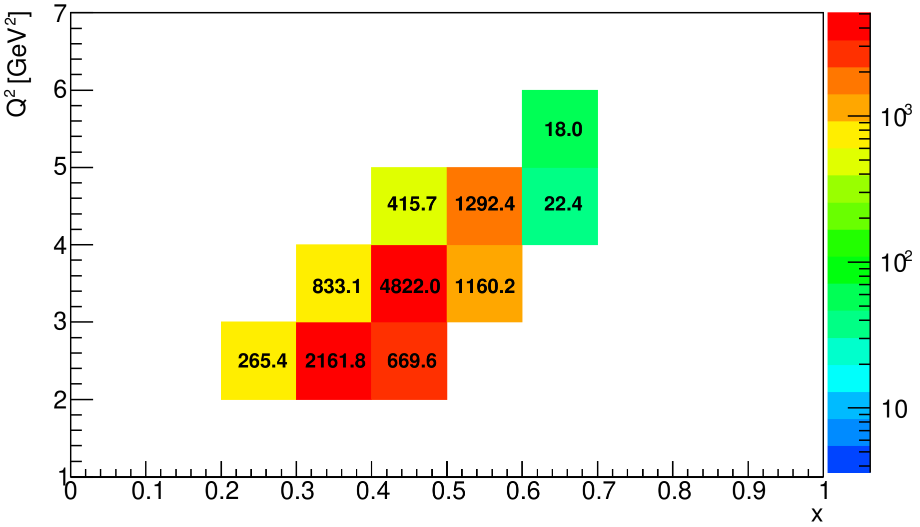

Figure 15: Simulated DIS rates in Hz for a 3 μA 6.6 GeV beam, a 40-cm liquid deuterium target, and the SoLID in the PVDIS configuration. The baffles are in place. DIS cuts of $W > 2$ GeV and $Q^2 > 1$ GeV^2 have been applied.

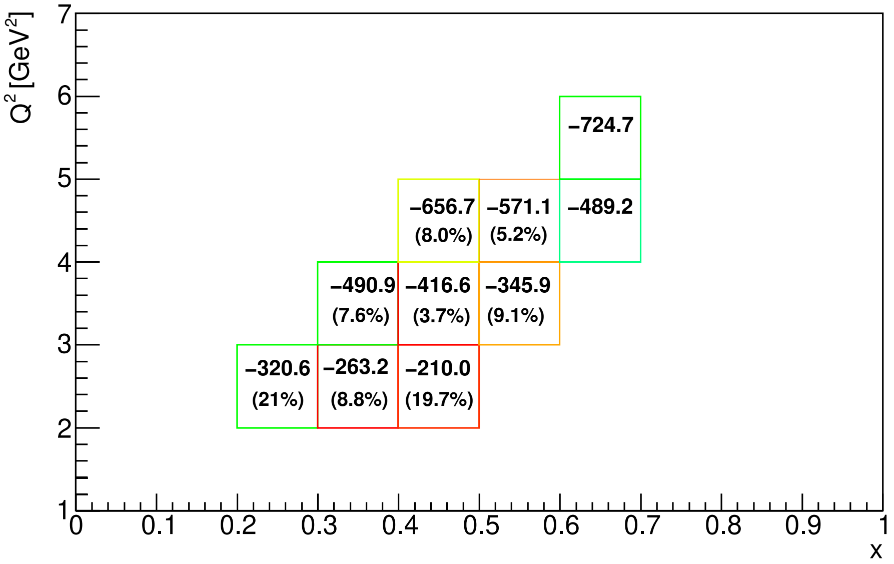

Figure 16: Values of $A_d^{e^+e^-}$ in ppm for the 6.6 GeV run, calculated from MMHT14 and CT18. The expected relative statistical uncertainties in percent are shown for kinematic bins where they are below 30%. The beam time is 10 PAC days at 3 μA and the baffles are in place.

sufficient to constrain the uncertainty due to bin migration to a sub-% level on the asymmetries. This does not include the uncertainty due to QED higher-order corrections for the 6.6 GeV runs, which should be treated separately, see section 4.7.

4.6 Coulomb Correction

Once the incident positrons (electrons) approach the target nucleus, they are decelerated (accelerated) by the nuclear Coulomb field. Similarly, outgoing positrons (electrons) are accelerated (decelerated). Such Coulomb effects, commonly known from differences between energy spectra of nuclear $\beta^{\pm}$ decay, were measured in electron scattering [33]. The effect of the nuclear Coulomb field in lepton scattering can be approximated as a change in the incident (beam) energy $E_{b,\text{eff}} = E_b - V_C$ and a change in the scattered energy $E'_{\text{eff}} = E' - V_C$, where V_C is the value of the effective Coulomb potential energy seen by the lepton during the scattering process. In [33] the size of V_C was determined by comparing e^+ and e^- quasi-elastic scatterings off a ^{12}C and a ^{208}Pb target, and the data were fitted to yield

$$|V_C| \;=\; \frac{(1.27 \pm 0.10)\text{MeV fm}}{\langle r^2\rangle^{1/2}} Z, \tag{26}$$

where Z and $\langle r^2\rangle^{1/2}$ are the atomic number and the RMS radius of the target nucleus, respectively. For the deuteron, $Z = 1$ and using $\langle r^2\rangle^{1/2} \approx (1.2\ \text{fm})A^{1/3} = 1.51$ fm, we obtain $|V_C| = 0.84 \pm 0.066$ MeV, i.e. effective shifts of the beam energy at the $(7.6 \pm 0.6) \times 10^{-5}$ level (for 11 GeV), and the scattered lepton's momentum at the $(42 \pm 3.3) \times 10^{-5}$ level (for 2 GeV). In a more recent work [34], Coulomb correction was approximated using the effective momentum method similar to [33]. Because the Coulomb effect correction is small, the approximation using the effective energy (momentum) to correct it should be sufficient and can be incorporated into the procedure described in section 4.5.

4.7 Higher-order QED Contributions

At the level of one-boson exchange (QED LO), the e^+ and e^- DIS cross sections are identical. At higher orders, two-boson exchange corrections contain contributions with opposite signs for e^+ and e^- scattering and cause a difference in the cross sections. For elastic scattering and inelastic scattering at low Q^2, the NLO corrections are not well understood and the so called "two photon exchange" (TPE) process where the two photons are both "hard" (of similar energy) is believed to be the reason behind the discrepancy in the measured proton form factor ratio G_E^p/G_M^p data between the cross section (Rosenbluth) method and the polarization transfer method. For a review of the TPE topic see [35].

For DIS, the NLO processes (including TPE) are straightforward to calculate. We have performed a NLO QED calculation of the e^+ vs. e^- DIS asymmetry on the deuteron. The program used is a Monte Carlo event generator developed for HERA [36, 37, 38] and modified for the fixed-target setting of the proposed measurement. The asymmetry $A_d^{e^+e^-}$ at the LO level (only one-photon and one-Z exchanges) is consistent with calculations using Eq. (10) to within 3%. A thorough check will be performed in future studies to pin down the origin of this difference. The NLO calculation includes the NLO level vertex diagrams, box diagrams with an additional photon and one-photon radiation from leptons and quarks. Everything was calculated for DIS, i.e. in the parton model, and with MMHT PDFs. The size of QED NLO corrections from this calculation will be given in Fig. 17.

If we assume the parton model to be a valid framework, then the accuracy of QED corrections is limited only by the omission of higher-order terms and can reach a high precision. While higher-order calculations involving hadronic structure beyond the parton model, including quark-quark correlations, are more difficult to carry out and are model-dependent, we note that some of these effects have been categorized as the ”higher-twist” effect, to be discussed next. Should the proposed measurement be approved, higher order QED processes, along with $O(\alpha_S)$ QCD corrections, will be studied carefully. Our goal is to calculate the higher order corrections (QED and QCD) to 1% level or better, which should be limited mostly by the uncertainty of the input PDFs.

As an alternative to the standard radiative correction approaches that have been used in the literature, a new approach [39] has been developed recently based on the simultaneous factorization of both QED and QCD effects, which allows corrections to be computed in a systematically improvable way. Currently the formalism has been worked out at $\mathcal{O}(\alpha^2)$ in the electromagnetic coupling; higher order contributions, at which TPE effects will enter, are being computed [40] and should be available by the time the experiment proposed here would run.

4.8 Higher-Twist Effect

Higher-twist (HT) effects refer to corrections suppressed by powers of $1/Q^2$. An example are processes with correlated pairs of quarks or gluons inside the nucleus. The HT effects modify the asymmetries through a change in the absorption cross-section ratio R^γ in Eqs. (14), or through changes in the structure functions F_1^γ and $F_3^{\gamma Z}$. The effect on R^γ was estimated in [41] and was found to be negligible. Studies of HT effects on the γZ structure functions can be dated back to the SLAC PVDIS (E122) experiment [42, 43], and more recently in [44, 45, 46]. These works all focused on the C_{1q} ($F_1^{\gamma Z}$) contribution to the PVDIS asymmetry. Though irrelevant for the proposed measurement, they all found the HT effects on the ratio $F_1^{\gamma Z}/F_1^\gamma$ to be small.

There is no theoretical estimation of the HT effects on $F_3^{\gamma Z}$ that is directly relevant for the $A_d^{e^+e^-}$ asymmetry. We consider two approaches. The first is to use data on the neutrino structure function F_3^ν, for which the HT term was extracted as $xF_3^\nu = xF_3^\nu + H_3^\nu/Q^2$ [41, 47]. Because the deuteron structure function $F_{3,d}^\nu = (u_V + d_V + 2s - 2\bar{c})$ (per-nucleon as in [41]) has a similar quark content as $F_{3,d}^{\gamma Z} = u_V + d_V + \frac{4}{3}c_V + \frac{2}{3}s_V$ (per-nucleus as in this document), one can use H_3^ν as an estimate of the HT effects on $F_3^{\gamma Z}$. Then we applied CJ15's fit for the HT effect of F_2^γ [48]. We found the asymmetry to shift by a few percent (relative) and the shift has a x dependence. The net effect of this shift is a change in the asymmetry vs. Q^2 slope that significantly affects the interpretation of the asymmetry in terms of C_{3q}. Compared to the HT effects of $F_{1,2}$ structure functions, the value of H_3^ν is much larger and the uncertainty is also rather large. There is unfortunately no new data on differential (anti)neutrino-nucleus DIS cross-sections that can be used to improve the analysis in [41], though there is a plan to improve the neutrino data precision [49].

In the second approach, we note that it is a common practice in parameterizations of structure function data to assume the same HT effects on $F_3^{\gamma Z}$ as on $F_{2(1)}^\gamma$, rendering a full cancellation of HT effects on the asymmetry. For a conservative estimate, we apply H_2, the HT term for F_2^γ structure function from CJ15 to our kinematic coverage [50] and assume the same effect on the $A_d^{e^+e^-}$ asymmetry, i.e. no cancellation from possible HT effects of $F_3^{\gamma Z}$. We found the shift in the extracted C_{3q} is about a quarter in size compared to the first approach, and the uncertainty in the shift using CJ15's uncertainty on H_2 is negligible.

We will present quantitative results of both approaches in section 5.1. Note that the HT effects mostly affect the extraction of C_{3q} and not $F_3^{\gamma Z}$.

4.9 Error Budget Summary

For convenience, in Table 1 we list a few experimental uncertainties that are common to all kinematic bins. The uncertainties due to Q^2 determination is from [16] (SoLID PVDIS measurement) as we will utilize the same SoLID setup. The uncertainty due to bin migration is deduced from 6 GeV PVDIS results (section 4.5), and those due to event reconstruction and DAQ deadtime were discussed in section 3.8. The effect from the DAQ deadtime is considered negligible in the extraction of the electroweak contribution of the asymmetry because the same deadtime applies to all events. The full uncertainty includes also the statistical uncertainty (Fig. 7), uncertainty due to background correction (Eqs.(22) and (23)), PDF uncertainty (Fig. 8), QED higher order contributions (sections 4.7), and higher-twist effects (section 4.8, for C_{3q} extraction only).

Table 1: Error budget table. See text for details.

Source	Uncertainty on Asymmetry
Q^2	0.2% relative
Bin migration	0.4% relative
Event reconstruction	0.2% relative
DAQ deadtime	negligible if the same for all events

5 Projected Results

In this section we provide projected results on C_{3q} and $F_3^{\gamma Z}$ and also make a connection with two-photon-exchange physics at the end.

5.1 Extraction of $2C_{3u} - C_{3d}$ Using a Multi-Parameter Fit and a Monte Carlo Method

In Fig. 17 we plot the expected results on the electroweak $A_d^{e^+e^-}$, calculated using Eq. (12) and normalized by $Y(y)R_V/(1+R_S/5)$, as functions of x and divided into Q^2 bins. A small step size in x is used to emphasize the kinematic dependence of experimental effects. The EW contribution calculated using the parton-model expression, once normalized by $Y(y)R_V/(1+R_S/5)$, is essentially a constant at a fixed value of Q^2 (the effect of R_C can be ignored at JLab energy). In Fig. 17 we also show two calculated experimental effects: $\Delta A_{Eb,\max}$, contribution to the asymmetry if the beam energy of e^+ is lower than e^- by 5×10^{-4} (relative); and $\Delta A_{Ep,\max}$, if the magnetic field of SoLID in the positive polarity differs from that at negative polarity by 1×10^{-5} (relative). Additionally, QED NLO contributions from the calculation described in section 4.7 are shown, multiplied by factor $1/5$ to fit into the figure. One can see that the experimental effects have a drastic x dependence, which will be used below to separate them from the electroweak contribution to the asymmetry. We also studied the Q^2 dependence in fixed x bins but the effects are not as prominent, though more careful studies can be done to perfect the fitting procedure.

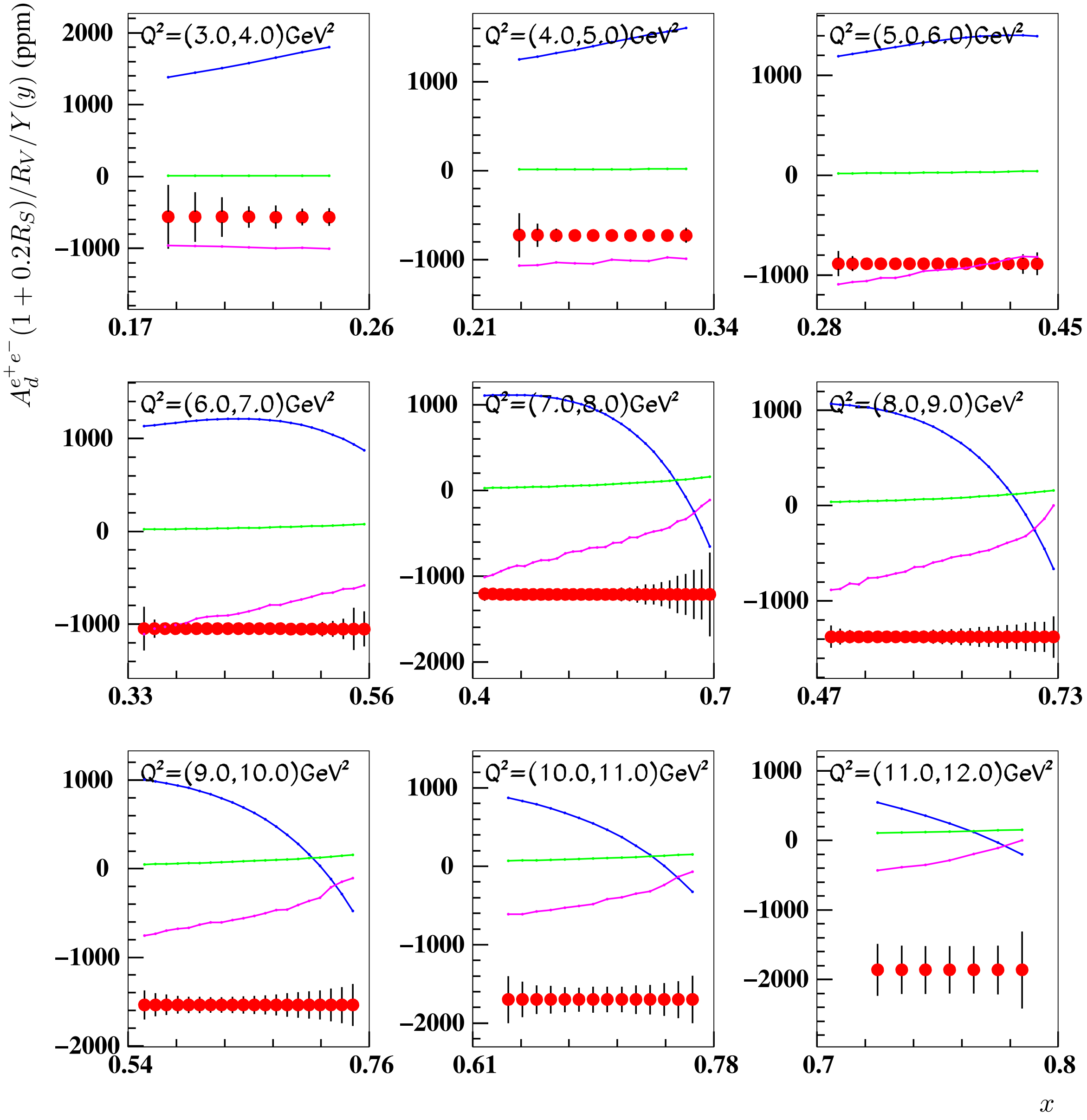

Figure 17: Expected size for the EW contribution to the asymmetry $A_d^{e^+e^-}$ divided by $R_V Y(y)/(1+0.2R_S)$ (red solid circles) vs. x for each Q^2 bin. The error bars are expected statistical uncertainties. The blue curves show ΔA_{Eb}, the expected shift in the asymmetry if the beam energy of e^+ is lower than e^- by 5×10^{-4} (relative), and the green curves show ΔA_{Ep}, the expected shift in the asymmetry if the magnetic field of SoLID in the positive polarity differs from that at negative polarity by 1×10^{-5} (relative). A difference in the luminosity between e^+ and e^- runs (not shown) will cause a nearly uniform shift of the measured asymmetry in all bins. The QED NLO contribution is shown by magenta curves after being multiplied by factor $1/5$.

5.1.1 The Fitting Method

We generated "pseudo" data by assuming three random numbers that apply to all bins: d_1 for the luminosity difference up to $1\% = 10^4$ ppm; and d_2 and d_3 as coefficients for $\Delta A_{Eb,\max}$ and $\Delta A_{Ep,\max}$, respectively. All three terms represent differences between e^+ and e^- running that cannot be determined by existing monitoring methods. Pseudo data are generated in each bin using the expected statistical uncertainty and with the three experimental systematic effects applied. All pseudo-data are fitted using

$$A_{\mathrm{pseudo-data}} = p_0(-108\ \mathrm{ppm})Q^2Y(y)\frac{R_V}{1+\frac{1}{5}R_S} + p_1 + p_2\Delta A_{Eb,\max} + p_3\Delta A_{Ep,\max} \tag{27}$$

where p_0 represents $2C_{3u} - C_{3d}$. The χ^2 is calculated using the uncertainty of the asymmetry (either statistical or total that includes widening from charged particles and pair production background events) in each bin and then minimized.

To understand the impact of each systematic effect, we practiced the generation of the pseudo data and the fitting in stages. First, we excluded the $\Delta A_{E_b,\max}$ and $\Delta A_{E_p,\max}$ terms when generating the pseudo data – setting $d_2 = d_3 = 0$ and subsequently $p_2 = p_3 = 0$ when fitting – and minimize the χ^2 using the statistical uncertainty of the asymmetry in each bin, we obtain:

$$\Delta(2C_{3u} - C_{3d})_{\mathrm{stat+lumi}} = \pm 0.0301\ . \tag{28}$$

If we include charged particles and pair production background events, i.e. use the uncertainty of the asymmetry in each bin calculated from Eqs. (22) and (23), we obtain:

$$\Delta(2C_{3u} - C_{3d})_{\mathrm{stat+bg+lumi}} = \pm 0.0323\ . \tag{29}$$

We further included the uncertainties of Table 1 and those due to the uncertainty in the PDF inputs at this stage. But these effects are found to be sub-1% level on the asymmetry and the differences in the fitted results are negligible.

Next, we took into account the $\Delta A_{E_b,\max}$ term by setting nonzero $d_{0,1,2}$ and fitting $p_{0,1,2}$, we obtain:

$$\Delta(2C_{3u} - C_{3d})_{\mathrm{stat+bg+Eb+lumi}} = \pm 0.0375\ . \tag{30}$$

If we also include the $\Delta A_{E_p,\max}$ term by setting nonzero $d_{0,1,2,3}$ and fitting $p_{0,1,2,3}$, we obtain:

$$\Delta(2C_{3u} - C_{3d})_{\mathrm{exp}} = \pm 0.0650\ , \tag{31}$$

which immediately doubles the uncertainty. This is partly due to the added degree of freedom in the fit and partly due to the competing effects between ΔE_b and ΔE_p, since both affect Q^2 and cause similar shifts to the asymmetry. Clearly, it's desirable to control the magnetic field of SoLID to within 10^{-5} between opposite polarity runs using the method proposed in Appendix C so the fitting parameter p_3 can be omitted.

5.1.2 Monte Carlo Method for Uncertainty Determination

The theoretical uncertainties in principle can be studied by shifting all pseudo data points up or down together by ±1% of the QED NLO contribution or the higher-twist contribution to the asymmetry, then refitting the pseudo data and taking the difference in the fitted values of C_{3q}. However, we found the difference in the fitted C_{3q} varies from one set of generated pseudo data to another, reflecting a combined effect of the statistical nature of the pseudo data and the fitting method. To fully explore the uncertainty of the fitting method described in the previous section, we adopted a Monte Carlo method as follows: we generated 1000 sets of pseudo data using randomly selected luminosity, beam energy, and E_p factor (with the magnitude of the E_p factor below $\pm 10^{-5}$) each time, we fit the pseudo data and obtain $p_{0,1,2}$ (we do not fit the E_p effect, i.e. set $p_3 = 0$ given that it can be controlled to a desired level). Then we shift the pseudo data by ±1% of the QED NLO contribution and refit and record the difference in the fitted C_{3q}, denoted as $dC_{3q,1\%\mathrm{QED}}$. Similarly, we shift the pseudo data by the estimated HT contribution and refit and record the difference in the fitted C_{3q}, called $dC_{3q,\mathrm{HT}}$. From the generated 1000 data sets and fittings we obtained distributions of $dC_{3q,1\%\mathrm{QED}}$ and $dC_{3q,\mathrm{HT}}$. Taking the standard deviation of the distribution as the uncertainty, we found:

$$\Delta(2C_{3u} - C_{3d})_{1\%\ \mathrm{on\ QED}} = \pm 0.009\ , \tag{32}$$

see Fig. 18 (left panel). This is a much smaller effect compared to the relative size of the QED NLO contribution ($2 \sim 5$ times larger than EW contribution). We think the reason that our method is not very sensitive to the 1% QED shift is that this shift is partially compensated by the ΔA_{E_b} term, which has a similar kinematic dependence as the QED NLO term.

For higher twist effects, we shift all pseudo data points up or down together according to the size of the HT effects on $xF_3^{\gamma Z}$ using H_3^ν from [41] and that on F_1^γ from CJ15 [48], we obtain:

$$\Delta(2C_{3u} - C_{3d})_{\mathrm{HT\ using}\ H_3^\nu} = {}^{-0.073}_{-0.164}\ , \tag{33}$$

Alternatively, if we assume HT effects on the asymmetry is the same (relative) size as the CJ15's result on F_2^γ, then

$$\Delta(2C_{3u} - C_{3d})_{\mathrm{HT\ using}\ H_2} = {}^{+0.000}_{-0.035}\ , \tag{34}$$

see Fig. 18 (right panel).

Finally, we note that the MC method gives a wider distribution for the fitted C_{3q} than Eqs. (28-30), indicating it includes uncertainties of both the data being fitted and the fitting method. From Fig. 18, we see that the nominal fits have at the largest

$$\Delta(2C_{3u} - C_{3d})_{\mathrm{stat+bg+Eb+lumi,MC}} = \pm 0.053\ . \tag{35}$$

Because the HT estimate using the H_3^ν approach is larger than the experimental uncertainty of Eq. (35), we expect the data obtained from the proposed measurement will improve the uncertainty on HT of $F_3^{\gamma Z}$ compared to [49], and we will focus on the CJ15 estimate hereafter.

5.1.3 Combined Uncertainties on C_{3q}

Putting together all uncertainty estimate, we obtain from the MC method:

$$\Delta(2C_{3u} - C_{3d})_{\mathrm{total}} \approx \pm 0.053(\mathrm{exp}) \pm 0.009(1\%\ \mathrm{QED})^{+0.000}_{-0.035}(\mathrm{HT, CJ15}) = {}^{+0.054}_{-0.064}\ . \tag{36}$$

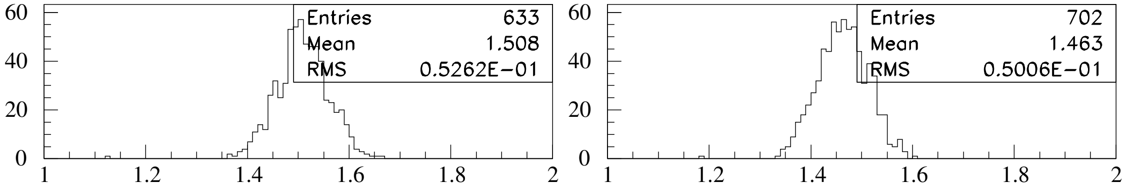

with −1% QED shift

with CJ15 HT upper bound

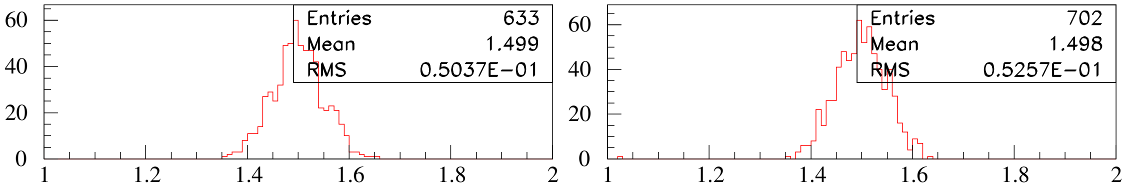

nominal

nominal

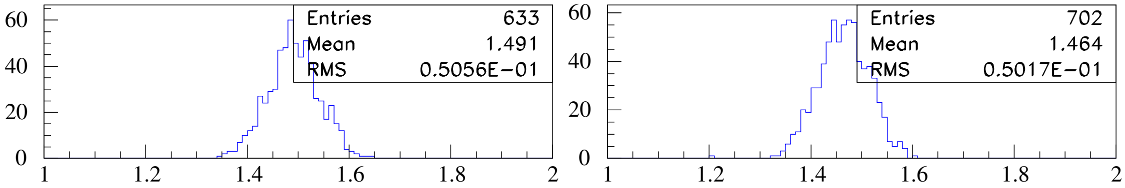

with +1% QED shift

with CJ15 HT lower bound

Figure 18: Distributions of the fitted $2C_{3u} - C_{3d}$ value from the Monte-Carlo fitting method. The fitting was performed 1000 times though not all pseudo data sets yielded successful fit results. *Left:* Nominal value (middle) and with pseudo data shifted by ±1% of the QED NLO contribution (top and bottom). The uncertainty of the pseudo data fitted here included only statistical uncertainty; *Right*: Nominal value (middle) and with pseudo data shifted by the maximum and the minimum of the HT contribution estimated using the CJ15 estimate on H_2^γ (top and bottom) with a 90% C.L. The uncertainty of the pseudo data fitted here included both statistical uncertainty and background effects.

5.1.4 Expected BSM Physics Mass Limit

One can now calculate the mass limit using Eq. (18). Using the ± 0.060 total uncertainty, we obtain:

$$\Lambda_{AA} = v\sqrt{\frac{8\sqrt{5}\pi}{\Delta(2C_{3u} - C_{3d})}} = 246.22 \text{ GeV}\sqrt{\frac{8\sqrt{5}\pi}{0.060}} = 7.5 \text{ TeV} , \qquad (37)$$

at the 68% C.L. This will be the first time we set a mass limit on the AA term of the electron-quark effective couplings.

5.2 Projected Results on $F_3^{\gamma Z}$

The asymmetry $A_d^{e^+e^-}$ provides a direct measurement of the structure function $F_3^{\gamma Z}$, as can be seen from Eq. (13). While a complete analysis from $A_d^{e^+e^-}$ to $F_1^{\gamma Z}$ requires care, we provide here a simple projection of what can be extracted from the proposed measurement.

We start from the statistical uncertainty of $A_d^{e^+e^-}$ that includes background correction, then add in quadrature the experimental uncertainty as listed in Table 1, and uncertainties due to luminosity and beam energy differences using the fitted uncertainties of p_1 and p_2 in Eq. (27), respectively. The uncertainty due to the $\pm 1\%$ uncertainty in QED higher-order corrections contributes to the $F_3^{\gamma Z}$ determination twice: first is when subtracting the QED contribution from the measured asymmetry, second is through its effect on the fitted p_2. Both effects were evaluated and added in quadrature to other sources of the uncertainties listed above. We treat the result as the total uncertainty of $A_d^{e^+e^-}$ and calculate the uncertainty in $F_3^{\gamma Z}$ using Eq. (13). The simple parton model of F_1^{γ}, Eq. (17), is used with MMHT14 PDFs as input. Details of the projected results and uncertainties are shown in Table 2 using standard uncertainty propagation, though a Monte Carlo method similar to section 5.1.2 can be used for a more robust projection. The procedure is repeated for 5% and 10% uncertainties in the QED higher-order corrections, and we found the uncertainties in $xF_{3,d}^{\gamma Z}$ due to QED and dp_2 enlarge proportionally.

Table 2: Expected uncertainty on $xF_{3,d}^{\gamma Z}$ extracted from $A_d^{e^+e^-}$. The uncertainty due to luminosity and beam energy differences are obtained from the fitting results of p_1 and p_2 of Eq. (27) and by varying the QED higher-order contribution by 1% and refitting. The uncertainty due to PDF inputs and those listed in Table 1 are very small and not shown, but are included in the total uncertainty calculation.

x	Q^2 (GeV)^2	Y	$xF_{3,d}^{\gamma Z}$ from $A_d^{e^+e^-}$	$d(xF_{3,d}^{\gamma Z})$					
				(stat)	(stat +bg)	(1% QED)	(lumi dp_1)	(E_b fit dp_2)	(total)
0.25	3.5	0.812	0.8250	0.0970	0.1350	0.0816	0.0735	0.0008	0.1993
0.25	4.5	0.968	0.8144	0.0227	0.0282	0.0657	0.0496	0.0008	0.0901
0.35	4.5	0.751	0.6978	0.0281	0.0307	0.0572	0.0496	0.0009	0.0865
0.35	5.5	0.892	0.6781	0.0079	0.0087	0.0421	0.0329	0.0008	0.0548
0.45	5.5	0.715	0.4722	0.0194	0.0196	0.0291	0.0294	0.0009	0.0498
0.35	6.5	0.980	0.6629	0.0118	0.0138	0.0336	0.0237	0.0006	0.0450
0.45	6.5	0.835	0.4549	0.0047	0.0048	0.0206	0.0191	0.0007	0.0290
0.55	6.5	0.691	0.2586	0.0098	0.0098	0.0107	0.0142	0.0008	0.0226
0.45	7.5	0.928	0.4413	0.0053	0.0056	0.0178	0.0142	0.0005	0.0241
0.55	7.5	0.793	0.2478	0.0035	0.0035	0.0079	0.0094	0.0005	0.0133
0.65	7.5	0.674	0.1113	0.0047	0.0047	0.0021	0.0050	0.0005	0.0085
0.45	8.5	0.986	0.4302	0.0220	0.0235	0.0122	0.0098	0.0004	0.0359
0.55	8.5	0.881	0.2393	0.0033	0.0034	0.0071	0.0072	0.0004	0.0113
0.65	8.5	0.763	0.1064	0.0025	0.0025	0.0021	0.0037	0.0003	0.0056
0.75	8.5	0.662	0.0351	0.0026	0.0027	0.0003	0.0020	0.0002	0.0043
0.55	9.5	0.948	0.2322	0.0073	0.0075	0.0050	0.0050	0.0003	0.0126
0.65	9.5	0.843	0.1024	0.0022	0.0022	0.0021	0.0029	0.0002	0.0047
0.75	9.5	0.740	0.0335	0.0018	0.0018	0.0004	0.0014	0.0002	0.0029
0.65	10.5	0.910	0.0990	0.0041	0.0041	0.0016	0.0021	0.0002	0.0063
0.75	10.5	0.812	0.0321	0.0015	0.0015	0.0004	0.0010	0.0001	0.0023
0.75	11.5	0.876	0.0310	0.0023	0.0023	0.0002	0.0007	0.0001	0.0033

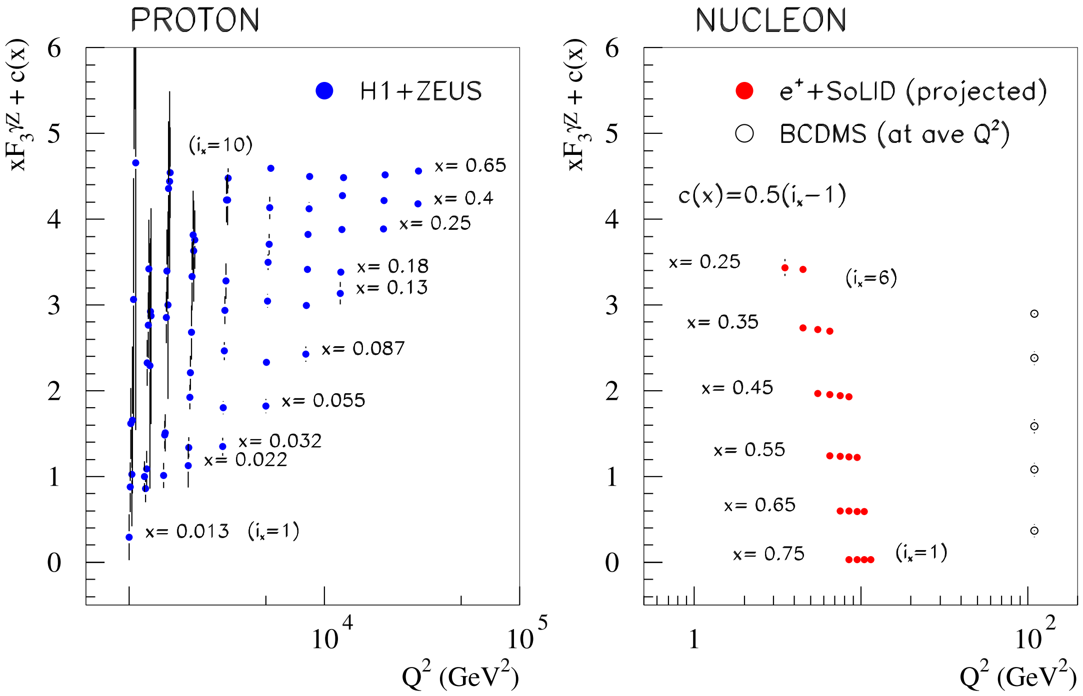

Figure 19: Projected results on the per-nucleon $F_{3,d}^{\gamma Z}$ from the proposed measurement (red solid points). For visual clarity, all data points are offset vertically by $c(x) = 0.5(i_x - 1)$ with $i_x = 1, 2, \ldots 10$ and $i_x = 1, 2, \ldots 6$ from bottom to top for the proton (left) and the nucleon (right), respectively. See text for the simple method used to make these projections and details of existing data and discussions, and Table 2 for numerical values.

We plot the projected $F_3^{\gamma Z}$ (for 1% QED higher-order calculation uncertainty) in their per-nucleon value in the right panel of Fig. 19 along with existing data from HERA [51] (left panel, proton) and BCDMS [52] (right panel, nucleon). The existing data are the same as in Fig. 18.12 of PDG [10] but the HERA data plotted there were combined across their Q^2 ranges. The BCDMS data published were for a Q^2 range from 80 to 140 (GeV)^2 and are plotted here at 110 (GeV)^2. The x values of BCDMS cover from $x = 0.25$ to $x = 0.65$ with 0.10 step size and are thus the same as SoLID projected results. The Q^2 "gap" in the right panel is likely to be filled at the future EIC if a positron beam becomes available there. Likewise, one can repeat the measurement proposed here on the proton with SoLID or EIC to fully map out the left panel.

5.3 Connection to TPE Study

The measurement proposed here is part of JLab positron working group [20] (e^+@JLab) research program. The e^+@JLab program in fact is devoting several measurements towards a better understanding of the two photon exchange (TPE) process with the hope of casting more light on the proton form factor ratio G_E^p/G_M^p discrepancy observed between polarization transfer and Rosenbluth separation methods. Measurement of the difference between unpolarized e^+ and unpolarized e^- elastic scattering off a proton target provides direct access to TPE in elastic scattering. The most comprehensive measurement can be performed with the CLAS12 detector [53]. The CLAS12 measurement can be complemented by a Hall A [54] measurement using the Super BigBite Spectrometer with a focus on low-ϵ kinematics. The spectrometers in Hall C would be well-suited for performing a so-called super-Rosenbluth measurement with positrons [55], in which an L/T separation is performed from cross sections in which only the recoiling proton is detected. The results of a positron super-Rosenbluth measurement could be directly compared to those of a previous measurement in Hall A, taken with electrons [56]. Once such dedicated data are collected and analyzed, the information they provide on TPE in elastic scattering will help to improve TPE calculations in the DIS region at low Q^2 as well. As a result, the uncertainty of TPE calculations for the Q^2 region of the measurement proposed here ($Q^2 > 6$ GeV^2, where the statistical precision is highest) can be better constrained. Meanwhile, we point out that the proposed measurement will provide the highest precision data to date, which can be directly used to cross check TPE calculations in the DIS region[4].

6 Beam Time Request and Scheduling Considerations

6.1 Beam Time Request

We request 104 days of beam time. This includes 96 days of 3 μA running split evenly between e^+ and e^- runs – 80 days DIS production at 11 GeV, 8 days of reverse polarity runs at 11 GeV, and 8 days of DIS at 6.6 GeV for checking inputs to radiative corrections (bin migration); 2 days for beam pass changes; 2 days for reversing SoLID polarity during each of e^+ and e^- runs, a maximum of 2 days for Compton tune, and 2 days of commissioning. While beam polarization is not critical for the measurement, we note that parity feedback for helicity-correlated beam quality control is the norm for JLab experiments and we plan to utilize it through out the run. A summary of beam time request is given in Table 3.

Not included in the beam time request is the time needed to commission the positron beam, and the time needed to switch from e^- to e^+ beam and the setup that follows, which may be substantial.

6.2 Scheduling Considerations

The proposed measurement is designed to be done with the same configuration as the SoLID PVDIS experiment, with the only change being the SoLID magnet polarity reversal. Thus it can run either before or after PVDIS, or run interchangeably. We note that many of the systematic effects, such as tracking efficiency and accuracy, DAQ deadtime, and Q^2 determination will be studied extensively for the PVDIS experiment, which will run at 17 times higher current than the proposed measurement. Considering the sequence of e^- vs. e^+ runs, frequent switching between e^- and e^+ runs is highly desired, though probably very difficult to achieve in practice.

---

[4] Higher order QED contributions were taken into account in HERA analysis of e^+p and e^-p DIS data, though a global fit was used to separate all effects and thus the constraint on TPE is not as direct as the proposed measurement.

Table 3: Beam time request for the proposed measurement. The target type "carbon" refers to carbon foils for optics and beam checkout, and "LD_2" refers to the 40-cm liquid deuterium target. Time needed to commission the PEPPo source, the positron beam and the secondary electron beam, and the time needed to switch between the two beams are not included.

Purpose	Beam energy and type, target	PAC days
General Commissioning	as needed, carbon	2
Compton tune	as needed, carbon	2
Production	11 GeV, 3 μA e^+ and e^- (PEPPo), LD_2	80
Reverse polarity runs	11 GeV 3 μA e^+ and e^- (PEPPo), LD_2	8
Reverse SoLID polarity	N/A	2
Radiative (bin migration) corrections	6.6 GeV 3 μA e^+ and e^- (PEPPo), LD_2	8
Pass changes	N/A	2
Total		104

7 Summary

We propose an exploratory measurement of the lepton charge asymmetry on the deuteron, $A_d^{e^+e^-}$. The measured asymmetry will provide a unique access to the third (AA) lepton-quark effective coupling combination $2C_{3u} - C_{3d}$. We attempt to perform a first extraction of this combination for the electron, and we estimate the uncertainty to be

$$\Delta(2C_{3u} - C_{3d})_{\text{total}} \approx \pm 0.055(\text{exp}) \pm 0.009(1\% \text{ QED})^{+0.000}_{-0.035}(\text{HT using CJ15 H}_2)\ . \quad (38)$$

using the CJ15 estimate on the HT effects. This estimate is based on the expectation that QED and QCD higher order corrections can be calculated to 1% relative or better. We note that the extensive TPE study planned for elastic ep scattering using a e^+ beam will help to constrain TPE calculations needed for DIS. We also expect that with more theoretical effort, the uncertainty due to higher-twist effects will likely be reduced with a dedicated study in the near future. Both higher-order radiative corrections and HT uncertainties will require support from and close collaboration with the theory groups, and some work is already underway. In the meantime, one can extract the nucleon structure function $F_{3,d}^{\gamma Z}$ and improve upon existing world data (which are so far provided only by the BCDMS collaboration for the nuclear target), as shown in Fig. 19. While it is not within the scope of the proposed measurement, many of the practices in this work may benefit other SoLID experiments as well as similar studies at the future EIC. Finally, we note that further intensive work will be needed to carry out the proposed measurements and to analyze and interpret the data, yet we have established a clear roadmap to completing the experiment and, we hope, opened a new direction for the research program at JLab.

Acknowledgment

by X. Z.

I thank my father for showing me how to be a professor and a life-time researcher, and my mother for endowing me with her passion for new things and a desire to "do it all". I thank people who support me, in person or at a distance, for forming an invisible yet tightly knitted web that holds my world together in these difficult times. And I thank those who provide vision and guidance in this endless chase of adventure in physics.

This work is supported by U.S. Department of Energy under Award numbers SC00–03885 and DE–SC0014434.

A Lepton DIS asymmetries from γZ interferences

In this section we present expressions for lepton DIS asymmetries that arise from the γZ interference, including PVDIS asymmetry and lepton charge asymmetries for both the proton and the deuteron.

A.1 PVDIS Asymmetry In the Parton Model

We start from the parton model expressions. Details of the derivation will be given in Appendix D so as not to bore the readers. The PVDIS asymmetry for a proton target, counting u, d, c, s quark flavors and using $C_{1c,2c} = C_{1u,2u}$, $C_{1s,2s} = C_{1d,2d}$, is:

$$\begin{aligned} & A_{RL,p}^{e^-,\mathrm{PVDIS}} \\ = \quad & |\lambda| \frac{3\sqrt{2} G_F Q^2}{4\pi\alpha} \frac{[2(u^+ + c^+)C_{1u} - (d^+ + s^+)C_{1d}] + Y[2(u_V + c_V)C_{2u} - (d_V + s_V)C_{2d}]}{4[u^+ + c^+] + [d^+ + s^+]} \end{aligned} \tag{39}$$

where the $-$ sign in σ^- represents electron scattering, $|\lambda|$ is the magnitude of the incident beam's polarization and the parton distributions are $q^+ \equiv q(x) + \bar{q}(x)$ and $q_V \equiv q(x) - \bar{q}(x)$ ($q = u, d, c, s$). The kinematic function Y is defined as

$$Y(y) \equiv \frac{1 - (1-y)^2}{1 + (1-y)^2} \, . \tag{40}$$

For the deuteron or any isoscalar target and ignoring nuclear effects,

$$\begin{aligned} & A_{RL,d}^{e^-,\mathrm{PVDIS}} \\ = \quad & |\lambda| \frac{3 G_F Q^2}{2\sqrt{2}\pi\alpha} \frac{2(1 + R_C)C_{1u} - (1 + R_S)C_{1d} + Y[2C_{2u}(1 + \epsilon_c) - C_{2d}(1 + \epsilon_s)]R_V}{5 + 4R_C + R_S} \end{aligned} \tag{41}$$

where

$$R_V(x) \quad \equiv \quad \frac{u_V + d_V}{u^+ + d^+} \, , \quad R_C(x) \equiv \frac{2(c + \bar{c})}{u^+ + d^+} \, , \quad R_S(x) \equiv \frac{2(s + \bar{s})}{u^+ + d^+} \, , \tag{42}$$

and the ϵ's account for $c - \bar{c}$ and $s - \bar{s}$ which are often set to zero in PDF sets:

$$\epsilon_c \quad \equiv \quad \frac{2(c - \bar{c})}{u^+ + d^+} \, , \quad \epsilon_s \equiv \frac{2(s - \bar{s})}{u^+ + d^+} \, . \tag{43}$$

If counting only the light quarks u and d then

$$A_{RL,d}^{e^-,\mathrm{PVDIS}} \quad \approx \quad |\lambda| \frac{3 G_F Q^2}{10\sqrt{2}\pi\alpha} \left[(2C_{1u} - C_{1d}) + R_V Y (2C_{2u} - C_{2d})\right] \, . \tag{44}$$

A.2 Lepton vs. Anti-Lepton Asymmetries In the Parton Model

The asymmetry between right-handed e^+ and left-handed e^- DIS off a proton target, assuming $c = \bar{c}$ and $s = \bar{s}$ [5], is

$$\begin{aligned} A^{e^+e^-}_{RL,p} &\equiv \frac{\sigma^+_R - \sigma^-_L}{\sigma^+_R + \sigma^-_L} \\ &= \frac{3G_FQ^2}{2\sqrt{2}\pi\alpha} Y(y) \frac{2|\lambda| u_V C_{2u} - |\lambda| d_V C_{2d} - 2u_V C_{3u} + d_V C_{3d}}{4(u^+ + c^+) + 1(d^+ + s^+)} \ . \end{aligned} \tag{45}$$

Similarly, the asymmetry between right-handed e^+ and right-handed e^- DIS off a proton target under the same assumption is:

$$\begin{aligned} A^{e^+e^-}_{RR,p} &\equiv \frac{\sigma^+_R - \sigma^-_R}{\sigma^+_R + \sigma^-_R} \\ &= \frac{3G_FQ^2}{2\sqrt{2}\pi\alpha} \frac{-2|\lambda|(u^+ + c^+)C_{1u} + |\lambda|(d^+ + s^+)C_{1d} - 2u_V C_{3u} Y(y) + d_V C_{3d} Y(y)}{4(u^+ + c^+) + (d^+ + s^+)} \ . \end{aligned} \tag{46}$$

For the deuteron or any isoscalar target and ignoring nuclear effects:

$$A^{e^+e^-}_{RL,d} = \frac{3G_FQ^2}{2\sqrt{2}\pi\alpha} Y(y) R_V \frac{|\lambda|(2C_{2u} - C_{2d}) - (2C_{3u} - C_{3d})}{5 + 4R_C + R_S} \ , \tag{47}$$

$$A^{e^+e^-}_{RR,d} = \frac{3G_FQ^2}{2\sqrt{2}\pi\alpha} \frac{-|\lambda|[2(1 + R_C)C_{1u} - (1 + R_S)C_{1d}] - Y(y) R_V (2C_{3u} - C_{3d})}{5 + 4R_C + R_S} \ . \tag{48}$$

And if only u, d are considered then

$$A^{e^+e^-}_{RL,d} \approx \frac{3G_FQ^2}{10\sqrt{2}\pi\alpha} Y(y) R_V \left[|\lambda|(2C_{2u} - C_{2d}) - (2C_{3u} - C_{3d})\right] \quad (u, d \ \text{only}), \tag{49}$$

$$A^{e^+e^-}_{RR,d} \approx \frac{3G_FQ^2}{10\sqrt{2}\pi\alpha} \left[-|\lambda|(2C_{1u} - C_{1d}) - Y(y) R_V (2C_{3u} - C_{3d})\right] \quad (u, d \ \text{only}). \tag{50}$$

The equations for RL and RR asymmetries can be extended to LR, and LL, respectively, by flipping $|\lambda| \to -|\lambda|$. And all can be used for $A^{e^+e^-}$ (unpolarized beams) by setting $|\lambda| = 0$.

The asymmetry measured at CERN [18] is $B_+ \equiv \frac{\sigma^+(-|\lambda|) - \sigma^-(+|\lambda|)}{\sigma^+(-|\lambda|) + \sigma^-(+|\lambda|)}$ on a ^{12}C target and thus can be treated as $A^{\mu^+\mu^-}_{LR,d}$. Substituting $|\lambda| \to -|\lambda|$ in Eq. (47):

$$B = -\frac{3G_FQ^2}{2\sqrt{2}\pi\alpha} Y(y) R_V(x) \frac{(2C_{3u} - C_{3d}) + |\lambda|(2C_{2u} - C_{2d})}{5 + 4R_C + R_S} \ . \tag{51}$$

---

[5] if considering $c \neq \bar{c}$ and $s \neq \bar{s}$, change $u_V \to u_V + c_V$ and $d_V \to d_V + s_V$ in all proton results, and multiply $C_{2u(d)}$ and $C_{3u(d)}$ by $(1 + \epsilon_c)$ $((1 + \epsilon_s))$ – see Eq. (103) – in all deuteron results throughout this section. No change to the C_{1q} term if calculating $A^{e^+e^-}_{LL,RR}$.

For SoLID we can use unpolarized beam (higher intensity) and measure

$$A_d^{e^+e^-} = -\frac{3G_F Q^2}{2\sqrt{2}\pi\alpha} Y(y) R_V \frac{(2C_{3u} - C_{3d})}{5 + 4R_C + R_S} \tag{52}$$

$$\approx -\frac{3G_F Q^2}{10\sqrt{2}\pi\alpha} Y(y) R_V (2C_{3u} - C_{3d}) \ \ (u, d \ \text{ only})\ . \tag{53}$$

A.3 PVDIS Asymmetry in the General Case

After establishing the parton-model results for asymmetries, we now consider the more general case. The general tensor expression for the NC lepton scattering cross section is [57]:

$$\frac{d^2\sigma}{d\Omega dE'} = \frac{\alpha^2}{Q^4}\left(\frac{E'}{E}\right)\left(L^{\gamma}_{\mu\nu} W^{\mu\nu}_{\gamma} + \eta_{\gamma Z} L^{\gamma Z}_{\mu\nu} W^{\mu\nu}_{\gamma Z}\right)\ , \tag{54}$$

where

$$\eta_{\gamma Z} = \frac{G_F Q^2}{2\sqrt{2}\pi\alpha} \frac{M_Z^2}{M_Z^2 + Q^2}\ . \tag{55}$$

We use the leptonic and hadronic tensors from [57], with the exception of adding a minus sign (in red below) to the γZ leptonic tensor:

$$L^{\gamma Z}_{\mu\nu} \ \text{ for } e^{\pm} = -(g_V^e \pm g_A^e \lambda) L^{\gamma}_{\mu\nu}\ , \tag{56}$$

where $\lambda = \pm 1$ is the helicity state of the initial lepton. The added minus sign represents the charge of the lepton (e^-, μ^- or τ^-) in unit of $|e|$, and is missing in Ref. [57] and Eq. (18.3) of PDG [10]. The helicity-dependent differential cross section difference is

$$\frac{d^2\sigma_R}{d\Omega dE'} - \frac{d^2\sigma_L}{d\Omega dE'} = \frac{\alpha^2}{Q^4}\left(\frac{E'}{E}\right)\left(\frac{G_F Q^2}{2\sqrt{2}\pi\alpha}\right)|\lambda| \times \left\{ g_A^e \frac{Q^2}{M} F_1^{\gamma Z} + g_A^e\left(\frac{Q^2}{My} - Mx\right) F_2^{\gamma Z} + g_V^e \frac{Q^2(2-y)}{2My} F_3^{\gamma Z}\right\} , \tag{57}$$

and the sum is

$$\frac{d^2\sigma_R}{d\Omega dE'} + \frac{d^2\sigma_L}{d\Omega dE'} = \frac{\alpha^2}{Q^4}\left(\frac{E'}{E}\right) \times \left\{ \frac{Q^2}{M} F_1^{\gamma} + \left(\frac{Q^2}{My} - Mx\right) F_2^{\gamma} - \left(\frac{G_F Q^2}{2\sqrt{2}\pi\alpha}\right)\left[g_V^e \frac{Q^2}{M} F_1^{\gamma Z} + g_V^e \left(\frac{Q^2}{Mx}\frac{1-y}{y} - Mx\right) F_2^{\gamma Z} + g_A^e \frac{Q^2}{2My}(2-y) F_3^{\gamma Z} |\lambda|^2 \right]\right\}\ , \tag{58}$$

where one can set $|\lambda|^2 = 1$ since so far we are dealing with incident leptons of pure helicity states $\lambda = \pm 1$. To calculate the experimental asymmetry, one denotes $N_R(N_L) = (1 - P_b)(N_{h=+1} + N_{h=-1}) + P_b N_{h=+1(-1)}$ for the number of beam particles incident on the target during helicity $+1(-1)$ time windows with P_b the magnitude of the beam polarization, it's straightforward to show one can replace $|\lambda|$ by $|P_b|$ and the experimental PVDIS asymmetry in terms of structure functions is:

$$A_{RL}^{e^-} = \frac{|P_b|\eta_{\gamma Z}\left[g_A^e 2yF_1^{\gamma Z} + g_A^e F_2^{\gamma Z}\left(\frac{2}{xy}-\frac{2}{x}-\frac{2M^2xy}{Q^2}\right) + g_V^e(2-y)F_3^{\gamma Z}\right]}{2yF_1^{\gamma} + \left(\frac{2}{xy}-\frac{2}{x}-\frac{2M^2xy}{Q^2}\right)F_2^{\gamma} - \eta_{\gamma Z}\left[g_V^e 2yF_1^{\gamma Z} + g_V^e\left(\frac{2}{xy}-\frac{2}{x}-\frac{2M^2xy}{Q^2}\right)F_2^{\gamma Z} + g_A^e(2-y)F_3^{\gamma Z}\right]} . \tag{59}$$

This result can be used for both collider and fixed target settings. For positron scattering, one replaces $g_A^e \to -g_A^e$. These results were also presented in Ref. [58] and [59] with $\frac{M^2x}{Q^2} = \frac{M}{E}$ for fixed target settings, though they used a different convention for $g_{V,A}^e$ and g_V^q, and have a sign problem due to using $L_{\mu\nu}^{\gamma Z}$ from [57]. Equations (61) shows that the $F_3^{\gamma Z}(x, Q^2)$ term involves a spin flip of the quark (g_A^q) and is suppressed by the kinematic factor Y_3 due to angular momentum conservation. It vanishes at the forward angle $\theta = 0$ or $y = 0$, and increases with θ or y at fixed x.

One should note the process of replacing $|\lambda|$ by $|P_b|$ works for all asymmetries derived in this document and thus we will use $|\lambda|$ for the magnitude of both helicity and beam polarization, though there is a difference as outlined above.

Approximations

In the results above we have kept the electroweak contribution to the total cross section in the denominator, though they can be safely omitted at low to medium energies much below the Z-pole. Furthermore, we can use $R^{\gamma(\gamma Z)}(x, Q^2)$, the ratio of the longitudinal to transverse virtual photon electromagnetic absorption (γZ interference) cross sections to eliminate F_2:

$$F_2^{\gamma(\gamma Z)} = \frac{2xF_1^{\gamma(\gamma Z)}(1+R^{\gamma(\gamma Z)})}{r^2} , \tag{60}$$

with $r^2 = 1 + \frac{Q^2}{\nu^2}$. The asymmetry can now be written as:

$$A_{PV} = \frac{G_F Q^2}{2\sqrt{2}\pi\alpha}\left[g_A^e \frac{F_1^{\gamma Z}}{F_1^{\gamma}} Y_1 + \frac{g_V^e}{2}\frac{F_3^{\gamma Z}}{F_1^{\gamma}} Y_3\right] , \tag{61}$$

where the kinematic factors $Y_{1,3}$ are

$$Y_1 = \left[\frac{1+R^{\gamma Z}}{1+R^{\gamma}}\right] \frac{1+(1-y)^2 - y^2\left[1-\frac{r^2}{1+R^{\gamma Z}}\right] - \frac{2M^2x^2y}{Q^2}}{1+(1-y)^2 - y^2\left[1-\frac{r^2}{1+R^{\gamma}}\right] - \frac{2M^2x^2y}{Q^2}} \tag{62}$$

$$Y_3 = \left[\frac{r^2}{1+R^{\gamma}}\right] \frac{1-(1-y)^2}{1+(1-y)^2 - y^2\left[1-\frac{r^2}{1+R^{\gamma}}\right] - \frac{2M^2x^2y}{Q^2}} . \tag{63}$$

Our results for $Y_{1,3}$ are consistent with the fixed-target results in Ref. [58] and [59]. To a good approximation $R^{\gamma Z}$ can be assumed to be equal to R^{γ}, resulting in $Y_1 = 1$.

A.4 Lepton-Charge Asymmetries in the General Case

The above prescription can be extended to e^+e^- asymmetries. We found similar results:

$$A_{RL}^{e^+e^-} = \frac{\eta_{\gamma Z}\left(|\lambda| g_V^e + g_A^e\right)(2-y)F_3^{\gamma Z}}{2yF_1^\gamma + \left(\frac{2}{xy} - \frac{2}{x} - \frac{2M^2xy}{Q^2}\right)F_2^\gamma - \eta_{\gamma Z}(g_V^e + g_A^e)\left[2yF_1^{\gamma Z} + \left(\frac{2}{xy} - \frac{2}{x} - \frac{2M^2xy}{Q^2}\right)F_2^{\gamma Z}\right]} \tag{64}$$

$$A_{RR}^{e^+e^-} = \frac{\eta_{\gamma Z} g_A^e\left[-|\lambda|(2y)F_1^{\gamma Z} - |\lambda|\left(\frac{2}{xy} - \frac{2}{x} - \frac{2M^2xy}{Q^2}\right)F_2^{\gamma Z} + (2-y)F_3^{\gamma Z}\right]}{2yF_1^\gamma + \left(\frac{2}{xy} - \frac{2}{x} - \frac{2M^2xy}{Q^2}\right)F_2^\gamma - \eta_{\gamma Z} g_V^e\left[2yF_1^{\gamma Z} + \left(\frac{2}{xy} - \frac{2}{x} - \frac{2M^2xy}{Q^2}\right)F_2^{\gamma Z} + (2-y)F_3^{\gamma Z}\right]}. \tag{65}$$

Approximations
Expressing F_2 in terms of R and F_1 and omitting the EW term in the denominator:

$$A_{RL}^{e^+e^-} = \frac{G_F Q^2}{2\sqrt{2}\pi\alpha}\frac{|\lambda| g_V^e + g_A^e}{2} Y_3 \frac{F_3^{\gamma Z}}{F_1^\gamma}\,, \tag{66}$$

$$A_{RR}^{e^+e^-} = \frac{G_F Q^2}{2\sqrt{2}\pi\alpha}\left[-|\lambda| g_A^e Y_1 \frac{F_1^{\gamma Z}}{F_1^\gamma} + \frac{g_A^e}{2} Y_3 \frac{F_3^{\gamma Z}}{F_1^\gamma}\right]\,. \tag{67}$$

Plugging in parton model F_1 for the deuteron, we recover the parton-model result with the only change being $Y \to Y_3$ and the C_{1q} terms need to be multiplied by Y_1:

$$A_{RL,d}^{e^+e^-} = \frac{3G_F Q^2}{2\sqrt{2}\pi\alpha} Y_3 R_V \frac{|\lambda|(2C_{2u} - C_{2d}) - (2C_{3u} - C_{3d})}{5 + 4R_C + R_S}\,, \tag{68}$$

$$A_{RR,d}^{e^+e^-} = \frac{3G_F Q^2}{2\sqrt{2}\pi\alpha} \frac{-|\lambda| Y_1 (2C_{1u} - C_{1d}) - Y_3 R_V (2C_{3u} - C_{3d})}{5 + 4R_C + R_S}\,, \tag{69}$$

For unpolarized beams:

$$A_d^{e^+e^-} = -\frac{3G_F Q^2}{2\sqrt{2}\pi\alpha} Y_3 R_V \frac{(2C_{3u} - C_{3d})}{5 + 4R_C + R_S}\,. \tag{70}$$

B Positron beams at Jefferson Lab

This appendix is based on current investigations of the impact of positron beam operation at CEBAF, that were collected in the document *Some practical considerations for a positron source and positron beam operations at CEBAF* from P. Degtiarenko, J. Grames, J. Kowal, J. Musson, S. Philip, M. Tiefenbak, and K. Welch [60].

B.1 Radiological considerations

Two potential approaches of producing positron beams are considered: one being a separate new enclosure, the other being the existing injector segment to house the positron source. At the very high level, the first option would be the *safest* from a radiological standpoint, as it would allow shielding to be applied as part of the initial facility design, and allow the shielding and other radiological controls to be optimized as integral part of the design.

At energies above the photo-neutron production threshold ($\sim$10-15 MeV), any design will have to address the shielding of neutrons and photons, plus the activation of materials. A 100 kW-100 MeV system would involve significant shielding, and very high levels of activation in the targets and surrounding materials, plus significant activation of cooling water used in and around the targets, and air activation in the vault. Maintenance would also become a significant issue. The activation would produce a radiological *footprint* similar to one of the beam dumps in Hall A or C. In other words, the positron production facility would in effect create a new *radiological facility* analogous to the Hall A dump, including cooling water systems, and would benefit the most from being separated from the existing beam enclosure.

B.2 Beam power considerations

Considering a positron source based on a 100 kW electron beam power, a reasonable way to produce and capture positrons should be a two-stage design. This would allow to separate the functions of main energy dissipation, and the positron production. The first stage (a radiator and a subsequent beam dump) would absorb the main beam energy, and the positron production stage would see only a few percent of it. This separation would further provide more comfortable heat and radiation conditions for the positron capture hardware. The design choices may also include magnetic field removal of the electron beam, as in the current version of the Compact Photon Source [61].

B.3 Personnel and machine protection

From the Personnel Safety System (PSS) perspective, electrical hazard, PSS and ODH controls are hereafter considered:

Electrical hazard - concerning the polarity reversal of the dipoles transporting the beam to experimental halls, the current transducers providing feedback to BELLs system would need to be replaced if installed after the polarity switch;

PSS controls - building a separate positron injector will require to treat it as a separate segment, where all necessary PSS controls would have to be installed, in essence a duplication of the existing injector;

ODH controls - building a separate segment with equipment using significant quantity of cryogens may require installation of an Oxygen Defiency Hazard system.
From the Machine Protection System perspective, there would be in general no need to alter the existing equipment around the site, except the new positron injector area.

B.4 Reversal of CEBAF magnetic field

A tentative list of the electrical systems requiring attention for positron beam delivery is:

1. Trims magnet (∼1900 units);
2. ARC1 to ARC10 (10 units);
3. RSEP8 and RSEP9 (2 units), recirculating septa in the West and East ARC;
4. Dogleg1 to Dogleg9 (9 units);
5. XSEP2, 4, 6, 8, 10 (5 units) extraction region magnets for each of 5 passes;
6. YA 2, 4, 6, 8, 10 (5 units) extraction region thin septa for each of 5 passes;
7. Hall A, B, C, D (5 units) magnets that transport beam into each Hall;
8. BSY Dump (1 unit) which allows beam steered into the dump before Halls A, B, C;
9. Hall A and Hall C Lambertson (2 units);
10. Recirculation and transport shunt modules (109 units);
11. End station A Møller quadrupoles (4 units);
12. End station A Møller and Compton dipoles (2 units);
13. End station C quadrupole magnets (2 units);
14. End station C Compton dipole (1 unit);
15. End station D Tagger magnte (1 unit).

All correctors and quadrupole magnets (except one in Hall C) are bipolar power supplies able to drive positive or negative current, and can be used for electron or positron beams without any changes in hardware. Other trim magnets used for position modulation and fast feedback are not expected to be affected by the beam charge. All of the bending dipole magnets in CEBAF proper are powered by uni-polar power supplies without polarity reversal switches. Most of the ARC magnets are in a series configuration, meaning that the reversal of the power leads at the supply effectively reverses the field in all of the magnets powered by the individual power supply (see Fig. 20 for a typical example). Similarly to the power supplies, the shunt modules will also need to have leads reversed on the termination in the upstairs chassis. To reduce the number of reversing operations and to prevent failures/errors, the polarity reversal would have to be an engineered solution. The system would have remotely controlled switches that can be configured into the correct state for electron or positron beam. Operational procedures would

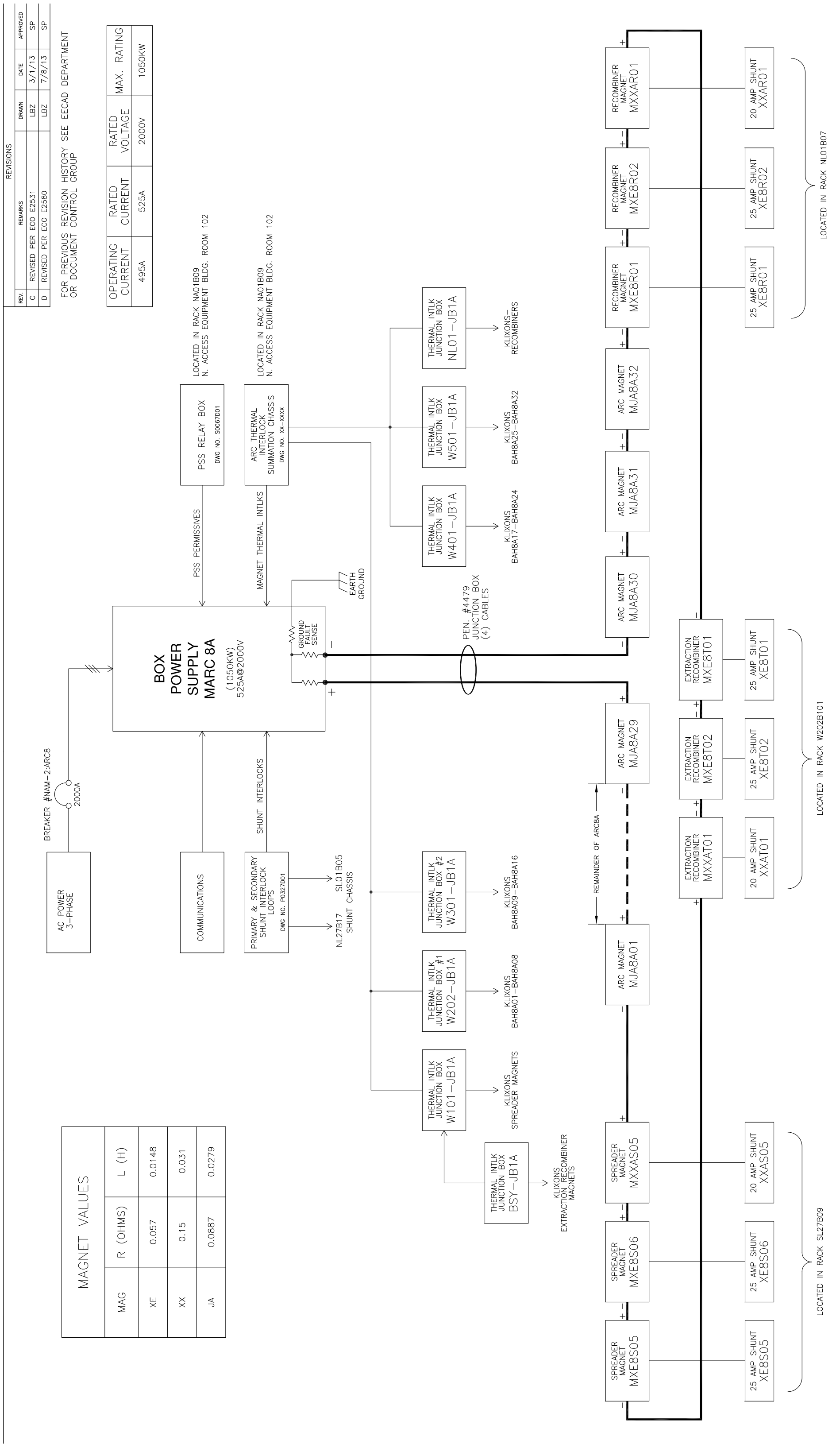

Figure 20: Typical box power supply for ARC magnets.

remain unchanged, as the magnet systems are blind to polarity of connection. However, any portion of the accelerator used to create the electron beam for the production of positrons as well as to transport positrons would require special attention procedurally.
Each of the physics halls have normal and superconducting magnets of various kinds that are not controlled by DC power. Their configuration needs should be examined by the various Halls. Additionally, Hall D is using a permanent dipole to prevent beam into the Hall in case of failure of the Tagger magnet. This may need to be rotated to get the same effect.

The various magnets of the accelerator are a mix of bipolar and unipolar configurations. For the bipolar magnets, observations of the relationship between the $\vec{B} \cdot \vec{dl}$ and the current are consistent with no change in magnetic field versus current after unipolar operation. The meter-scale dipole magnets configured as unipolar systems exhibit a remnant field in the 10-15 Gauss range. The most stringent empirical test of the non-influence of this field is the observation of the fine reproducibility of the beam trajectory after dipole string power supply trips to zero current. The uncontrolled magnetic field of the dipoles, involving prospectively a flux reversal as the dipole field collapses, has not been seen to alter the beam trajectory after the multiple hysteresis cycles executed by protocol after such an event. The known observations seem to indicate that the magnet iron is magnetically soft enough at the fields in use in the CEBAF accelerator as to result in no persistent calibration shifts after field reversal and restoration.

B.5 CEBAF diagnostics for positron beams

Since previous positron efforts [62, 63] have successfully employed DCT, cavity, and button-electrode-based BPM systems, it is our opinion that design for positron production can proceed, based on data obtained from the JLab experience. Following is a summary of diagnostics behavior and metrics.

BCM resolution analysis

Since electrons and positrons differ only by charge (and magnetic moment), polarity is an obvious difference in the electronic signals. Signal polarity is of little significance, since beam current is the result of a magnitude-only measurement of the cavity ($Q \approx 10^4$), which is phase-independent. Also, positron mass and beam size should result in identical beam loading, thereby producing the same cavity response for a given beam current.

For 25 years, JLab has been operating 33 BCM pillbox cavities to provide detailed current information, time of flight measurements, and also as time-of-arrival sensors. Parametric simulation for various expected beam currents has been performed, which agrees with actual beam-based measurements (to within 2 dB). Therefore, it is useful to rely on several rules of thumb for which receiver electronics can be evaluated in the lab. Using this data, the RF output power is accurately predicted for a large range of beam currents. Figure 21 is a composite of several JLab beamline elements, of which the BCM cavity is shown in red. Knowing the sensor output allows one to quickly establish a linearity constant for I_{beam} versus V_{out}, wich in the case of the standard SS304 JLab BCM cavity is $K = 447 \times 10^{-6}$ μA/μV, for electron and presumably positron beams. For determination of resolution, noise power must be known so as to establish the confidence of the measurement from the resulting signal-to-noise ratio (SNR). If a perfect system is assumed and sitting in-situ at room temperature (290 K), the noise power for the 50 Ω

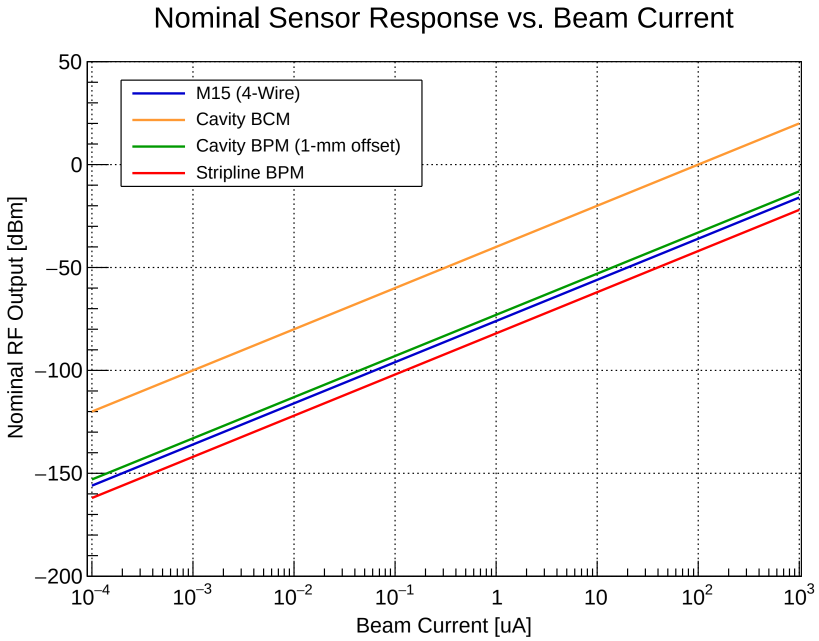

Figure 21: Nomograph of expected BCM cavity power output (red) for various electron/positron beam currents. Recalling that I_{beam}=1 μA results in -40 dBm of output power, then scaling simply follows $20\log(I_{beam})$.

receiver possessing a 1 Hz bandwidth is calculated from

$$P_n = k_B T B = -174\,\text{dBm-Hz} \tag{71}$$

where k_B is the Boltzmann's constant, T=290 K, and B is the bandwidth. Finally, the resolution of the BCM is

$$\sigma = \delta I_{beam} = \frac{\delta V_{noise}}{K} \approx 1\,\text{pA}\,. \tag{72}$$

In reality, cable losses, receiver noise figure, finite-bit resolution and the fact that the receivers are intentionally wound for the larger signals of CEBAF impact the ultimate sensitivity. Extensive JLab experience predicts a minimum detectable signal of $\leq$ 500 pA implying a composite noise figure of 27 dB. A large improvement is expected with the JLab digital diagnostics receivers which possess a 4 dB noise figure.

BPM analysis

Low-Q BPM sensors are somewhat problematic, since they often rely on a directional characteristic. The M15 BPMs at CEBAF are open-wire, 200 Ω structures which, when used with the standard 50 Ω receiver, have moderate directivity, but are not fully reliant on that quality. It was shown [64] that regardless of how the BPM is installed, usable signal is available. With respect to electronics, BPM detection is a relative measurement (aside from any 4-wire applications). Therefore, as long as the change in response is common to all four sensor electrodes (antennas), then a calculated position should be available. It is likely that for any units which have had field mapping and bench calibrations, the relationship between electrical and physical centers would be altered. Reversing the necessary BPM sensors within the beamline is an obvious solution if it appears that sensitivity or orthogonality is compromised.

Assuming nearly-identical behavior for electron and positron beams, the BPM resolution follows as before by establishing a sensor output, calculating expected noise voltage (V_n), and applying to the position calculation algorithm. Here, however, the algorithm may have several forms, which affects the sensitivity a given SNR has on the result. For one-dimension, the resolution is:

$$\sigma_X = \frac{a}{2\sqrt{2}} \frac{1}{\sqrt{SNR}} = \frac{a}{2\sqrt{2}} \frac{V_n}{V_s} \tag{73}$$

where V_s is the signal voltage. Considering the JLab M15 BPM, the typical output power for 100 nA is -102 dBm. Expected noise power for a receiver having a 10 dB noise figure and 10 Hz bandwidth is -154 dBm. So, the resulting 52 dB SNR predicts a resolution of 10 μm. Note that the resolution scales inversely with current, and as the square-root of bandwidth. So, at 10 nA, 1 Hz, the expected resolution becomes 300 μm. Table 4 provides the performance of BCM and BPM in use at JLab.

I_{beam} (μA)	BCM (dBm)	σ_{BCM} @ 1 Hz (pA)	BPM (dBm)	σ_{BPM} @ 1 Hz (μm)
0.01	-80	$\leq$ 500	-120	300
0.10	-60		-100	30
1	-40		-80	3
10	-20		-60	0.3
100	0		-40	0.03

Table 4: Summary of expected BCM and M15 BPM performance from JLab experience.

C Magnetic Field Considerations

The SoLID magnetic solenoid features a 1.4 T axial magnetic field that extends 3.5 m in length, with a magnet bore of 3 m in diameter. As seen in Fig. 4, the magnet features a large open region where the magnetic field needs to be mapped; on the downstream side, an end cap region houses most of the detectors. The desired magnetic field integral accuracy for the both SIDIS and PVDIS programs is $\Delta B/B = 0.2\%$. For the proposed measurement, the requirement is much higher, at the 10^{-5} level, see Section 5.1. Meeting this goal requires high-precision magnetic field sensors. Additionally, the location of the field sensors should be known to $\leq$1 mm.

In Sec. C.2, we discuss a field mapping solution that will provide 10^{-6} (ppm) level accuracy and precision in $\Delta B/B$. We also discuss possible solutions for improving the field uniformity in Sec. C.3 and stabilizing and tracking the field in Sec. C.4. The techniques discussed below have been successfully used for work related to the Fermilab Muon $g-2$ Experiment. More specifically, these techniques improved the magnetic field uniformity of an MRI solenoid at Argonne National Lab to the few ppm level, which established the method for the absolute calibration system for Muon $g-2$, a critical system for the magnetic field quality. With this design, the difference in the scattered particle's momenta can be controlled to much below the relative 10^{-5} level between e^+ and e^- runs.

C.1 Magnetic Field Quality in Reversed Polarity Mode

Based on Opera simulations [65], it is not anticipated that changing the polarity of the magnet would significantly change the magnetic field vector along the main bore and the first $\approx$1/4 of the detector region. This is because the hysteresis B-H curve of the steel that encloses these regions is flat for the range of B magnitudes needed for SoLID. However, in the remainder of the detector region the B-H curve response becomes more linear, and it is anticipated that the magnetic field could change by up to about 2 mT (20 G). Given that the anticipated magnetic field magnitude in this region is of order 7.5 mT (75 G) for the nominal magnet polarity, such a large possible change requires a magnetic field map once the polarity of the magnet is flipped.

C.2 Field Mapper System

C.2.1 Design Concept

A field mapping system that sufficiently quantifies the magnetic field in the magnet will consist of a symmetrical, circular array of magnetometers mounted to a translation stage that can move the magnetometer assembly along the magnet geometrical axis. The stage can be driven either by hand or by a non-magnetic motor in discrete steps. At a given axial location, a measurement is performed where a magnetic field reading is taken on each of the magnetometers on the assembly. At a given axial location, the magnetometer array can be rotated to a new azimuthal location and the measurement procedure is repeated; this process is completed for all azimuthal angles to cover the full 2π coverage of the solenoid. After the full azimuth is mapped, the assembly is moved to the next axial position and the process repeats. A concept sketch is given in Fig. 22.

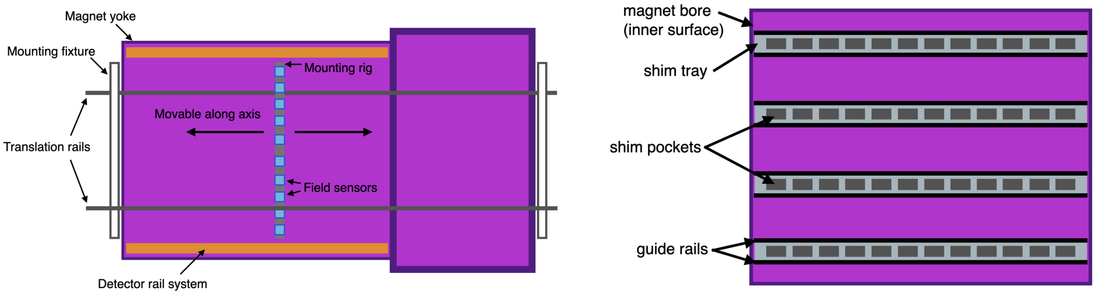

a) Field Mapper design concept. A mounting rig equipped with Hall magnetometers slides along rails centered on the magnet bore to measure the magnetic field at various axial locations.

b) Magnetic field shimming design concept. Trays of insertable iron pieces organized into pockets along the length of the magnet are mounted to the inner lining of the magnet bore.

Figure 22: The concept for the magnetic field mapping system (a) and fixed passive shim trays (b) for the SoLID magnet.

C.2.2 Sensor Selection, Calibration, and Positioning

An optimal choice of magnetometer sensor for the purposes of SoLID is a 3D Hall probe, which measure all three components of the magnetic field. Probes from the Senis company [66] are capable of ppm resolution and accurate to $<$100 ppm in $\Delta B/B$, exceeding the requirements stated above. The absolute scale of the magnetic field measured by the sensors can be improved by a calibration procedure that compares the Hall probe readings to those of an NMR-based magnetometer. Proton NMR relates the Larmor precession frequency f_p of protons to the magnetic field strength B via $f_p = (\gamma_p/2\pi)\,B$. Proton-rich NMR samples are used as an absolute benchmark because the proton gyromagnetic ratio γ_p is known to very high precision [67] exceeding that which would impact the precision of the magnetic field measurements. This allows the absolute magnetic field strength B to be extracted from the Larmor precession frequency that is measured in NMR.

The calibration procedure is as follows: the Hall probe and the NMR probe are swapped back and forth into the same location in a magnet (which is highly uniform in magnetic field magnitude) and their measurements are compared. The JLab Magnet Measurement Group has magnets that can facilitate such measurements. Positioning the two probes in the same location is accomplished by constructing a specialized mounting rig that allows swapping the probes back and forth in controlled step sizes so that their sensor centers are aligned. Such a step size can be accomplished by an encoder-equipped motion-controlled system. The encoders that mark the position of the rig are calibrated by performing controlled motions referenced to fiducial monuments that are surveyed by a laser-tracking system. With laser tracking typically yielding $<$1 mm accuracy, this will ensure accurate positioning of the two probes during the calibration procedure. Additionally, laser tracking and survey alignment for the field mapper device will enable sub-mm positioning accuracy. We can leverage the experience, expertise, and resources of JLab Magnet Measurement Group, working collaboratively with them to develop and build both the calibration system and the field mapper.

C.3 Magnetic Field Uniformity

A common technique used in the operation of MRI solenoid magnets, which have very similar geometry to the SoLID magnet, is to shape the magnetic field to be uniform (generally called "shimming") by the placement of small iron pieces at the perimeter of the magnet bore [68]. This process is called passive shimming since the iron pieces are fixed in space, held in pockets affixed to the inner diameter of the magnet bore, see Fig. 22. The size and amount of iron pieces to place at a given location along the magnet axis is determined by an algorithm which derives from methods developed at General Electric [69, 70] for determining shim coil currents to minimize magnetic field inhomogeneities. The general algorithm is that of a least-squares minimization problem to determine the placement and quantity of (assumed saturated) iron pieces in shim tray pockets in order to minimize the peak-to-peak variation of the magnetic field. After these iron pieces are inserted into the trays, the field is mapped and the process iterates. Typically, the magnet must be ramped down to zero field in order to manipulate the iron pieces. Based on previous experience with MRI solenoid magnets, which have a very similar geometry to that of the SoLID magnet, it takes roughly 1–2 weeks to shim the field to the desired uniformity ($\leq$10 ppm level in $\Delta B/B$). The physical size of the trays that house the iron pieces can be as small as 2 inches long by 0.7 inches tall, extending the whole length of the magnet bore. This relatively compact size can work well with the planned occupancy of the magnet bore by the main detector systems.

C.4 Magnetic Field Tracking and Stabilization

While accurate and precise magnetic field maps are critical for particle tracking, magnetic field stability is also important; if the magnetic field drifts during the experiment due temperature changes (which can cause the magnet yoke steel and coils to expand or contract), then the magnetic field magnitude at any given point in the bore may change. If this change is not tracked, then the track reconstruction will be incorrect given an initial magnetic field map at some earlier time. To mitigate this, magnetic field sensors can be installed in the magnet bore at fixed locations along its inner diameter to monitor the magnetic field components as they change over time. The field sensor data is used to feed back to the magnet power supply to make small changes to the magnet current to maintain a stable magnetic field. This can be accomplished by using a proportional-integral-derivative (PID) feedback loop; using a programmable current source, the measured error field (the difference in the measured field and the desired field) is converted into a small current (typically $\leq$few mA) that is delivered to the main magnet power supply in order to make small changes to the magnetic field to maintain the desired value. The time scale of the feedback loop is determined in a dedicated study that observes the time it takes for the magnetic field to change relative to when its magnet current was changed.

C.4.1 Radiation Protection Considerations

The Senis Hall probes have a CMOS integrated magnetic field sensor epoxied to a ceramic structure. At the inner diameter of the magnet bore, the neutron fluence is estimated to be $\sim 10^{14}$ n/cm^2 [71]; at this level, the ceramics and electronics of the sensor will be susceptible to radiation damage. This indicates that shielding for the sensors will be important for radiation protection.

D Parton-Model Derivation for Lepton DIS Asymmetries

In this section, we will derive parton-model expressions for the asymmetries of lepton deep inelastic scattering off a nucleon or nuclear target that arise from the interference between electromagnetic and electroweak neutral current (NC) interactions. We will focus on the low energy approximation, i.e., at energies much below the mass of the Z^0. These derivations lead to the parton-model NC asymmetries given in Ref. [11].

D.1 Definitions and conventions

We will follow mostly the convention of Halzen&Martin, and the γ-matrix algebra from Griffiths and Peskin&Schroeder. Kinematics of lepton-quark scattering are defined in Fig. 23. The photon-fermion vertex term [Eq. (5.17) of Halzen&Martin] is $-ie\gamma^\mu Q$ with Q the fermion electric charge in units of $e = \sqrt{4\pi\alpha}$. The Z^0-fermion vertex term is

$$-i\frac{g}{\cos\theta_W}\gamma^\mu\frac{1}{2}\left(c_V^f - c_A^f\gamma^5\right) ,$$

where θ_W is the weak mixing angle, and $c_{V,A}^f$ are the vector and the axial-vector charge of the fermion, respectively, see Table 5.

fermion	Q_f	c_A^f	c_V^f
ν_e, ν_μ, ν_τ	0	$\frac{1}{2}$	$\frac{1}{2}$
e^-, μ^-, τ^-	-1	$-\frac{1}{2}$	$-\frac{1}{2} + 2\sin^2\theta_W \approx -0.03$
u, c, t	$\frac{2}{3}$	$\frac{1}{2}$	$\frac{1}{2} - \frac{4}{3}\sin^2\theta_W \approx 0.19$
d, s, b	$-\frac{1}{3}$	$-\frac{1}{2}$	$-\frac{1}{2} + \frac{2}{3}\sin^2\theta_W \approx -0.34$

Table 5: Electromagnetic and electroweak NC couplings for leptons and quarks in the Standard Model, reproduced from Table 13.2 of Halzen&Martin. Anti-fermions have the same coupling as fermions.

The photon and the Z^0 propagator terms are

$$-i\frac{g_{\mu\nu}}{q^2} \qquad \text{and} - i\frac{g_{\mu\nu} - \frac{q_\mu q_\nu}{M_Z^2}}{q^2 - M_Z^2} , \tag{74}$$

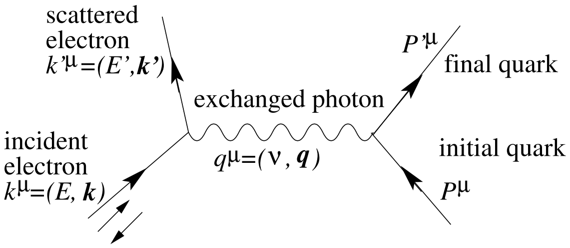

Figure 23: One-photon exchange of electron-quark scattering. For electroweak neutral current interaction, replace the photon by a Z^0 boson.

respectively, where M_Z is the Z^0 mass.

D.2 Adding AA term to the neutral current weak interaction Lagrangian

We first go through the exercise of deriving the amplitude of neutral current weak interactions in DIS to check the VV and AA terms of the Lagrangian. Using Feynman calculus, we write the amplitude of NC eq scattering as:

$$\frac{1}{i}\mathcal{M}_{NC} = \bar{l}_f \left[-i\frac{g}{\cos\theta_W}\gamma^\mu \frac{1}{2}\left(c_V^l - c_A^l\gamma^5\right)\right] l_i \left(-i\frac{g_{\mu\nu} - \frac{q_\mu q_\nu}{M_Z^2}}{q^2 - M_Z^2}\right) \bar{q}_f \left[-i\frac{g}{\cos\theta_W}\gamma^\nu \frac{1}{2}\left(c_V^q - c_A^q\gamma^5\right)\right] q_i \; ,$$

where $l_{i,f}$ and $q_{i,f}$ are the Dirac spinors for the initial and the final state electrons and quarks, respectively. The couplings g is related to the Fermi constant using Eq.(13.35) of PDG [10]:

$$\frac{G_F}{\sqrt{2}} = \frac{g^2}{8M_Z^2\cos^2\theta_W} \; . \tag{75}$$

Combined with the limit $|q^2| \ll M_Z^2$ we obtain:

$$\begin{aligned} \mathcal{M}_{NC} &= 4\sqrt{2}G_F\left[\bar{l}_f\gamma^\mu\frac{1}{2}\left(c_V^l - c_A^l\gamma^5\right)l_i\right]g_{\mu\nu}\left[\bar{q}_f\gamma^\nu\frac{1}{2}\left(c_V^q - c_A^q\gamma^5\right)q_i\right] & (76)\\ &= -\frac{G_F}{\sqrt{2}}\Big[-2c_V^l c_V^q \bar{l}_f\gamma^\mu l_i\bar{q}_f\gamma_\mu q_i + 2c_V^l c_A^q \bar{l}_f\gamma^\mu l_i \bar{q}_f\gamma_\mu\gamma^5 q_i \\ &\quad +2c_A^l c_V^q \bar{l}_f\gamma^\mu\gamma^5 l_i\bar{q}_f\gamma_\mu q_i - 2c_A^l c_A^q \bar{l}_f\gamma^\mu\gamma^5 l_i\bar{q}_f\gamma_\mu\gamma^5 q_i\Big] \; . & (77) \end{aligned}$$

If we define effective couplings $g_{VV}^{eq} \equiv -2c_V^l c_V^q$, $g_{VA}^{eq} = C_{2q} \equiv 2c_V^l c_A^q$, $g_{AV}^{eq} = C_{1q} \equiv 2c_A^l c_V^q$ and $g_{AA}^{eq} = C_{3q} \equiv -2c_A^l c_A^q$ then

$$\begin{aligned} \mathcal{M}_{NC} &= -\frac{G_F}{\sqrt{2}}\left[g_{VV}^{eq}\bar{l}_f\gamma^\mu l_i\bar{q}_f\gamma_\mu q_i + g_{VA}^{eq}\bar{l}_f\gamma^\mu l_i\bar{q}_f\gamma_\mu\gamma^5 q_i\right. \\ &\quad \left. +g_{AV}^{eq}\bar{l}_f\gamma^\mu\gamma^5 l_i\bar{q}_f\gamma_\mu q_i + g_{AA}^{eq}\bar{l}_f\gamma^\mu\gamma^5 l_i\bar{q}_f\gamma_\mu\gamma^5 q_i\right] \; . \end{aligned} \tag{78}$$

Note the signs of the effective couplings are defined such that all of the g terms have the same (positive) sign on the RHS of Eq. (78). Comparing this with Eq.(10.21d) of PDG [10] we see that the neutral weak interaction Lagrangian that includes the AA term should be

$$\mathcal{L}_{int}^{NC} = \frac{G_F}{\sqrt{2}}\left[g_{VA}^{eq}\bar{l}_f\gamma^\mu l_i\bar{q}_f\gamma_\mu\gamma^5 q_i + g_{AV}^{eq}\bar{l}_f\gamma^\mu\gamma^5 l_i\bar{q}_f\gamma_\mu q_i + g_{AA}^{eq}\bar{l}_f\gamma^\mu\gamma^5 l_i\bar{q}_f\gamma_\mu\gamma^5 q_i\right] . \tag{79}$$

We will use the notation $C_{1,2,3}$ and $g_{AV,VA,AA}$ interchangeably though there is a difference in their definition that involves higher-order electroweak radiative corrections.

D.3 The one-photon exchange amplitude

The derivation of $\mathcal{M}_\gamma$ is "textbook" material but we describe it here to show the Feynman calculus and establish convention that we follow throughout this appendix. Using the photon vertex term from D.1 and the projection operator $P_h \equiv \frac{1+h\gamma^5}{2}$ with $h = +1(-1)$ for right(left)-handed lepton spinors, the one-photon exchange amplitude for initial leptons with helicity h is

$$\mathcal{M}_{\gamma,h} \quad = \quad -Q_l Q_q \frac{4\pi\alpha}{q^2} (\bar{l}_f \gamma^\mu P_h l_i)(\bar{q}_f \gamma_\mu q_i) \; . \tag{80}$$

We emphasize here that we are deriving the amplitude lepton scattering off quarks. The case of anti-leptons or anti-quarks will be provided in a later section.

The cross section of electromagnetic process is given by

$$\begin{aligned} |\mathcal{M}_h^\gamma|^2 \quad &= \quad Q_l^2 Q_q^2 \left(\frac{4\pi\alpha}{q^2}\right)^2 \left[(\bar{l}_f \gamma^\mu P_h l_i)(\bar{q}_f \gamma_\mu q_i)\right]^* \left[(\bar{l}_f \gamma^\nu P_h l_i)(\bar{q}_f \gamma_\nu q_i)\right] \\ &= \quad Q_l^2 Q_q^2 \left(\frac{4\pi\alpha}{q^2}\right)^2 (\bar{q}_f \gamma_\mu q_i)^\dagger \left(\bar{l}_f \gamma^\mu P_h l_i\right)^\dagger \left(\bar{l}_f \gamma^\nu P_h l_i\right) \left(\bar{q}_f \gamma_\nu q_i\right) \; . \end{aligned} \tag{81}$$

Using

$$[\bar{u}(b)\Gamma u(b)]^\dagger \quad = \quad \bar{u}(b)\bar{\Gamma}^\dagger u(b) \tag{82}$$

with $u(b)$ any spinor state, Γ any 4×4 matrix and $\bar{\Gamma}^\dagger \equiv \gamma^0 \Gamma^\dagger \gamma^0$, we obtain:

$$|\mathcal{M}_h^\gamma|^2 \quad = \quad Q_l^2 Q_q^2 \left(\frac{4\pi\alpha}{q^2}\right)^2 \left(\bar{l}_i \gamma^0 P_h^\dagger \gamma^{\mu\dagger} \gamma^0 l_f\right) \left(\bar{l}_f \gamma^\nu P_h l_i\right) \left(\bar{q}_i \gamma^0 \gamma_\mu^\dagger \gamma^0 q_f\right) \left(\bar{q}_f \gamma_\nu q_i\right) \; . \tag{83}$$

Then we use $P_h^\dagger = P_h$ and $\gamma^0 \gamma_\mu^\dagger \gamma_0 = \gamma_\mu$ to obtain $\gamma^0 P_h^\dagger \gamma^{\mu\dagger} \gamma^0 = P_{-h} \gamma^0 \gamma^{\mu\dagger} \gamma^0 = P_{-h} \gamma^\mu$, and that when summing over all final spin states $\sum_{s_f=1,2} l_f \bar{l}_f = \not{k}'$ and $\sum_{s_f=1,2} q_f \bar{q}_f = \not{P}'$ for massless particles, we obtain:

$$\sum_{\text{all final spins}} |\mathcal{M}_h^\gamma|^2 \quad = \quad Q_l^2 Q_q^2 \left(\frac{4\pi\alpha}{q^2}\right)^2 \left(\bar{l}_i P_{-h} \gamma^\mu \not{k}' \gamma^\nu P_h l_i\right) \left(\bar{q}_i \gamma_\mu \not{P}' \gamma_\nu q_i\right) \; .$$

The P_{-h} and the P_h on the RHS above are redundant ($\gamma^5 \gamma^\mu = -\gamma^\mu \gamma^5$). Furthermore we use the trace theorem that

$$\sum_{s_a=1,2} \bar{u}(a) Q u(a) \quad = \quad \mathrm{Tr}\left[(\not{p}_a + m_a) Q\right] \tag{84}$$

where $u(a)$ is any Dirac spinor state of 4-momentum p_a and Q is any 4×4 matrix, we obtain:

$$\begin{aligned} \sum_{\text{all spins}} |\mathcal{M}_h^\gamma|^2 \quad &= \quad Q_l^2 Q_q^2 \left(\frac{4\pi\alpha}{q^2}\right)^2 \mathrm{Tr}\left[\not{k} \gamma^\mu \not{k}' \gamma^\nu P_h\right] \mathrm{Tr}\left[\not{P} \gamma_\mu \not{P}' \gamma_\nu\right] \\ &= \quad Q_l^2 Q_q^2 \left(\frac{4\pi\alpha}{q^2}\right)^2 \frac{1}{2} \left\{ \left[4k^\mu k'^\nu + 4k'^\mu k^\nu - 4g^{\mu\nu}(k \cdot k') + h k_\alpha k'_\beta 4i\epsilon^{\mu\alpha\nu\beta}\right] \right. \\ &\qquad \left. \cdot \left[4P_\mu P'_\nu + 4P'_\mu P_\nu - 4g_{\mu\nu}(P \cdot P')\right] \right\} \; . \end{aligned} \tag{85}$$

Next we note that terms like $k_\alpha k'_\beta \epsilon^{\mu\alpha\nu\beta} 4g_{\mu\nu}(P \cdot P') = 0$ always because $\epsilon^{\mu\alpha\nu\beta} = 0$ if $\mu = \nu$, and $g^{\mu\nu} \neq 0$ only for $\mu = \nu$. Terms like $k_\alpha k'_\beta \epsilon^{\mu\alpha\nu\beta}(P_\mu P'_\nu + P'_\mu P_\nu) = 0$ always because

$\epsilon^{\mu\alpha\nu\beta} = -\epsilon^{\nu\alpha\mu\beta}$ (anti-symmetric under $\mu \leftrightarrow \nu$) but $P_\mu P'_\nu + P'_\mu P_\nu = P_\nu P'_\mu + P'_\nu P_\mu$ (symmetric under $\mu \leftrightarrow \nu$). The remaining non-zero terms give us:

$$\sum_{\text{all spin states}} |\mathcal{M}_h^\gamma|^2 = 8Q_l^2 Q_q^2 \left(\frac{4\pi\alpha}{q^2}\right)^2 \left[2(P\cdot k)(P'\cdot k') + 2(P\cdot k')(P'\cdot k)\right] .$$

Using Mandelstan variables $s \equiv (k+P)^2$and $u \equiv (k+P')^2$, and ignoring lepton or quark masses, we have $s = 2k\cdot P = 2k'\cdot P'$ and $u = 2k\cdot P' = 2k'\cdot P = -(1-y)s$:

$$\sum_{\text{all spin}} |\mathcal{M}_h^\gamma|^2 = 4Q_l^2 Q_q^2 \left(\frac{4\pi\alpha}{q^2}\right)^2 s^2 \left[1+(1-y)^2\right] . \tag{86}$$

D.4 The $Z - \gamma^*$ interference term

To derive the amplitude for the $Z - \gamma^*$ interference term, we use Eq. (80) for $\mathcal{M}_\gamma$ with initial lepton beam of helicity h, and for Z exchange we add initial helicity projector to the intial lepton spinor of Eqs. (76-77):

$$\mathcal{M}_{NC}^h = \sqrt{2}G_F \left[\bar{l}_f\gamma^\mu \left(c_V^l - c_A^l\gamma^5\right) P_h l_i\right] \left[\bar{q}_f\gamma_\mu \left(c_V^q - c_A^q\gamma^5\right) q_i\right] , \tag{87}$$

The interference term is $\mathcal{M}_\gamma^* \mathcal{M}_Z + \mathcal{M}_\gamma \mathcal{M}_Z^*$ and that below we only give expressions for $\mathcal{M}_\gamma^* \mathcal{M}_Z$. The corresponding expressions for $\mathcal{M}_\gamma \mathcal{M}_Z^*$ are obtained from the hermitian conjugate.

$$\begin{aligned} &\mathcal{M}_\gamma^{h\,*}\mathcal{M}_{NC}^h \\ = \;& -Q_l Q_q \frac{4\pi\alpha}{q^2} \left[(\bar{l}_f\gamma^\mu P_h l_i)(\bar{q}_f\gamma_\mu q_i)\right]^* \sqrt{2}G_F \bar{l}_f\gamma^\nu(c_V^l - c_A^l\gamma^5)P_h l_i \bar{q}_f\gamma_\nu(c_V^q - c_A^q\gamma^5)q_i \\ = \;& -\frac{4\sqrt{2}\pi G_F\alpha}{q^2} Q_l Q_q (\bar{l}_i P_{-h}\gamma^\mu l_f)\left[\bar{l}_f\gamma^\nu(c_V^l - c_A^l\gamma^5)P_h l_i\right] \cdot (\bar{q}_i\gamma_\mu q_f)\left[\bar{q}_f\gamma_\nu(c_V^q - c_A^q\gamma^5)q_i\right] . \end{aligned}$$

Summing over all initial and final spins, and using the same tricks as in previous section:

$$\begin{aligned} \sum_{\text{all spins}} \mathcal{M}_\gamma^{h\,*}\mathcal{M}_{NC}^h = \;& -\frac{4\sqrt{2}\pi G_F\alpha}{q^2} Q_l Q_q \\ & \cdot \mathrm{Tr}\left[\not{k}\gamma^\mu \not{k}'\gamma^\nu(c_V^l - c_A^l\gamma^5)P_h\right] \mathrm{Tr}\left[\not{P}\gamma_\mu \not{P}'\gamma_\nu(c_V^q - c_A^q\gamma^5)\right] . \end{aligned} \tag{88}$$

Now we deal with the trace terms. First,

$$\begin{aligned} &\mathrm{Tr}\left[\not{k}\gamma^\mu \not{k}'\gamma^\nu(c_V^l - c_A^l\gamma^5)P_h\right] \\ = \;& (c_V^l - hc_A^l)2\left[k^\mu k'^\nu + k'^\mu k^\nu - g^{\mu\nu}(k\cdot k')\right] + (hc_V^l - c_A^l)k_\alpha k'_\beta(2i)\epsilon^{\mu\alpha\nu\beta} . \end{aligned}$$

By letting $h = 0$, $k \to P$ and $k' \to P'$ in the result above and multiply by 2, we obtain

$$\mathrm{Tr}\left[\not{P}\gamma_\mu \not{P}'\gamma_\nu(c_V^q - c_A^q\gamma^5)\right] = (c_V^q)4\left[P_\mu P'_\nu + P'_\mu P_\nu - g_{\mu\nu}(P\cdot P')\right] - c_A^q P^\alpha P'^\beta(4i)\epsilon_{\mu\alpha\nu\beta} .$$

Plugging both trace results into Eq. (88):

$$
\begin{aligned}
&\sum_{\text{all spins}} \mathcal{M}_{\gamma}^{h\,*} \mathcal{M}_{NC}^{h} \\
= \quad & -\frac{4\sqrt{2}\pi G_F \alpha}{q^2} Q_l Q_q 8 \left[(c_V^l - h c_A^l)(k^\mu k'^\nu + k'^\mu k^\nu - g^{\mu\nu} k \cdot k') + i (h c_V^l - c_A^l) k_\alpha k'_\beta \epsilon^{\mu\alpha\nu\beta} \right] \\
& \left[c_V^q (P_\mu P'_\nu + P'_\mu P_\nu - g_{\mu\nu} P \cdot P') - i c_A^q P^\alpha P'^\beta \epsilon_{\mu\alpha\nu\beta} \right] \ . \qquad (89)
\end{aligned}
$$

Following the same argument as for Eq. (85), some terms on the RHS are always zero after the implied summation. Furthermore, using $\epsilon\epsilon$ rule, one obtains

$$
\begin{aligned}
&\sum_{\text{all spins}} \mathcal{M}_{\gamma}^{h\,*} \mathcal{M}_{NC}^{h} \\
= \quad & -\frac{32\sqrt{2}\pi G_F \alpha}{q^2} Q_l Q_q \left[(c_V^l - h c_A^l)(k^\mu k'^\nu + k'^\mu k^\nu - g^{\mu\nu} k \cdot k') c_V^q (P_\mu P'_\nu + P'_\mu P_\nu - g_{\mu\nu} P \cdot P') \right. \\
& \left. + (h c_V^l - c_A^l) k_\alpha k'_\beta c_A^q P^\rho P'^\sigma (-2)(\delta_\rho^\alpha \delta_\sigma^\beta - \delta_\rho^\beta \delta_\sigma^\alpha) \right] \qquad (90) \\
= \quad & -\frac{32\sqrt{2}\pi G_F \alpha}{q^2} Q_l Q_q \left\{ 2(k \cdot P)(k' \cdot P') \left[c_V^l c_V^q - h c_A^l c_V^q - h c_V^q c_A^q + c_A^l c_A^q \right] \right. \\
& \left. + 2(k \cdot P')(k' \cdot P) \left[c_V^l c_V^q - h c_A^l c_V^q + h c_V^q c_A^q - c_A^l c_A^q \right] \right\} \ . \qquad (91)
\end{aligned}
$$

Plugging in $s = 2k \cdot P$ and $u = 2k' \cdot P = -s(1-y)$:

$$
\begin{aligned}
&\sum_{\text{all spins}} \mathcal{M}_{\gamma}^{h\,*} \mathcal{M}_{NC}^{h} \\
= \quad & -\frac{32\sqrt{2}\pi G_F \alpha}{q^2} Q_l Q_q \left\{ \frac{s^2}{2} \left[c_V^l c_V^q - h c_A^l c_V^q - h c_V^l c_A^q + c_A^l c_A^q \right] \right. \\
& \left. + \frac{u^2}{2} \left[c_V^l c_V^q - h c_A^l c_V^q + h c_V^l c_A^q - c_A^l c_A^q \right] \right\} \\
= \quad & -\frac{16\sqrt{2}\pi G_F \alpha}{q^2} Q_l Q_q s^2 \\
& \times \left\{ (c_V^l c_V^q - h c_A^l c_V^q)[1 + (1-y)^2] + (-h c_V^l c_A^q + c_A^l c_A^q)[1 - (1-y)^2] \right\} \ . \qquad (92)
\end{aligned}
$$

D.5 Treatment of antiparticles

We first rewrite Eq. (80) and Eq. (87) using the usual notation u in place of l for the Dirac spinor of particles:

$$
\mathcal{M}_{\gamma,h}^{lq} = -Q_l Q_q \frac{4\pi\alpha}{q^2} (\bar{u}_f \gamma^\mu P_h u_i)(\bar{q}_f \gamma_\mu q_i) \ , \qquad (93)
$$

$$
\mathcal{M}_{NC,h}^{lq} = \sqrt{2} G_F \left[\bar{u}_f \gamma^\mu \left(c_V^l - c_A^l \gamma^5 \right) P_h u_i \right] \left[\bar{q}_f \gamma_\mu \left(c_V^q - c_A^q \gamma^5 \right) q_i \right] \ . \qquad (94)
$$

For anti-lepton $\bar{l} - q$ scattering where the intial anti-lepton has helicity h, Eq. (93) becomes

$$\mathcal{M}^{\bar{l}q}_{\gamma,h} = -Q_l Q_q \frac{4\pi\alpha}{q^2}(\bar{v}_i P_h \gamma^\mu v_f)(\bar{q}_f \gamma_\mu q_i) = -Q_l Q_q \frac{4\pi\alpha}{q^2}(\bar{v}_i \gamma^\mu P_{-h} v_f)(\bar{q}_f \gamma_\mu q_i) ,$$

and Eq. (87) becomes

$$\begin{aligned}\mathcal{M}^{\bar{l}q}_{NC,h} &= \sqrt{2}G_F \left[\bar{v}_i P_h \gamma^\mu \left(c^l_V - c^l_A \gamma^5\right) v_f\right] \left[\bar{q}_f \gamma_\mu \left(c^q_V - c^q_A \gamma^5\right) q_i\right] \\ &= \sqrt{2}G_F \left[\bar{v}_i \gamma^\mu \left(c^l_V - c^l_A \gamma^5\right) P_{-h} v_f\right] \left[\bar{q}_f \gamma_\mu \left(c^q_V - c^q_A \gamma^5\right) q_i\right] ,\end{aligned}$$

where we used $\gamma^5\gamma^\mu = -\gamma^\mu\gamma^5$, which gives $P_h\gamma^\mu = \gamma^\mu P_{-h}$ and $P_h\gamma^5 = \gamma^5 P_h$. Since the derivation of $\mathcal{M}^{h\,*}_\gamma \mathcal{M}^h_{NC}$ stays the same for anti-particles (note that both Eqs. (82) and (84) remain the same for anti-particle spinor v in the massless limit), we can use lq result [Eq. (91)] for $\bar{l}q$ with the substitution $h \to -h$ and switch the initial vs. the final lepton wavefunction $i \leftrightarrow f$ (or $k \leftrightarrow k'$ since that's the only thing matters). Starting from Eq. (91) and do the above required substitutions ($h \to -h$ and $k \leftrightarrow k'$), we have:

$$\begin{aligned}&\sum_{\text{all spins}} \mathcal{M}^{h\,*}_\gamma \mathcal{M}^h_{NC}(\text{for } \bar{l}q) \\ =& -\frac{32\sqrt{2}\pi G_F \alpha}{q^2} Q_l Q_q \Big\{2(k'\cdot P)(k\cdot P')\left[c^l_V c^q_V + h c^l_A c^q_V + h c^q_V c^q_A + c^l_A c^q_A\right] \\ &+2(k'\cdot P')(k\cdot P)\left[c^l_V c^q_V + h c^l_A c^q_V - h c^q_V c^q_A - c^l_A c^q_A\right]\Big\} \\ =& -\frac{32\sqrt{2}\pi G_F \alpha}{q^2} Q_l Q_q \Big\{2(k\cdot P)(k'\cdot P')\left[c^l_V c^q_V + h c^l_A c^q_V - h c^q_V c^q_A - c^l_A c^q_A\right] \\ &+2(k\cdot P')(k'\cdot P)\left[c^l_V c^q_V + h c^l_A c^q_V + h c^q_V c^q_A + c^l_A c^q_A\right]\Big\} \qquad (95)\end{aligned}$$

Comparing the above with Eq. (91) we can see that the difference between $\bar{l}q$ and lq can be equivalently treated as an algebraic flip of the signs of both h and c^q_A. Using sign flip rather than switching the 4-momentum vectors allows us to use Eq. (92) directly for anti-particles.

For anti-quarks we have similar results. For $l - \bar{q}$ scattering, Eq. (80) becomes

$$\mathcal{M}^{l\bar{q}}_{\gamma,h} = -Q_l Q_q \frac{4\pi\alpha}{q^2}(\bar{u}_f \gamma^\mu P_h u_i)(\bar{v}_i \gamma_\mu v_f) ,$$

and Eq. (87) becomes

$$\mathcal{M}^{l\bar{q}}_{NC,h} = \sqrt{2}G_F \left[\bar{u}_f \gamma^\mu \left(c^l_V - c^l_A \gamma^5\right) P_h u_i\right] \left[\bar{q}_i \gamma^\mu \left(c^q_V - c^q_A \gamma^5\right) q_f\right] ,$$

where the $q_{i,f}$ are Dirac spinors for the initial and the final anti-quark states, respectively. Thus the only change from the $l - q$ case is $i \leftrightarrow f$ (or $P \leftrightarrow P'$) for the quark states. Starting from

Eq. (91) and do the substitutions $P \leftrightarrow P'$,

$$\begin{aligned}
&\sum_{\text{all spins}} \mathcal{M}_\gamma^{h\,*} \mathcal{M}_{NC}^h (\text{for } l\bar{q}) \\
=&\ -\frac{32\sqrt{2}\pi G_F \alpha}{q^2} Q_l Q_q \Big\{ 2(k \cdot P')(k' \cdot P) \left[c_V^l c_V^q - h c_A^l c_V^q - h c_V^q c_A^q + c_A^l c_A^q \right] \\
&+2(k \cdot P)(k' \cdot P') \left[c_V^l c_V^q - h c_A^l c_V^q + h c_V^q c_A^q - c_A^l c_A^q \right] \Big\} \\
=&\ -\frac{32\sqrt{2}\pi G_F \alpha}{q^2} Q_l Q_q \Big\{ 2(k \cdot P)(k' \cdot P') \left[c_V^l c_V^q - h c_A^l c_V^q + h c_V^q c_A^q - c_A^l c_A^q \right] \\
&+2(k \cdot P')(k' \cdot P) \left[c_V^l c_V^q - h c_A^l c_V^q - h c_V^q c_A^q + c_A^l c_A^q \right] \Big\} \qquad (96)
\end{aligned}$$

Comparing the above with Eq. (91) we can see that again the difference between lq and $l\bar{q}$ can be alternatively treated as a sign flip of c_A^q.

Lastly for $\bar{l} - \bar{q}$ scattering, Eq. (80) becomes

$$\mathcal{M}_{\gamma,h}^{\bar{l}\bar{q}} = -Q_l Q_q \frac{4\pi\alpha}{q^2} (\bar{v}_i P_h \gamma^\mu v_f)(\bar{q}_i \gamma_\mu q_f) = -Q_l Q_q \frac{4\pi\alpha}{q^2} (\bar{v}_i \gamma^\mu P_{-h} v_f)(\bar{q}_i \gamma_\mu q_f)\ ,$$

and Eq. (87) becomes

$$\begin{aligned}
\mathcal{M}_{NC,h}^{\bar{l}\bar{q}} &= \sqrt{2} G_F \left[\bar{v}_i P_h \gamma^\mu \left(c_V^l - c_A^l \gamma^5 \right) v_f \right] \left[\bar{q}_i \gamma^\mu \left(c_V^q - c_A^q \gamma^5 \right) q_f \right] \\
&= \sqrt{2} G_F \left[\bar{v}_i \gamma^\mu \left(c_V^l - c_A^l \gamma^5 \right) P_{-h} v_f \right] \left[\bar{q}_i \gamma^\mu \left(c_V^q - c_A^q \gamma^5 \right) q_f \right]\ ,
\end{aligned}$$

which is lq case with $h \to -h$, $k \leftrightarrow k'$, $P \leftrightarrow P'$. Once again, starting from Eq. (91) and do substitutions $h \to -h$, $k \leftrightarrow k'$, $P \leftrightarrow P'$, and note that the latter two cause no effect in all $k \cdot P'$-like terms:

$$\begin{aligned}
&\sum_{\text{all spins}} \mathcal{M}_\gamma^{h\,*} \mathcal{M}_{NC}^h (\text{for } \bar{l}\bar{q}) \\
=&\ -\frac{32\sqrt{2}\pi G_F \alpha}{q^2} Q_l Q_q \Big\{ 2(k' \cdot P')(k \cdot P) \left[c_V^l c_V^q + h c_A^l c_V^q + h c_V^q c_A^q + c_A^l c_A^q \right] \\
&+2(k' \cdot P)(k \cdot P') \left[c_V^l c_V^q + h c_A^l c_V^q - h c_V^q c_A^q - c_A^l c_A^q \right] \Big\}\ . \qquad (97)
\end{aligned}$$

This time, the difference from the lq case can be alternatively treated as a sign flip of h. Similarly the difference from the $\bar{l}q$ case is a sign flip of c_A^q.

D.6 Electroweak neutral current cross section asymmetries

In this section we use results from the previous two sections to derive asymmetries of lepton scattering of opposite helicities or opposite charges.

D.6.1 PVDIS asymmetry in electron scattering

For cross sectional asymmetry of incident lepton beam of opposite helicities, i.e., PV asymmetry, both the numerator and the denominator are linear combinations of all quarks reside in the target, with proper PDF and charge-weighting used. Also, all Mandelstan variables s, u, t are calculated using $P_{quark} = xP_{nucleon}$ as interpreted in the infinite momentum frame. The asymmetry is defined as the difference between right-handed and left-handed incident electron beam:

$$\begin{aligned}
A^{PV} &= \frac{\sigma_R - \sigma_L}{\sigma_R + \sigma_L} \\
&= \frac{|\mathcal{M}_Z + \mathcal{M}_\gamma|^2_{h=+|\lambda|} - |\mathcal{M}_Z + \mathcal{M}_\gamma|^2_{h=-|\lambda|}}{|\mathcal{M}_Z + \mathcal{M}_\gamma|^2_{h=+|\lambda|} + |\mathcal{M}_Z + \mathcal{M}_\gamma|^2_{h=-|\lambda|}} \approx \frac{2(\mathcal{M}^*_\gamma \mathcal{M}_Z)_{h=+|\lambda|} - 2(\mathcal{M}^*_\gamma \mathcal{M}_Z)_{h=-|\lambda|}}{2|\mathcal{M}_\gamma|^2}
\end{aligned}$$

Using Eq. (92) for the numerator and Eq. (86) for the denominator:

$$\begin{aligned}
A^{PV} &= \frac{\sqrt{2}G_F q^2}{Q_l 4\pi\alpha} \frac{\sum q(x) Q_q \left\{2c^l_A c^q_V[1+(1-y)^2] + 2c^l_V c^q_A[1-(1-y)^2]\right\} |\lambda|}{\sum q(x) Q_q^2 [1+(1-y)^2]} \\
&= \frac{\sqrt{2}G_F q^2}{Q_l 4\pi\alpha} \frac{\sum q(x) Q_q \left[2c^l_A c^q_V + 2c^l_V c^q_A Y(y)\right] |\lambda|}{\sum q(x) Q_q^2}
\end{aligned}$$

where λ is the magnitude of the incident beam's polarization ($R-L$), $q(x)$ are parton distribution functions, and the kinematic function Y is defined as

$$Y(y) \equiv \frac{1-(1-y)^2}{1+(1-y)^2} \,. \tag{98}$$

Plugging in $Q_l = -1$ for electron scattering, $Q^2 \equiv -q^2$ and definitions of C_{1q} and C_{2q}:

$$A^{e^-,\text{PVDIS}} = \frac{\sqrt{2}G_F Q^2}{4\pi\alpha} \frac{\sum q(x) Q_q \left[C_{1q} + C_{2q} Y(y)\right] |\lambda|}{\sum q(x) Q_q^2} \,. \tag{99}$$

For a proton target, counting only u, d, c, s quark flavors and use $C_{1c,2c} = C_{1u,2u}$, $C_{1s,2s} = C_{1d,2d}$, and note for antiquark contribution all c^q_A (and thus all C_{2q}) terms must have an extra minus sign (see Section D.5), we obtain

$$\begin{aligned}
&A^{e^-,\text{PVDIS}}_p = \\
&|\lambda| \frac{\sqrt{2}G_F Q^2}{4\pi\alpha} \frac{\frac{2}{3}[u^+ + c^+]C_{1u} - \frac{1}{3}[d^+ + s^+]C_{1d} + Y[\frac{2}{3}(u_V + c_V)C_{2u} - \frac{1}{3}(d_V + s_V)C_{2d}]}{\frac{4}{9}[u^+ + c^+] + \frac{1}{9}[d^+ + s^+]}
\end{aligned}$$

where $q^+ \equiv q(x) + \bar{q}(x)$ and $q_V \equiv q(x) - \bar{q}(x)$ ($q = u, d, c, s$). If we assume $c = \bar{c}$, $s = \bar{s}$ then $c_V = s_V = 0$ and

$$A^{e^-,\text{PVDIS}}_p = |\lambda| \frac{\sqrt{2}G_F Q^2}{4\pi\alpha} \frac{\frac{2}{3}[u^+ + c^+]C_{1u} - \frac{1}{3}[d^+ + s^+]C_{1d} + Y[\frac{2}{3}u_V C_{2u} - \frac{1}{3}d_V C_{2d}]}{\frac{4}{9}[u^+ + c^+] + \frac{1}{9}[d^+ + s^+]} \,. \tag{100}$$

For the deuteron or any isoscalar target but ignoring nuclear effects, substitute $u \to u + d$ and $d \to u + d$ in the expression for $A^{e^-,\text{PVDIS}}_p$ above and assuming c and s are the same in the proton and the neutron, we obtain:

$$A_d^{e^-,\mathrm{PVDIS}} = |\lambda| \frac{3G_F Q^2}{2\sqrt{2}\pi\alpha} \frac{2(1+R_C)C_{1u} - (1+R_S)C_{1d} + Y[2C_{2u}(1+\epsilon_c) - C_{2d}(1+\epsilon_s)]R_V}{5+4R_C+R_S}\ , \tag{101}$$

where

$$R_V(x) \ \equiv\ \frac{u_V + d_V}{u^+ + d^+}\ ,\ \ R_C(x) \equiv \frac{2(c+\bar{c})}{u^+ + d^+}\ ,\ \ R_S(x) \equiv \frac{2(s+\bar{s})}{u^+ + d^+}\ , \tag{102}$$

and the ϵ's account for $c - \bar{c}$ and $s - \bar{s}$ which are often set to zero in PDF sets:

$$\epsilon_c \ \equiv\ \frac{2(c-\bar{c})}{u^+ + d^+}\ ,\ \ \epsilon_s \equiv \frac{2(s-\bar{s})}{u^+ + d^+}\ . \tag{103}$$

If counting only the light quarks u, d then

$$A_p^{e^-,\mathrm{PVDIS}} \ \approx\ |\lambda| \frac{\sqrt{2}G_F Q^2}{4\pi\alpha} \frac{\frac{2}{3}u^+ C_{1u} - \frac{1}{3}d^+ C_{1d} + Y[\frac{2}{3}u_V C_{2u} - \frac{1}{3}d_V C_{2d}]}{\frac{4}{9}u^+ + \frac{1}{9}d^+} \tag{104}$$

$$A_d^{e^-,\mathrm{PVDIS}} \ \approx\ |\lambda| \frac{3G_F Q^2}{10\sqrt{2}\pi\alpha} \left[(2C_{1u} - C_{1d}) + R_V Y(2C_{2u} - C_{2d})\right]\ . \tag{105}$$

D.6.2 Asymmetry between electron and positron scattering

For the difference between electron and positron scattering, we can define:

$$A_{RL}^{e^+e^-} \equiv \frac{\sigma_R^{e^+} - \sigma_L^{e^-}}{\sigma_R^{e^+} + \sigma_L^{e^-}}, \qquad A_{LR}^{e^+e^-} \equiv \frac{\sigma_L^{e^+} - \sigma_R^{e^-}}{\sigma_R^{e^+} + \sigma_L^{e^-}}, \tag{106}$$

$$A_{LL}^{e^+e^-} \equiv \frac{\sigma_L^{e^+} - \sigma_L^{e^-}}{\sigma_L^{e^+} + \sigma_L^{e^-}}, \qquad A_{RR}^{e^+e^-} \equiv \frac{\sigma_R^{e^+} - \sigma_R^{e^-}}{\sigma_R^{e^+} + \sigma_R^{e^-}}, \tag{107}$$

and

$$A^{e^+e^-} \ \equiv\ \frac{\sigma_{h=0}^{e^+} - \sigma_{h=0}^{e^-}}{\sigma_{h=0}^{e^+} + \sigma_{h=0}^{e^-}}. \tag{108}$$

Note that asymmetries in Eqs. (106) and (107) were called B or B_+ in Ref. [18, 72] and $C_{L,R}$ in Ref. [72], respectively.

Calculations of $A_{RL}^{e^+e^-}$ require:

$$\begin{aligned} A_{RL}^{e^+e^-} &= \frac{|\mathcal{M}_Z^{e^+} + \mathcal{M}_\gamma^{e^+}|^2_{h=+|\lambda|} - |\mathcal{M}_Z^{e^-} + \mathcal{M}_\gamma^{e^-}|^2_{h=-|\lambda|}}{|\mathcal{M}_Z^{e^+} + \mathcal{M}_\gamma^{e^+}|^2_{h=+|\lambda|} + |\mathcal{M}_Z^{e^-} + \mathcal{M}_\gamma^{e^-}|^2_{h=-|\lambda|}} \\ &\approx \frac{2(\mathcal{M}_\gamma^{e^+*}\mathcal{M}_Z^{e^+})_{h=+|\lambda|} - 2(\mathcal{M}_\gamma^{e^-*}\mathcal{M}_Z^{e^-})_{h=-|\lambda|}}{2|\mathcal{M}_\gamma|^2}\ , \end{aligned}$$

where the approximation is valid for $Q^2 \ll M_Z^2$. Again we use Eq. (86) for the numerator and Eq. (92) for the numerator (omitting the summation sign):

$$
\begin{aligned}
\left(\mathcal{M}_h^Z \mathcal{M}_h^{\gamma *}\right)^{eq} &= -\frac{16\sqrt{2}\pi\alpha G_F Q_l Q_q}{q^2} s^2 \\
&\quad \times \left\{ (c_V^l c_V^q - h c_A^l c_V^q)[1+(1-y)^2] + (-h c_V^l c_A^q + c_A^l c_A^q)[1-(1-y)^2] \right\} ,
\end{aligned}
$$

and recall for $e^+ - q$ scattering we flip the signs of both h and c_A^q (see Section D.5):

$$
\begin{aligned}
\left(\mathcal{M}_h^Z \mathcal{M}_h^{\gamma *}\right)^{e^+ q} &= -\frac{16\sqrt{2}\pi\alpha G_F Q_l Q_q}{q^2} s^2 \\
&\quad \times \left\{ (c_V^l c_V^q + h c_A^l c_V^q)[1+(1-y)^2] + (-h c_V^l c_A^q - c_A^l c_A^q)[1-(1-y)^2] \right\} ,
\end{aligned}
$$

we obtain:

$$
\begin{aligned}
& (\mathcal{M}_\gamma^* \mathcal{M}_Z)_{h=+|\lambda|}^{e^+ q} - (\mathcal{M}_\gamma^* \mathcal{M}_Z)_{h=-|\lambda|}^{e^- q} \\
= \; & -\frac{16\sqrt{2}\pi\alpha G_F Q_l Q_q}{q^2} s^2 \\
& \times \left\{ (c_V^l c_V^q + |\lambda| c_A^l c_V^q)[1+(1-y)^2] + (-|\lambda| c_V^l c_A^q - c_A^l c_A^q)[1-(1-y)^2] \right. \\
& \left. -(c_V^l c_V^q + |\lambda| c_A^l c_V^q)[1+(1-y)^2] - (+|\lambda| c_V^l c_A^q + c_A^l c_A^q)[1-(1-y)^2] \right\} \qquad (109)
\end{aligned}
$$

where the first line in the wiggly bracket are from e^+ and the second line is from e^-. The VV and AV terms cancel out between the two, while the VA and AA terms are identical. Plugging in $Q_l = -1$ for the electron, we are left with:

$$
(\mathcal{M}_\gamma^* \mathcal{M}_Z)_{h=+|\lambda|}^{e^+ q} - (\mathcal{M}_\gamma^* \mathcal{M}_Z)_{h=-|\lambda|}^{e^- q} = -\frac{16\sqrt{2}\pi\alpha G_F Q_q}{q^2} s^2 (2|\lambda| c_V^l c_A^q + 2 c_A^l c_A^q)[1-(1-y)^2] .
$$

Conversely, if we form the RR asymmetry then the VV and VA terms cancel while AV and AA terms are identical, leaving only the AV and AA terms:

$$
\begin{aligned}
& (\mathcal{M}_\gamma^* \mathcal{M}_Z)_{h=+|\lambda|}^{e^+ q} - (\mathcal{M}_\gamma^* \mathcal{M}_Z)_{h=+|\lambda|}^{e^- q} \\
= \; & -\frac{16\sqrt{2}\pi\alpha G_F Q_l Q_q}{q^2} s^2 \\
& \times \left\{ (c_V^l c_V^q + |\lambda| c_A^l c_V^q)[1+(1-y)^2] + (-|\lambda| c_V^l c_A^q - c_A^l c_A^q)[1-(1-y)^2] \right. \\
& \left. -(c_V^l c_V^q - |\lambda| c_A^l c_V^q)[1+(1-y)^2] - (-|\lambda| c_V^l c_A^q + c_A^l c_A^q)[1-(1-y)^2] \right\} \\
= \; & \frac{16\sqrt{2}\pi\alpha G_F Q_q}{q^2} s^2 \left\{ 2|\lambda| c_A^l c_V^q [1+(1-y)^2] - 2 c_A^l c_A^q [1-(1-y)^2] \right\} . \qquad (110)
\end{aligned}
$$

For LL one simply flip the sign of $|\lambda|$ above.

For e^+ vs. e^- scattering off a nuclear target, , and note for antiquark contribution all c_A^q (and thus all $C_{2q,3q}$) terms must have an extra minus sign (see Section D.5), we have

$$A_{RL}^{e^+e^-} = \frac{\sum_q -\frac{16\sqrt{2}\pi\alpha G_F}{q^2} s^2[1-(1-y)^2]Q_q[2|\lambda|c_V^l c_A^q + 2c_A^l c_A^q]\,(q(x)-\bar{q}(x))}{\sum_q 4Q_l^2\left(\frac{4\pi\alpha}{q^2}\right)^2 s^2[1+(1-y)^2]Q_q^2\,(q(x)+\bar{q}(x))} \tag{111}$$

Plugging in $Q_l^2 = 1$, $C_{2q} \equiv 2c_V^l c_A^q$, $C_{3q} = -2c_A^l c_A^q$, and $q^2 = -Q^2$:

$$A_{RL}^{e^+e^-} = \frac{G_F}{2\sqrt{2}\pi\alpha}Q^2 Y(y)\frac{\sum_q q_V(x)Q_q(|\lambda|C_{2q} - C_{3q})}{\sum_q q^+(x)Q_q^2}\,. \tag{112}$$

For the proton and considering u, d, c, s

$$A_{RL,p}^{e^+e^-} = \frac{3G_F}{2\sqrt{2}\pi\alpha}Q^2 Y(y)\frac{2|\lambda|(u_V+c_V)C_{2u} - |\lambda|(d_V+s_V)C_{2d} - 2(u_V+c_V)C_{3u} + (d_V+s_V)C_{3d}}{4(u^+ + c^+) + 1(d^+ + s^+)}\,.$$

If we assume $c = \bar{c}$, $s = \bar{s}$ then $c_V = s_V = 0$ and

$$A_{RL,p}^{e^+e^-} = \frac{3G_F}{2\sqrt{2}\pi\alpha}Q^2 Y(y)\frac{2|\lambda|u_V C_{2u} - |\lambda|d_V C_{2d} - 2u_V C_{3u} + d_V C_{3d}}{4(u^+ + c^+) + (d^+ + s^+)}\,. \tag{113}$$

For the deuteron or any isoscalar target and ignoring nuclear effects:

$$A_{RL,d}^{e^+e^-} = \frac{3G_F}{2\sqrt{2}\pi\alpha}Q^2 Y(y) R_V \frac{|\lambda|(2C_{2u} - C_{2d}) - (2C_{3u} - C_{3d})}{5 + 4R_C + R_S}\,. \tag{114}$$

And if only u, d are considered then

$$A_{RL,p}^{e^+e^-} \approx \frac{3G_F}{2\sqrt{2}\pi\alpha}Q^2 Y(y)\frac{2|\lambda|u_V C_{2u} - |\lambda|d_V C_{2d} - 2u_V C_{3u} + d_V C_{3d}}{4(u^+) + (d^+)}\,. \tag{115}$$

$$A_{RL,d}^{e^+e^-} \approx \frac{3G_F}{10\sqrt{2}\pi\alpha}Q^2 Y(y) R_V\left[|\lambda|(2C_{2u} - C_{2d}) - (2C_{3u} - C_{3d})\right]\,. \tag{116}$$

All results above can be extended to $A_{LR}^{e^+e^-}$ if we let $|\lambda| \to -|\lambda|$, and to $A^{e^+e^-}$ if we let $|\lambda| = 0$.

For $A_{RR,LL}^{e^+e^-}$, we start from Eq. (110):

$$A_{RR}^{e^+e^-} = \frac{G_F}{2\sqrt{2}\pi\alpha}Q^2 Y(y)\frac{\sum_q Q_q(-q^+|\lambda|C_{1q} - Y q_V C_{3q})}{\sum_q q^+ Q_q^2}\,. \tag{117}$$

For the proton and considering u, d, c, s

$$\begin{aligned} A_{RR,p}^{e^+e^-} &= \frac{3G_F}{2\sqrt{2}\pi\alpha}Q^2 \\ &\times \frac{-2|\lambda|(u^+ + c^+)C_{1u} + |\lambda|(d^+ + s^+)C_{1d} - 2(u_V + c_V)C_{3u}Y(y) + (d_V + s_V)C_{3d}Y(y)}{4(u^+ + c^+) + 1(d^+ + s^+)}\,. \end{aligned} \tag{118}$$

If we assume $c = \bar{c}$, $s = \bar{s}$ then $c_V = s_V = 0$ and

$$A^{e^+e^-}_{RR,p} = \frac{3G_F}{2\sqrt{2}\pi\alpha} Q^2 \frac{-2|\lambda|(u^+ + c^+)C_{1u} + |\lambda|(d^+ + s^+)C_{1d} - 2u_V C_{3u} Y(y) + d_V C_{3d} Y(y)}{4(u^+ + c^+) + (d^+ + s^+)} \ . \tag{119}$$

For the deuteron or any isoscalar target and ignoring nuclear effects:

$$A^{e^+e^-}_{RR,d} = \frac{3G_F}{2\sqrt{2}\pi\alpha} Q^2 \frac{-|\lambda|[2(1+R_C)C_{1u} - (1+R_S)C_{1d}] - Y(y)R_V(2C_{3u} - C_{3d})}{5 + 4R_C + R_S} \tag{120}$$

And if only u, d are considered then

$$A^{e^+e^-}_{RR,p} \approx \frac{3G_F}{2\sqrt{2}\pi\alpha} Q^2 \frac{-2|\lambda|u^+ C_{1u} + |\lambda|d^+ C_{1d} - 2u_V C_{3u} Y(y) + d_V C_{3d} Y(y)}{4(u^+) + (d^+)} \ . \tag{121}$$

$$A^{e^+e^-}_{RR,d} \approx \frac{3G_F}{10\sqrt{2}\pi\alpha} Q^2 \left[-|\lambda|(2C_{1u} - C_{1d}) - Y(y)R_V(2C_{3u} - C_{3d})\right] \ . \tag{122}$$

References

[1] ATLAS collaboration, M. Aaboud et al., *Observation of $H \to b\bar{b}$ decays and VH production with the ATLAS detector, Phys. Lett. B* ***786*** *(2018) 59–86*, [`1808.08238`].

[2] CMS collaboration, A. M. Sirunyan et al., *Observation of Higgs boson decay to bottom quarks, Phys. Rev. Lett.* ***121*** *(2018) 121801*, [`1808.08242`].

[3] LHCB collaboration, R. Aaij et al., *Test of lepton universality in beauty-quark decays,* `2103.11769`.

[4] MUON G-2 collaboration, B. Abi et al., *Measurement of the Positive Muon Anomalous Magnetic Moment to 0.46 ppm, Phys. Rev. Lett.* ***126*** *(2021) 141801*, [`2104.03281`].

[5] QWEAK collaboration, D. Androić et al., *Precision measurement of the weak charge of the proton, Nature* ***557*** *(2018) 207–211*, [`1905.08283`].

[6] PVDIS collaboration, D. Wang et al., *Measurement of parity violation in electron–quark scattering, Nature* ***506*** *(2014) 67–70.*

[7] D. Wang et al., *Measurement of Parity-Violating Asymmetry in Electron-Deuteron Inelastic Scattering, Phys. Rev. C* ***91*** *(2015) 045506*, [`1411.3200`].

[8] L. S. Cardman, *The PEPPo method for polarized positrons and PEPPo II, AIP Conf. Proc.* ***1970*** *(2018) 050001.*

[9] SOLID collaboration, J. P. Chen, H. Gao, T. K. Hemmick, Z. E. Meziani and P. A. Souder, *A White Paper on SoLID (Solenoidal Large Intensity Device),* `1409.7741`.

[10] PARTICLE DATA GROUP collaboration, P. A. Zyla et al., *Review of Particle Physics, PTEP* ***2020*** *(2020) 083C01.*

[11] X. Zheng, J. Erler, Q. Liu and H. Spiesberger, *Accessing weak neutral-current coupling C_{3q} using positron and electron beams at Jefferson Lab,* `2103.12555`.

[12] D. Becker et al., *The P2 experiment, Eur. Phys. J. A* ***54*** *(2018) 208*, [`1802.04759`].

[13] G. Toh, A. Damitz, C. E. Tanner, W. R. Johnson and D. S. Elliott, *Determination of the scalar and vector polarizabilities of the cesium $6s\ ^2S_{1/2} \to 7s\ ^2S_{1/2}$ transition and implications for atomic parity non-conservation, Phys. Rev. Lett.* ***123*** *(2019) 073002*, [`1905.02768`].

[14] C. Y. Prescott et al., *Parity Nonconservation in Inelastic Electron Scattering, Phys. Lett. B* ***77*** *(1978) 347–352.*

[15] C. Y. Prescott et al., *Further Measurements of Parity Nonconservation in Inelastic electron Scattering, Phys. Lett. B* ***84*** *(1979) 524–528.*

[16] P. Souder et al., "Precision Measurement of Parity-violationin Deep Inelastic Scattering Over a Broad Kinematic Range." JLab E12-10-007, 2010.

[17] J. Erler and S. Su, *The Weak Neutral Current, Prog. Part. Nucl. Phys.* ***71*** *(2013) 119–149*, [`1303.5522`].

[18] A. Argento et al., *Electroweak Asymmetry in Deep Inelastic Muon - Nucleon Scattering, Phys. Lett. B* ***120*** *(1983) 245*.

[19] J. Erler and M. J. Ramsey-Musolf, *Low energy tests of the weak interaction, Prog. Part. Nucl. Phys.* ***54*** *(2005) 351–442*, [`hep-ph/0404291`].

[20] A. Accardi et al., *e^+@JLab White Paper: An Experimental Program with Positron Beams at Jefferson Lab,* `2007.15081`.

[21] A. A. Sokolov and I. M. Ternov, *On polarization and spin effects in the theory of synchrotron radiation, Dokl. Akad. Nauk SSSR* ***153*** *(1963) 1052–1054*.

[22] S. Golge, *Feasibility and Conceptual Design of a CW Positron Source at CEBAF,* .

[23] A. Afanasev et al., *Physics with Positron Beams at Jefferson Lab 12 GeV,* `1906.09419`.

[24] Y. Roblin, *Using* CEBAF *as a positron machine,* .

[25] P. Gueye, "Hall C Energy Drift Monitoring." JLab TN01-056, 2001.

[26] C. Morean, *Target boiling studies using 2018 f_2-xem data,* 2020.

[27] *Opera, electromagnetic and electromechanical simulation,* .

[28] L. A. Harland-Lang, A. D. Martin, P. Motylinski and R. S. Thorne, *Parton distributions in the LHC era: MMHT 2014 PDFs, Eur. Phys. J. C* ***75*** *(2015) 204*, [`1412.3989`].

[29] T. Hou et al., *New CTEQ global analysis of quantum chromodynamics with high-precision data from the LHC, Phys. Rev. D* ***103*** *(2021) 014013*, [`1912.10053`].

[30] D. Flay. private communication, π^+ and π^- cross sections on a ^{3}He target from the 6 GeV d_2^n experiment, 2021.

[31] D. E. Wiser, "Inclusive Photoproduction of Protons, Kaons, and Pions at SLAC Energies." Ph.D. thesis, Univ. of Wisconsin, 1977.

[32] G. Niculescu and I. Niculescu, *The d/p ratio extraction from experiment e12-10-002,* 2021.

[33] P. Guèye, M. Bernheim, J. F. Danel, J. E. Ducret, L. Lakéhal-Ayat, J. M. Le Goff et al., *Coulomb distortion measurements by comparing electron and positron quasielastic scattering off* ^{12}C *and* ^{208}Pb, *Phys. Rev. C* ***60*** *(Sep, 1999) 044308*.

[34] JEFFERSON LAB HALL-A E05-110 collaboration, M. Paolone, *Measuring the Coulomb sum rule at JLab, AIP Conf. Proc.* ***1970*** *(2018) 020010*.

[35] J. Arrington, P. G. Blunden and W. Melnitchouk, *Review of two-photon exchange in electron scattering, Prog. Part. Nucl. Phys.* ***66*** *(2011) 782–833*, [`1105.0951`].

[36] A. Kwiatkowski, H. Spiesberger and H. J. Mohring, *Heracles: An Event Generator for ep Interactions at HERA Energies Including Radiative Processes: Version 1.0, Comput. Phys. Commun.* ***69*** *(1992) 155–172.*

[37] K. Charchula, G. A. Schuler and H. Spiesberger, *Combined QED and QCD radiative effects in deep inelastic lepton - proton scattering: The Monte Carlo generator DJANGO6, Comput. Phys. Commun.* ***81*** *(1994) 381–402.*

[38] H. Spiesberger, *Monte Carlo treatment of radiative corrections at HERA, Nucl. Phys. B Proc. Suppl.* ***29*** *(1992) 221–228.*

[39] T. Liu, W. Melnitchouk, J. Qiu and N. Sato, *Factorized approach to radiative corrections for inelastic lepton-hadron collisions,* `2008.02895`.

[40] T. Liu, W. Melnitchouk, J. Qiu and N. Sato, *A new approach to semi-inclusive deep-inelastic scattering with QED and QCD factorization, .*

[41] S. Alekhin, S. A. Kulagin and R. Petti, *Modeling lepton-nucleon inelastic scattering from high to low momentum transfer, AIP Conf. Proc.* ***967*** *(2007) 215–224*, [`0710.0124`].

[42] J. D. Bjorken, *Model Independent Remarks on Electron-Quark Parity Violating Neutral-Current Couplings, Phys. Rev. D* ***18*** *(1978) 3239.*

[43] L. Wolfenstein, *Testing the Weinberg-Salam Model in Polarized ed and ep Deep Inelastic Scattering, Nucl. Phys. B* ***146*** *(1978) 477–482.*

[44] S. Mantry, M. J. Ramsey-Musolf and G. F. Sacco, *Examination of higher-order twist contributions in parity-violating deep-inelastic electron-deuteron scattering, Phys. Rev. C* ***82*** *(2010) 065205*, [`1004.3307`].

[45] A. V. Belitsky, A. Manashov and A. Schafer, *Twist-four Corrections to Parity-Violating Electron-Deuteron Scattering, Phys. Rev. D* ***84*** *(2011) 014010*, [`1104.0511`].

[46] C.-Y. Seng and M. J. Ramsey-Musolf, *Parity Violating Deep Inelastic Electron-Deuteron Scattering: Higher Twist and Parton Angular Momentum, Phys. Rev. C* ***88*** *(2013) 015202*, [`1302.5047`].

[47] R. Petti. private communication, 2021.

[48] A. Accardi, L. T. Brady, W. Melnitchouk, J. F. Owens and N. Sato, *Constraints on large-x parton distributions from new weak boson production and deep-inelastic scattering data, Phys. Rev. D* ***93*** *(2016) 114017*, [`1602.03154`].

[49] R. Petti, *Precision Measurements of Fundamental Interactions with (Anti)Neutrinos,* 10, 2019, `1910.05995`.

[50] S. Li and A. Accardi. private communication, 2021.

[51] H1, ZEUS collaboration, H. Abramowicz et al., *Combination of measurements of inclusive deep inelastic $e^{\pm}p$ scattering cross sections and QCD analysis of HERA data, Eur. Phys. J. C* ***75*** *(2015) 580*, [`1506.06042`].

[52] A. Argento et al., *Measurement of the Interference Structure Function Xg(3) (X) in Muon - Nucleon Scattering, Phys. Lett. B* ***140*** *(1984) 142–144.*

[53] J. C. Bernauer, V. D. Burkert, E. Cline, A. Schmidt and Y. Sharabian, *Determination of two-photon exchange via* e^+p/e^-p *Scattering with CLAS12, Eur. Phys. J. A* ***57*** *(2021) 144*, [`2103.03948`].

[54] E. Cline, J. C. Bernauer and A. Schmidt, *Direct TPE Measurement via* e^+p/e^-p *Scattering at low* ε *in Hall A,* `2103.06301`.

[55] J. R. Arrington and M. Yurov, *A measurement of two-photon exchange in Super-Rosenbluth separations with positron beams,* `2103.03752`.

[56] I. A. Qattan et al., *Precision Rosenbluth measurement of the proton elastic form-factors, Phys. Rev. Lett.* ***94*** *(2005) 142301*, [`nucl-ex/0410010`].

[57] M. Anselmino, P. Gambino and J. Kalinowski, *Polarized deep inelastic scattering at high-energies and parity violating structure functions, Z. Phys. C* ***64*** *(1994) 267–274*, [`hep-ph/9401264`].

[58] T. Hobbs and W. Melnitchouk, *Finite-Q**2 corrections to parity-violating DIS, Phys. Rev. D* ***77*** *(2008) 114023*, [`0801.4791`].

[59] L. T. Brady, A. Accardi, T. J. Hobbs and W. Melnitchouk, *Next-to leading order analysis of target mass corrections to structure functions and asymmetries, Phys. Rev. D* ***84*** *(2011) 074008*, [`1108.4734`].

[60] P. Degtiarenko, J. Grames, J. Kowal, J. Musson, S. Philip, M. Tiefenback et al. private communication, 2020.

[61] D. Day et al., *A Conceptual Design Study of a Compact Photon Source (CPS) for Jefferson Lab, Nucl. Instrum. Meth. A* ***957*** *(2020) 163429*, [`1912.07355`].

[62] P. Valente et al., *Linear Accelerator Test Facility at LNF: Conceptual Design Report,* `1603.05651`.

[63] https://www.bergoz.com/en/mx-bpm.

[64] W. Barry, *A General analysis of thin wire pickups for high frequency beam position monitors, Nucl. Instrum. Meth. A* ***301*** *(1991) 407–416.*

[65] J. F. Benesch. private communication, 2021.

[66] “Senis hall probe magnetometers.” https://www.senis.swiss/magnetometer/overview-magnetometer.

[67] P. J. Mohr, D. B. Newell and B. N. Taylor, *CODATA recommended values of the fundamental physical constants: 2014, Rev. Mod. Phys.* ***88*** *(Sep, 2016) 035009.*

[68] J. F. Benesch, *Passive Shimming Assembly for MR Magnet, U. S. Patent 4990877 (Feb, 1991) .*

[69] B. Dorri and J. F. Benesch, *Method of Otimizing Shim Coil Current Selection in Magnetic Rresonance Magnets, U. S. Patent 5005804 (Apr, 1991)* .

[70] B. Dorri, M. Vermilyea and W. Toffolo, *Passive shimming of mr magnets: algorithm, hardware, and results, IEEE Transactions on Applied Superconductivity* ***3*** *(1993) 254–257.*

[71] *Solid pre-conceptual design report,* .

[72] H. Spiesberger, *Radiative Corrections to Deep Inelastic ep Scattering at HERA,* in *XIII International School of Theoretical Physics: The Standard Model and Beyond, 12, 1989.*